https://doi.org/10.15388/vu.thesis.917
https://orcid.org/0009-0007-0569-8945

VILNIUS UNIVERSITY
STATE RESEARCH INSTITUTE CENTER FOR PHYSICAL SCIENCES AND TECHNOLOGY

Ihor Zharchenko

Direct Impact of Hot Carriers in Photovoltaics

DOCTORAL DISSERTATION

Natural Sciences,
Physics (N 002)

VILNIUS 2026

The dissertation was prepared between 2021 and 2025 at the State Research Institute Center for Physical Sciences and Technology.

Academic Supervisor – Prof. Dr. Jonas Gradauskas, **(**State Research Institute Center for Physical Sciences and Technology, Natural Sciences, Physics, N 002)

This doctoral dissertation will be defended in a public/closed meeting of the Dissertation Defence Panel:

Chairman – Prof. Dr. Nerija Žurauskienė (State Research Institute Center for Physical Sciences and Technology, Natural Sciences, Physics, N 002).
Members:
Prof. Dr. Zigmas Balevičius (State Research Institute Center for Physical Sciences and Technology, Natural Sciences, Physics, N 002),
Prof. Dr. Vygintas Jankauskas (Vilnius University, Natural Sciences, Physics, N 002),
Dr. Pāvels Onufrijevs (Riga Technical University, Natural Sciences, Physics, N 002),
Prof. Dr. Vincas Tamošiūnas (Vilnius University, Natural Sciences, Physics, N 002).

The dissertation shall be defended at a public meeting of the Dissertation Defence Panel at 11:00 on 8th of May 2026 in meeting room A101 of the State Research Institute Center for Physical Sciences and Technology.
Address: Saulėtekio ave., 3, A101, Vilnius, Lithuania
Tel. +37052649211; e-mail: office@ftmc.lt

https://doi.org/10.15388/vu.thesis.917
https://orcid.org/0009-0007-0569-8945

VILNIAUS UNIVERSITETAS
VALSTYBINIS MOKSLINIŲ TYRIMŲ INSTITUTAS FIZINIŲ IR TECHNOLOGIJOS MOKSLŲ CENTRAS

Ihor Zharchenko

Tiesioginė karštųjų krūvininkų įtaka fotovoltikai

DAKTARO DISERTACIJA

Gamtos mokslai,
Fizika, (N 002)

VILNIUS 2026

Disertacija rengta 2021–2025 metais Valstybiniame mokslinių tyrimų institute Fizinių ir technologijos mokslų centre.

Mokslinis vadovas – prof. dr. Jonas Gradauskas (Valstybinis mokslinių tyrimų institutas Fizinių ir technologijos mokslų centras, gamtos mokslai, Fizika, N 002).

Gynimo taryba:
Pirmininkas – prof. dr. Nerija Žurauskienė (Valstybinis mokslinių tyrimų institutas Fizinių ir technologijos mokslų centras, gamtos mokslai, fizika, N 002).
Nariai:
prof. dr. Zigmas Balevičius (Valstybinis mokslinių tyrimų institutas Fizinių ir technologijos mokslų centras, gamtos mokslai, fizika, N 002),
prof. dr. Vygintas Jankauskas (Vilniaus universitetas, gamtos mokslai, fizika, N 002),
dr. Pāvels Onufrijevs (Rygos technikos universitetas, Latvija, gamtos mokslai, fizika, N 002),
prof. dr. Vincas Tamošiūnas (Vilniaus universitetas, gamtos mokslai, fizika, N 002).

Disertacija ginama viešame Gynimo tarybos posėdyje 2026 m. gegužės mėn. 8 d., 11 val. Valstybinio mokslinių tyrimų instituto Fizinių ir technologijos mokslų centro A101 posėdžių salėje.
Adresas: Saulėtekio al., 3, A101, Vilnius, Lietuva
Tel. +37052649211; el. paštas: office@ftmc.lt

CONTENTS

INTRODUCTION 9

Objective 10

Tasks of the research 10

Scientific novelty 10

Practical value of the research findings 11

Statements for defence 11

Author contribution 11

LIST OF PUBLICATIONS 13

1. LITERATURE REVIEW 16

1.1. History of Photovoltaics 16

1.1.1. First generation of solar cells 17

1.1.2. Second generation of solar cells 19

1.1.3. Third generation of solar cells 19

1.1.3.1. Dye-sensitized solar cells 20

1.1.3.2. Perovskite solar cells 21

1.1.3.3. Organic photovoltaics 23

1.1.3.4. Quantum dot solar cells 24

1.1.3.5. Tandem solar cells 25

1.1.3.6. Hot carrier solar cells 26

1.2. The Shockley–Queisser limit 27

1.2.1. Solar Cell parameters 28

1.2.2. Typical loss mechanisms in a solar cell 30

1.2.2.1. Spectral losses 32

1.2.2.2. Optical losses 32

1.2.2.3. Recombination losses 33

1.2.2.4. Electrical losses 34

1.2.2.5. Entropic and thermodynamic losses 35

1.3. Potential techniques to overcome the Shockley–Queisser limit 37

1.3.1. Multijunction technology 37
1.3.2. Quantum-structured materials 39
1.3.3. Spectral manipulation techniques 41
1.4. Hot carriers in semiconductors and their role in photovoltaics 45
1.4.1. Concept of hot carriers 45
1.4.2. Mechanisms of hot carrier generation 45
1.4.3. Hot carrier cooling processes 46
1.4.4. Photovoltaics of hot carriers 47
2. METHODOLOGY 59
2.1. Structure simulation and fabrication 59
2.2. Investigated samples 60
2.2.1. Industrial polycrystalline silicon solar cells 60
2.2.2. GaAs p-n junction structure 61
2.2.3. Ratchet-based sensor 62
2.3. Experimental setup 62
2.3.1. Analysis of electrical properties of samples in direct current regime 62
2.3.2. Measurement scheme and equipment 64
2.3.3. Optical schemes of lasers for investigation 65
3. RESULTS AND DISCUSSION 68
3.1. Spectral Analysis of Hot Carriers 68
3.2. Influence of laser intensity on the formation of hot carrier photoresponse 76
3.3. Influence of Temperature on Hot Carrier Photocurrent Formation 82
3.4. Ratchet-based radiation sensor of broad radiation spectrum. 87
CONCLUSIONS 95
SANTRAUKA 97
PUBLIKACIJŲ SARAŠAS 120
REFERENCES 123

LIST OF ABBREVIATIONS

DC – Down-conversion
DS – Down-shifting
DSSC – Dye-Sensitized Solar Cell
EMF – Electromotive Force
ETL – Electron Transport Layer
ETM – Electron Transport Material (Electron Transport Layer)
HC – Hot Carrier
HCSC – Hot Carrier Solar Cell
HTM – Hole Transport Material
IR – Infrared
I-V – Current-Voltage (Characteristics)
LPE – Liquid Phase Epitaxy
MBE – Molecular Beam Epitaxy
MEG – Multiple Exciton Generation
OPV – Organic Photovoltaic
PCE – Power Conversion Efficiency
PSC – Perovskite Solar Cell
PV – Photovoltaic
QD – Quantum Dot
QDSC – Quantum Dot Solar Cell
SC – Solar Cell
SQL – Shockley–Queisser Limit
SRH – Shockley–Read–Hall recombination
TSC – Tandem Solar Cell
UC – Up-conversion

ACKNOWLEDGEMENTS

I would like to express my sincere gratitude to my supervisor, Prof. Dr. Jonas Gradauskas, for his continuous support, valuable guidance, and high scientific standards, which greatly contributed to the development of this work. His insight, experience, and dedication to research have been a constant source of inspiration throughout my studies.

I am deeply grateful to Dr. Oleksandr Masalskyi, Dr. Edmundas Širmulis, and all my colleagues from the Laboratory of Electronic Processes for their constructive discussions, insightful comments, and support during the course of this research.

I would like to acknowledge the State Research Institute Center for Physical Sciences and Technology and Vilnius University for providing excellent research facilities, resources, and a motivating scientific environment that made this work possible, as well as for the opportunity to prepare and defend this dissertation.

Finally, I would like to express my deepest gratitude to my fiancée, my family, and my friends for their constant support, encouragement, and belief in me throughout this journey.

INTRODUCTION

Over the past decades, the study of increasing the efficiency of solar cells (SCs) has remained one of the key directions of modern photovoltaics and energy research. The classical single junction solar cell based on a p-n junction, despite significant progress in fabrication technologies, has still not reached the theoretical Shockley–Queisser of about 33% (Shockley & Queisser, 1961). The main reason of this low value is the fundamental intrinsic losses determined by the interaction of photons with the semiconductor material (Hirst & Ekins-Daukes, 2011). Among them, the most significant are spectral losses, which occur due to the absence of absorption of photons with energy lower than the bandgap width (E_g), and so called thermalization losses, which are related to the dissipation of the excess energy of photons with energy higher than E_g in the form of heat during the rapid relaxation of hot carriers. Together these two mechanisms account for up to 80% of all intrinsic losses in solar cells (Hirst & Ekins-Daukes, 2011). The practical efficiencies of about 26% for Si and 28% for GaAs still remain below the theoretical maximum.

The development of third-generation photovoltaics is aimed at overcoming these limitations through the use of multijunction structures, spectral conversion, quantum wells and quantum dots, as well as the concept of hot carrier solar cells. Such devices, thanks to the selective extraction of carriers before their thermalization, have the potential to reach efficiencies of up to 66% (Ross & Nozik, 1982). However, the practical realization of these structures faces technological challenges associated with the extremely short lifetime of hot carriers, which lies within the picosecond range. At the same time, hot carriers may induce a photovoltage of opposite polarity to the generation-related component, thereby lowering the overall efficiency of a p-n junction-containing solar cell (Masalskyi & Gradauskas, 2022).

In this context, the hot carrier phenomenon appears to play a dual role. On the one hand, it represents an additional mechanism of intrinsic losses in classical solar cells that questions the attainability of the theoretical efficiency limit. On the other hand, it opens up prospects for the creation of new, highly efficient photovoltaic structures and sensor devices in which hot carrier processes can be deliberately and controllably exploited.

Objective

The objective of the research is to investigate the role of hot carriers in single junction solar cells with a particular focus on their direct impact on the photovoltaic response.

The study aims to evaluate the temperature and spectral conditions under which hot carriers become dominant. Special attention is devoted to the purposeful utilization of the hot carrier effect for the development of novel semiconductor structures, in particular ratchet-based electromagnetic radiation sensors, operating on the basis of hot carrier processes.

Tasks of the research

To achieve the objective of the research, the following tasks were formulated:

1. To investigate current-voltage characteristics of GaAs and Si p-n junctions under laser excitation with different wavelengths and intensities and to analyze the interplay between generation and hot carrier photocurrents.
2. To determine the temperature and spectral conditions under which the hot carrier contribution becomes significant or dominant in the total photovoltaic response.
3. To evaluate the effective hot carrier temperature from current-voltage characteristics.
4. To develop, model, and experimentally test a $GaAs/Al_xGa_{1-x}As$ ratchet-based sensor operating on the hot carrier effect for detection of the electromagnetic radiation.

Scientific novelty

For the first time, the direct impact of hot carriers on the photovoltaic response of single junction solar cells, particularly GaAs and Si p-n junctions, has been experimentally demonstrated over a wide range of wavelengths and temperatures. The effective hot carrier temperature has been determined based on the analysis of current-voltage characteristics and their temperature dependence, specifically for industrial silicon solar cells. In addition, a $GaAs/Al_xGa_{1-x}As$ ratchet-based sensor operating on the hot carrier effect has been developed and experimentally tested. The investigations showed viability of the sensor over a broad spectral and temperature range, providing a novel approach to electromagnetic radiation detection.

Practical value of the research findings

1. The obtained results make it possible to refine the mechanisms of photovoltaic response formation in single junction solar cells and can be applied to revise the efficiency limits of the conventional structures.
2. The determination of the effective hot carrier temperature in industrial silicon solar cells enables more accurate prediction of their operational characteristics under different operating conditions, especially in the concentrated light systems.
3. The developed and experimentally tested $GaAs/Al_xGa_{1-x}As$ ratchet-based sensor demonstrates the practical potential of utilizing the hot carrier effect in devices for electromagnetic radiation detection, particularly in the infrared region, without the need for cryogenic cooling.

Statements for defence

1. The hot carrier photocurrent is present in p-n junction-containing solar cells independently of light photon energy; it results both from the intraband and interband light absorption.
2. The hot carrier photocurrent becomes significant at voltage close to the maximum power point of a solar cell, underscoring the fundamentally detrimental impact of hot carrier processes on device operation.
3. The effective hot carrier temperature can be quantitatively determined using the voltage-temperature coefficient method, providing a direct experimental approach for analyzing carrier heating dynamics in photovoltaic devices.
4. A $GaAs/Al_xGa_{1-x}As$ ratchet-based sensor operates in a wide spectral range detecting both sub- and above-bandgap photons, and its successful operation in the IR range does not require cryogenic cooling.

Author contribution

The author independently carried out the main part of the experimental investigations of GaAs and Si p-n junctions under laser excitation at different wavelengths, intensities and temperatures. The author performed the analysis and visualization of the collected data, separation of generation-related and hot carrier photocurrent components, and the evaluation of effective hot carrier temperature in industrial silicon solar cells. The concept and design of the $GaAs/Al_xGa_{1-x}As$ ratchet-based sensor were developed with the direct participation of the author, who also conducted its experimental testing and

interpretation of the results. The author prepared the manuscripts of the related scientific publications and presented the outcomes at international and national conferences.

LIST OF PUBLICATIONS

Basis of the thesis

(A1) **Zharchenko I.**, Gradauskas J., Masalskyi O., Rodin A. “Hot carrier photocurrent induced by 0.92 eV photon energy radiation in a Si solar cell.” Opto-Electronics Review, 2024 32(2), 1-6.
doi: 10.24425/opelre.2024.150181.
(A2) Gradauskas J., Masalskyi O., Ašmontas S., Sužiedėlis A., Rodin A., **Zharchenko I**. “Hot carrier photocurrent as an intrinsic loss in a single junction solar cell.” Ukr. J. Phys. Opt., 2024, 25(1), 01106-01112.
doi: 10.3116/16091833/Ukr.J.Phys.Opt.2024.01106.
(A3) Ašmontas S., Masalskyi O., **Zharchenko I.**, Gradauskas J. “Some Aspects of Hot Carrier Photocurrent across GaAs p-n Junction.” Inorganics, 2024, 12(174), 1–9. doi: 10.3390/inorganics12060174.

Other publications

(A4) Sužiedėlis A., Ašmontas S., Gradauskas J., Čerškus A., Lučun A., Anbinderis M., **Zharchenko I.** “Anisotropy of Voltage Sensitivity of Bow-Tie Microwave Diodes Containing 2DEG Layer .” – Crystals, 2025 15(367), 1-18. doi: 10.3390/cryst15040367
(P1) Gradauskas J., Ašmontas S., Sužiedėlis A., Masalskyi O., **Zharchenko I.** „Reketinis plataus spektro spinduliuotės jutiklis“ („Ratchet-based sensor of broad radiation spectrum“). Lietuvos Respublikos patentas Nr. LT 7030B (2023/02/17).

List of conference presentations

(C1) V. Kyshchun, Ya. Faier, O. Masalskyi, **I. Zharchenko**, J. Gradauskas, A. Šilėnas, A. Čerškus. “Sensor based on hot carrier effect for electromagnetic radiation detection” – OpenReadings 2025 – 68th International Conference for Students of Physics Natural Sciences, May 13 – 16, 2025.
(C2) **I. Zharchenko**, J. Gradauskas, O. Masalskyi, S. Ašmontas, A. Sužiedėlis, A. Šilėnas, A. Čerškus, V. Kyshchun. “Evidence of Hot Carrier Effect in a Silicon Solar Cell” – Fiztech2024 – 14th Conference of Doctoral Students and Young Scientists, October 15 – 17, 2024.
(C3) O. Masalskyi, J. Gradauskas, **I. Zharchenko**, S. Ašmontas, A. Sužiedėlis, A. Šilėnas, A. Čerškus, E. Širmulis, V. Kyshchun.

“Peculiarities of hot carrier transport across GaAs p-n junction” – The APROPOS 19 Scientific Conference, October 1 – 4, 2024.

(C4) **I. Zharchenko**, J. Gradauskas, O. Masalskyi, S. Ašmontas, A. Sužiedėlis, A. Čerškus. “Unveiling Spectral Peculiarities of Hot Carrier Phenomena in GaAs Solar Cells” – «Lashkaryov’s readings- 2024» Young scientists conference on semiconductor physics, April 4, 2024.

(C5) O. Masalskyi, J. Gradauskas, **I. Zharchenko**, S. Ašmontas, A. Sužiedėlis, A. Šilėnas, A. Čerškus, A. Rodin. “Exploring the unavoidable hot carrier effect in GaAs p-n junction” – 45-oji Lietuvos nacionalinė fizikos konferencija, October 25 – 27, 2023.

(C6) **I. Zharchenko**, J. Gradauskas, O. Masalskyi, S. Ašmontas, A. Sužiedėlis, A. Šilėnas, A. Čerškus. “Exploring Spectral and Temperature Aspects of Hot Carrier Phenomena in GaAs Solar Cells” – Fiztech2023 – 13th Conference of Doctoral Students and Young Scientists, October 18 – 19, 2023.

(C7) J. Gradauskas, S. Ašmontas, O. Masalskyi, A. Sužiedėlis, A. Šilėnas, A. Čerškus, A. Rodin and **I. Zharchenko**. “Peculiarities of hot carrier effect in GaAs p-n junction” – EU PVSEC 2023 – The 40th European Photovoltaic Solar Energy Conference & Exhibition, September 18 – 22, 2023.

(C8) **I. Zharchenko**, O. Masalskyi, J. Gradauskas, S. Ašmontas, A. Sužiedėlis, A. Šilėnas, A. Čerškus, A. Rodin. “Investigating Hot Carrier Effects in GaAs P-N Diodes under Pulsed Laser Irradiation” – MATERIALS OF INTERNATIONAL SCIENTIFIC AND TECHNICAL CONFERENCE LASER TECHNOLOGIES. LASERS AND THEIR APPLICATION – LTLA – 2023, June 29 – 30, 2023.

(C9) **I. Zharchenko**, O. Masalskyi, J. Gradauskas, S. Ašmontas, A. Sužiedėlis, A. Šilėnas, A. Čerškus, A. Rodin. “Spectral peculiarities of hot carrier phenomenon in a solar cell” – Open readings 2023: 66th international conference for students of physics and natural sciences, April 18 – 21, 2023.

(C10) J. Gradauskas, S. Ašmontas, **I. Zharchenko**, O. Masalskyi, A. Sužiedėlis, A. Šilėnas, A. Čerškus, A. Rodin and P. Augustinas. “Low and high photon energy induced photoresponse in single junction solar cells” – The APROPOS 18 Scientific Conference, October 5 – 7, 2022.

(C11) J. Gradauskas, S. Ašmontas, O. Masalskyi, A. Sužiedėlis, A. Šilėnas, A. Čerškus, A. Rodin and **I. Zharchenko**. “Pre-thermalizational impact of hot carriers on photovoltage formation in a single junction solar cell” – The 8th World Conference on Photovoltaic Energy Conversion, September 26 – 30, 2022.

(C12) O. Masalskyi, J. Gradauskas, S. Ašmontas, A. Sužiedėlis, A. Šilėnas, A. Čerškus, A. Rodin and **I. Zharchenko**. “Direct hot carrier impact on photovoltage of a solar cell” – The 23rd Sde Boker Symposium on Solar Electricity Production, September 5 – 7, 2022.
(C13) O. Masalskyi, J. Gradauskas, **I. Zharchenko**. “Photovoltage formation across GaAs p-n junction under intense laser light” – DOC 2022 – 18th International Young Scientist Conference Developments in Optics and Communications, April 21 – 22, 2022.
(C14) O. Masalskyi, J. Gradauskas, S. Ašmontas, A. Sužiedėlis, A. Šilėnas, A. Čerškus, A. Rodin, **I. Zharchenko**. “Hot carriers in photoresponse formation across GaAs p-n junction” – Open Readings 2022 – 65 The international conference for students of physics and natural sciences, March 15 – 18, 2022.

1. LITERATURE REVIEW

1.1. History of Photovoltaics

The high growth of worldwide energy use, together with ongoing environmental problems like climate change, has highlighted renewable energies as critical to sustainable development. The increasing requirement for replacement of fossil fuel-based energy systems with sustainable and clean energy sources has caused particular interest towards solar photovoltaics. Generation of electricity by solar cells represents one of the most promising solutions identified for sustainably meeting the future energy requirements of humanity. It transforms sunlight into electricity via the photovoltaic effect, thus reducing gas emissions and utilizing the solar energy. Significant reductions in photovoltaic module prices over the last twenty years have triggered a rapid development of photovoltaic technology (Green, 2000; Razykov et al., 2011; Green, 2019).

However, research on the conversion of solar energy to electrical energy started as early as the 1800s. The French physicist Edmund Becquerel is frequently acknowledged for initiating the evolution in solar energy utilization through an article in 1839, in which he described an experiment with a wet cell battery (Becquerel, 1839). In his study, Becquerel observed that exposing silver plates to sunlight increased the output voltage of the battery. This finding opened new opportunities for further research (Goetzberger et al., 1998; Green, 1995). Nevertheless, it was not a priority at that time, as fossil fuels were cheap and easily available. Further initiatives to support this initial research were made in the 19th century. Adams and Day investigated the impact of sunlight on selenium in their paper (Adams & Day, 1877). In 1883, Charles Edgar Fritts, an electrician from New York, developed a prototype solar cell with an efficiency ranging from 1–2%, which had similarities to the typical solar cells used at the beginning of the 21st century (McCrea, 2008). The efficiency of this and all other cells was calculated by measuring the electricity produced from the total of possible energy that hits the photovoltaic (PV) surface. This prototype featured many attributes similar to the earliest manufactured solar cells: it included a glass covering, beneath which was a mass of fine gold wires sandwiched between glass and a thin layer of selenium. The early model offered scientists a foundation for future modifications, however it required years of research to boost efficiency and fully understand the reasons for the previously poor production.

The next significant development in the study of the photovoltaic effect originated from Planck's light quantum hypothesis (Planck, 1901), which

formed the foundation for Albert Einstein's 1905 research on the photoelectric effect (Einstein, 1905) – a work that finally won him the Nobel Prize in 1921.

During the second part of the 20th century, development of photovoltaics accelerated, propelled not only by advancements in natural sciences but also by certain historical occurrences that helped the growth of photovoltaic cells. In 1954, researchers at Bell Labs in the United States, made one of the most significant discoveries that influenced the modern solar industry. They have not known it was their study on semiconductors that ultimately advanced solar cell technology (Tsokos, 2008; Perlin, 2004). Semiconductors exhibiting properties between those of metals and insulators were developed using doped silicon, which researchers at Bell Labs found to outperform previously tested selenium. (Chapin et al., 1954). It was the first realization that solar cells could potentially surpass 20% efficiency, compared to the current 1–2% range. However, the researchers recognized that changing to a different material just was not enough for this big advancement, and they continued investigations to find an optimal p-n junction. Researchers at Bell Labs observed that by combining arsenic with silicon and applying a thin layer of boron, they achieved a cell efficiency of 6% (Schaeffer, 2008). Despite advancements, the present product remained too expensive for terrestrial uses. Nevertheless, it proved an ideal choice for the space power applications (National Centre for Photovoltaic Research and Education (NCPRE), n.d.). With continuous developments in solar cell technology, the scope of their potential applications is used. In 1960, Hoffman Electronics created a solar cell with 14% efficiency, initiating a transition from using these cells only in space applications to the potential for terrestrial use. The progression of photovoltaic technology is typically classified into three separate generations (Green, 2006).

1.1.1. First generation of solar cells

The first generation of solar cells includes devices fabricated from traditional semiconductor materials, primarily silicon and III–V compounds. They laid the foundation of modern photovoltaics and for decades remained the dominant technology in the industry.

The operation of such cells is based on the classical p-n junction, where photons with energies equal to or greater than the semiconductor bandgap E_g generate electron-hole pairs (Shockley & Queisser, 1961). The built-in electric field in the space-charge region separates the carriers: electrons drift toward the n-region and holes toward the p-region, forming a photocurrent in the external circuit (Green, 2006; Rühle, 2016).

In the 1980s, significant progress was achieved with gallium arsenide single crystal cells, where the direct bandgap enabled strong absorption in the visible spectrum. These devices reached efficiencies of about 22%. Further development of structures with light concentrators allowed record performance: by 2023 devices exceeded 30% efficiency (Fig. 1.1).

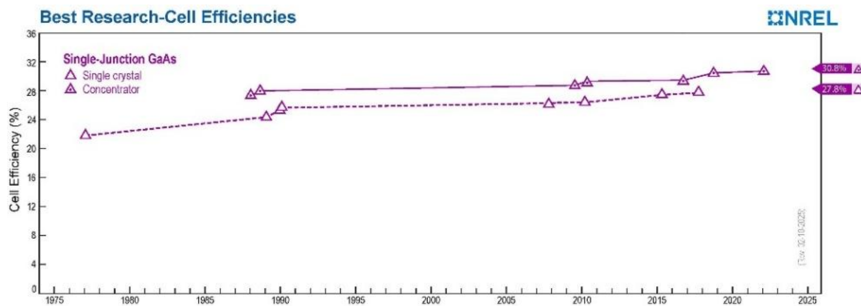

Fig. 1.1. Efficiency development of the $A_{III}B_V$ SC family.

Among silicon-based technologies, monocrystalline structures have played a leading role. Early single crystal Si cells achieved the highest efficiencies in their family, often surpassing later design improvements (Fig. 1.2). In contrast, polycrystalline silicon cells exhibited lower efficiencies due to grain boundaries acting as recombination centers, which reduced the diffusion length of carriers and, consequently, both short-circuit current and open-circuit voltage (Razykov et al., 2011).

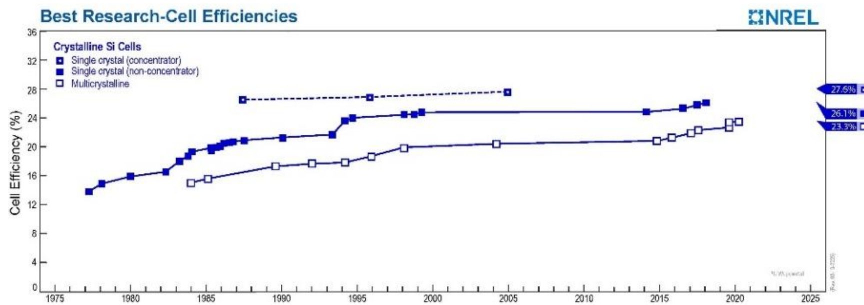

Fig. 1.2. Efficiency development of the silicon SC family.

Overall, first-generation solar cells approached the theoretical Shockley–Queisser efficiency limit for single junction devices (~30%) (Rühle, 2016). However, large-scale deployment was limited by high production costs, the requirement for highly purified materials, and complex technological

processes. Despite these limitations, first-generation solar cells remain the most widely used technology in global energy systems due to their durability and mature fabrication methods (Green, 2000).

1.1.2. Second generation of solar cells

The second generation of solar cells is associated with the development of thin-film technologies, which emerged in the late 1970s as a cheaper alternative to crystalline silicon. These devices require significantly less material, as thin layers can be deposited on different substrates, reducing costs and enabling new applications (Green, 2006).

The main representatives of this generation are cadmium telluride (CdTe), copper indium gallium selenide (CIGS), and amorphous silicon (a-Si). Both CdTe and CIGS have shown remarkable progress over the past decades, reaching laboratory efficiencies above 23%. In contrast, a-Si remained limited to about 14% due to inherent material constraints (Green, 2019; Rühle, 2016). Figure 1.3 illustrates the comparative efficiency evolution of these technologies from the 1980s to 2025.

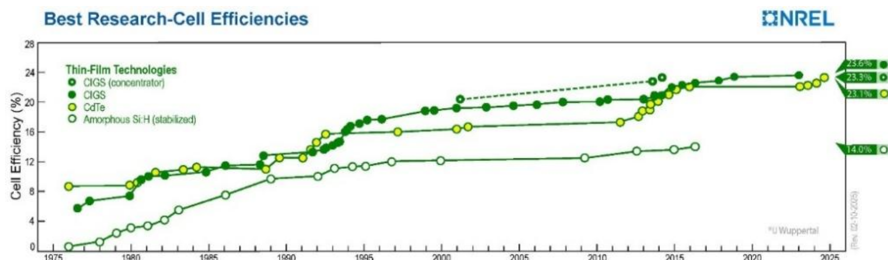

Fig. 1.3. Efficiency development of the thin-film SC technologies.

Although their record efficiencies are still lower compared to crystalline silicon, thin-film solar cells offer clear advantages – they are flexible, lightweight, and cheaper to produce. For these reasons, they are widely used in building-integrated photovoltaics, portable devices, and other fields where versatility is required.

1.1.3. Third generation of solar cells

Like all technologies aiming for excellence, numerous inventions were evaluated, resulting in both successful and unsuccessful outcomes. The photovoltaic sector has seen the rise of promising emerging technologies that

hold the potential to significantly impact the future of power generation. Third-generation PV technologies aim to achieve over 60% efficiency by combining high performance with low production cost while introducing novel concepts such as multijunction architectures, nanotechnology, spectral conversion, photonic and plasmonic light management, and mechanisms like multiple exciton generation, hot carrier extraction, and intermediate band photovoltaics. These technologies are engineered to capture a broader range of the solar spectrum, minimize thermal energy losses, and achieve power conversion efficiencies well beyond the single junction limit. The achieved efficiencies of different photovoltaic technologies are summarized in Fig. 1.4

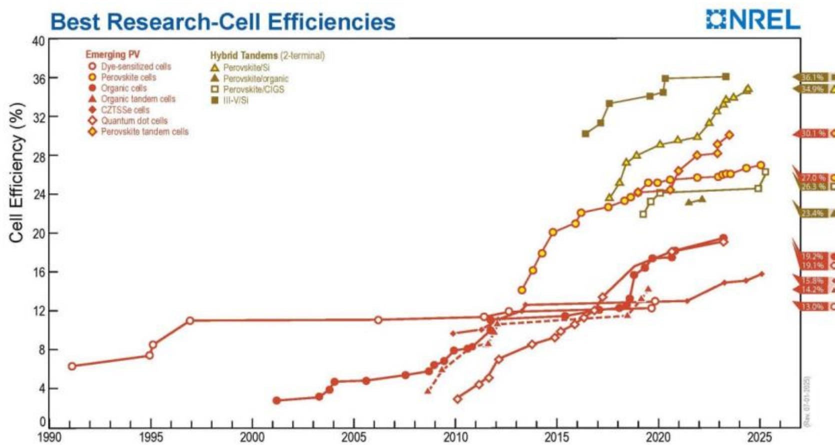

Fig. 1.4. Record efficiencies of emerging photovoltaic technologies.

1.1.3.1. Dye-sensitized solar cells

Dye-sensitized solar cells (DSSCs), also called Grätzel cells, have emerged as a technically and economically feasible alternative to traditional p-n junction photovoltaic systems. DSSCs were among the first emerging photovoltaic technologies, offering a promising path for solar energy conversion due to its potential for economical production and design adaptability (Ren et al, 2023).

DSSC operation is based on the excitation of electrons by photons interacting with sensitizers (see Fig. 1.5). The absorbed energy enables electrons to move from the valence band to the conduction band of the semiconductor material (commonly TiO_2). The electrons then pass through the porous thin semiconductor layer toward the transparent electrode, creating

photocurrent. In this way, DSSCs combine photophysical and electrochemical processes, which together ensure their functionality (Shah et al., 2023).

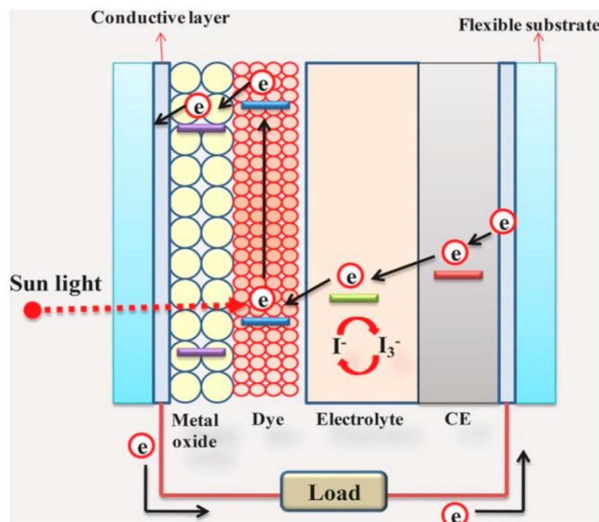

Fig. 1.5. Schematic diagram of a dye-sensitized solar cell. (Shah et al., 2023).

Despite the advantages of easy fabrication and structural flexibility, DSSCs still have lower power conversion efficiency compared to conventional silicon-based solar cells. This is primarily due to inefficient charge separation dynamics and electron recombination at the dye-semiconductor interface, which reduces the number of generated carriers. Nevertheless, intensive research in recent years has significantly improved the performance of DSSCs: advances in dyes, electrolytes, and electrode materials have increased efficiency from 7% to 15%, while the operational lifetime has improved from several months to more than one year (Sharma, 2017).

Thus, DSSCs remain a promising direction in the development of third-generation solar cells, although further work is still required to enhance their stability and efficiency in order to ensure full competitiveness.

1.1.3.2. Perovskite solar cells

Perovskite solar cells (PSCs) generate photoelectric current through a light-absorbing perovskite layer, usually composed of organic–inorganic compounds such as methylammonium lead halide, or fully inorganic substances such as cesium lead halide (Bello et al., 2022). They are recognized

as one of the most promising alternative photovoltaic technologies due to their high power conversion efficiencies, often surpassing those of conventional silicon-based solar cells (Suresh Kumar & Chandra Babu Naidu, 2021).

Typical PSC architectures are divided into conventional (n-i-p) and inverted (p-i-n) structures (Malinkiewicz et al., 2014; Liu et al., 2013). In the former, electrons are transported through the ETM (Electron Transport Material), whereas in the latter holes are extracted through the HTM (Hole Transport Material). A comparison of these two designs is shown in Fig. 1.6.

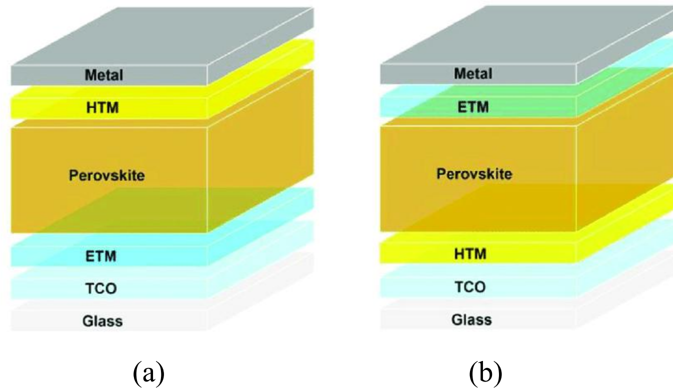

(a) (b)

Fig.1.6. Perovskite solar cell device structure: (a) conventional and (b) inverted (Shah et al., 2023).

The first attempts in this field were made in 2009 by Tsutomu Miyasaka et al., who reported a 3.8% PCE using a DSSC-based design with mesoporous TiO_2; however, these early devices suffered from poor stability due to liquid electrolytes (Lee et al., 2012). Subsequent progress was remarkably rapid, and by 2025 the efficiency of PSCs exceeded 27%. This improvement is attributed to the unique crystal structure of perovskites, which facilitates efficient charge separation and transport.

Nevertheless, there remain critical challenges that limit the commercialization of PSCs: carrier trap formation caused by electron-phonon interactions (Wu et al., 2015), degradation under humidity and light exposure (Brennan et al., 2017), and significant efficiency losses in large-area modules due to scaling issues (Li et al., 2019). Industrial-scale fabrication techniques, including vacuum and chemical vapor deposition, blade coating, slot-die coating, and spray coating, are being developed to address these barriers (Liu et al., 2023). Another key direction is device encapsulation, which is essential to ensure long-term stability under real-world conditions.

1.1.3.3. Organic photovoltaics

Organic photovoltaic (OPV) device is a type of third-generation solar cell in which organic materials such as polymers or small molecules are used to convert sunlight into electrical energy, and a schematic representation is shown in Fig. 1.7. The main advantages of this technology include light weight, flexibility, relatively low production cost, and compatibility with a wide range of substrates. These features open opportunities for integrating OPVs into portable electronics, wearable devices, window systems, and building-integrated photovoltaics (Du et al., 2019; Petrus et al., 2017).

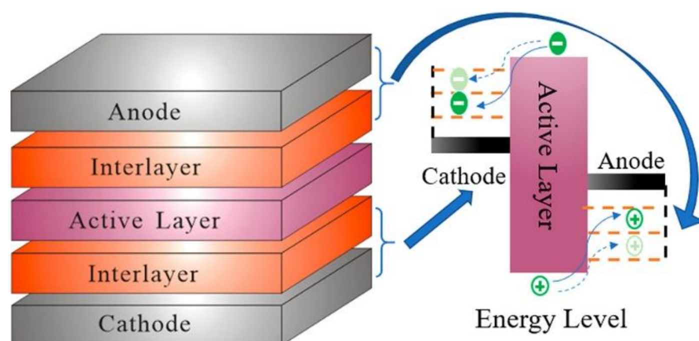

Fig.1.7. A schematic representation of the interfacial bilayer heterojunction configuration employed in organic photovoltaic devices (Li et al., 2020).

Despite their potential, organic solar cells lag behind traditional silicon and perovskite devices in terms of power conversion efficiency. The relatively low PCE is mainly associated with losses during charge separation, recombination at interfacial boundaries, and the limited mobility of charge carriers in organic layers. For this reason, in recent years research interest has gradually shifted away from OPVs toward alternative photovoltaic technologies.

Nevertheless, significant progress has been achieved: the development of new non-fullerene acceptors and optimized polymer blends has enabled OPV efficiencies to reach approximately 19.2%. Furthermore, the operational stability of modern devices has improved considerably, with projected lifetimes of polymer solar cells approaching 10 years (Du et al., 2019).

Thus, organic solar cells remain a promising technology thanks to their flexibility, low production costs, and wide integration possibilities. However, their role in the future development of photovoltaics will likely remain limited to niche applications due to lower efficiencies compared with other technologies.

1.1.3.4. Quantum dot solar cells

Quantum dot solar cells (QDSCs) are a third-generation photovoltaic technology that employs semiconductor nanoparticles, called quantum dots (QDs), as light-absorbing materials. Nanoparticles in the 2–10 nm size range exhibit variable bandgaps depending on their dimensions, enabling tunable absorption across a broad portion of the solar spectrum. This property makes QDs particularly attractive for multi-junction solar cells (Nozik, 2002; Klimov, 2017).

Structurally, QDSCs are similar to dye-sensitized solar cells, but the dye molecules are replaced by QDs (see Fig. 1.8). The working mechanism involves the generation of electron-hole pairs within the QDs upon photon absorption, followed by electron injection into a wide-bandgap metal oxide (e.g., TiO_2, ZnO, SnO_2), while holes are transferred to an electrolyte or a counter electrode (Kamat, 2013).

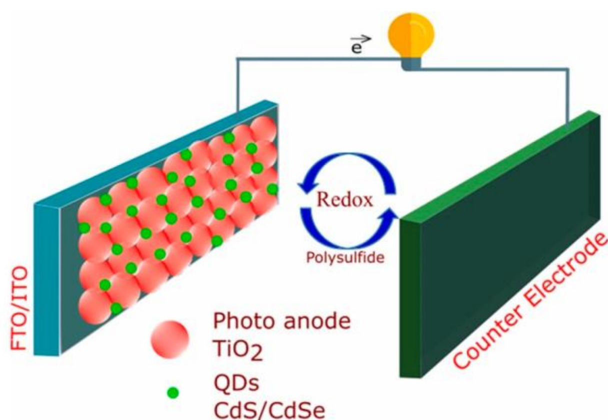

Fig. 1.8. Schematic of a quantum dot solar cell (Shah et al., 2023).

Significant progress has been achieved using various QD sensitizers, including CdSe, PbS, and perovskite QDs, with certain devices reaching efficiencies above 19% (Sargent, 2012; Ning et al., 2015). Furthermore, QDs have been widely studied as functional additives in perovskite solar cells, serving as components in electron and hole transport layers or even replacing them, thereby enhancing charge mobility, reducing recombination, and improving device stability (Brennan et al., 2017; Liu et al., 2021).

Despite these advancements in efficiency and functionality, QDSCs still face substantial challenges related to long-term stability, particularly under

exposure to moisture and oxygen. Addressing intrinsic material degradation, improving encapsulation strategies, and mitigating electrolyte volatility are critical for their commercial viability (Kamat, 2013; Ning et al., 2015).

Thus, with continued progress in material science and device engineering, quantum dot solar cells retain strong potential as a low-cost, high-efficiency solar energy conversion technology. For more detailed discussions, see Section 1.3.2.

1.1.3.5. Tandem solar cells

Tandem solar cells (TSCs) are advanced photovoltaic devices composed of multiple layers of materials with different bandgaps stacked together to more effectively absorb the solar spectrum (see Fig. 1.9). This architecture enables them to reach significantly higher power conversion efficiencies than single junction devices, with a theoretical efficiency limit of about 86% (De Vos, 1980).

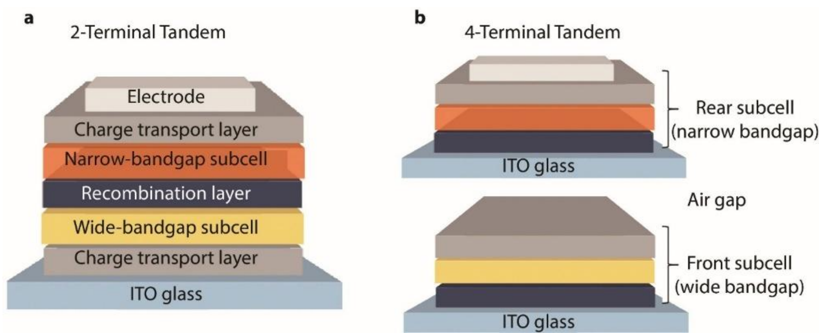

Fig. 1.9. Schematic represntation of two-terminal monolithic (a) and four-terminal (b) tandem structure (Ding et al., 2024).

Various designs have been explored, including two-terminal monolithic and four-terminal mechanically stacked cells. Experimental results demonstrated that combining a semitransparent perovskite solar cell with an efficiency of 18.9% with a silicon cell of 22.9% resulted in a tandem structure with an overall efficiency of about 26.0% (Lamanna et al., 2020; Chen et al., 2020). Further improvements, employing triple-halide perovskites and advanced interlayers, enabled stable efficiencies of around 27% (Xu et al., 2020).

More recent advances have pushed the efficiency even higher: in 2023, stable PSC/Si tandems with efficiencies exceeding 32.5% were reported and

confirmed in updated NREL tables (Shah et al., 2023). Current research continues to focus on improving band alignment, minimizing optical losses, and enhancing stability, with the aim of moving tandem solar cells closer to commercial deployment. For more detailed discussions, see Section 1.3.1.

1.1.3.6. Hot carrier solar cells

Hot carrier solar cells (HCSCs) represent an advanced photovoltaic concept aimed at surpassing the Shockley–Queisser limit by harvesting excess photon energy before it is lost through thermalization. An overview of the hot carrier solar cell concept is provided in Fig. 1.10. Unlike conventional solar cells, where photogenerated carriers quickly cool to the band edges, HCSCs are designed to extract hot carriers while they still retain high kinetic energy. This approach has the potential to significantly boost the power conversion efficiency (Ross & Nozik, 1982).

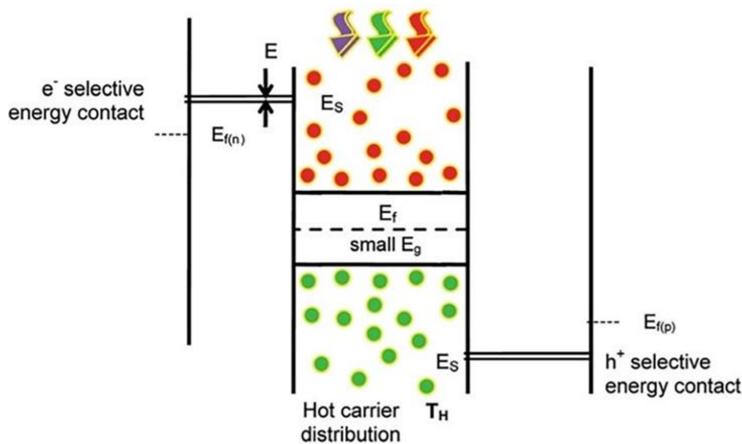

Fig 1.10. Schematic representation of the energy band diagram of a hot carrier solar cell. E_g denotes the band gap, E_f the equilibrium Fermi level, $E_{f(n)}$ and $E_{f(p)}$ the electron and hole quasi-Fermi levels, respectively, E_S the transmission window of the energy-selective contact, and T_H the temperature of the hot carriers (Conibeer, 2007).

Theoretical models predict that HCSCs could achieve a maximum efficiency of up to 66% under standard 1 sun illumination and approximately 85% under concentrated sunlight (Conibeer, 2007; Green, 2019). In contrast to tandem solar cells, hot carrier structures exhibit greater resilience to

spectrum variability, making them potentially more robust under real-world solar conditions (Green, 2019).

At the same time, the practical realization of HCSCs faces two primary challenges:

1. The development of absorber materials capable of slowing carrier cooling while maintaining excellent optoelectronic properties. Research is focused on nanostructures with enhanced quantum confinement effects and materials with suppressed carrier-phonon scattering (Conibeer et al., 2014).
2. The creation of energy-selective contacts able to extract high-energy carriers without inducing thermal relaxation. Such contacts are required to act as narrow energy filters, allowing only carriers with specific energies to pass through.

To address these challenges, new materials and nanostructures are being actively investigated. In particular, quantum dots and nanocrystals have shown promise in sustaining slow carrier cooling due to their discrete energy levels and modified carrier-phonon interaction dynamics (Nozik, 2002).

Thus, hot carrier solar cells are regarded as one of the most promising future technologies capable of overcoming the Shockley–Queisser limit. However, their practical realization depends on the successful development of absorber materials with prolonged carrier cooling and advanced selective contacts.

1.2. The Shockley–Queisser limit

The evolution of photovoltaic technology has advanced through three generations, all eventually focused on overcoming the Shockley–Queisser efficiency limit.

The fundamental limit that defines the maximum theoretical efficiency of photovoltaic conversion of solar radiation for single junction solar cells is the Shockley–Queisser limit (SQL). Using detailed balance principles, William Shockley and Hans-Joachim Queisser first introduced in 1961 a calculation for the maximum achievable efficiency of a solar cell based on a p-n junction. In their model, the solar spectrum represented as the emission of a black body with a surface temperature of T_s = 6000 K (Shockley & Queisser, 1961). They considered an ideal solar cell in which radiative recombination is the only essential recombination mechanism, thereby establishing the fundamental upper limit for minority carrier lifetime (Queisser, 2009). According to their assumptions, photons with energy below the semiconductor's bandgap are not absorbed by the solar cell, whereas photons with energy above the bandgap

generate electron-hole pairs with a quantum efficiency of 100%. Shockley and Queisser determined this theoretical efficiency limit specifically for a single junction solar cell operating at a temperature of 300 K (see Fig. 1.11).

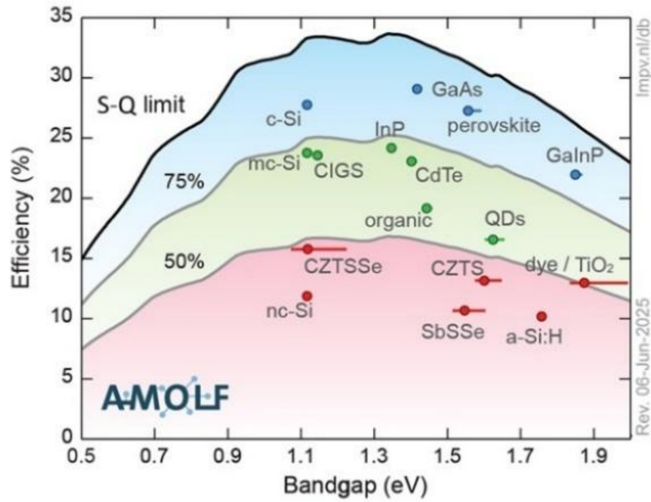

Fig. 1.11. Record solar cell efficiencies shown as a percentage of the Shockley–Queisser limit (black curve), with the gray curves marking 75% and 50% of that theoretical maximum. (AMOLF, n.d.).

Thus, the Shockley–Queisser limit determines the fundamental maximum efficiency boundaries of solar cells based on idealized conditions. To completely understand the practical performance possibilities of photovoltaic devices, it is necessary to examine specific parameters affecting their efficiency. These parameters include the bandgap energy, open-circuit voltage, short-circuit current, and fill factor. A detailed analysis of these parameters provides a better understanding of the origins of efficiency losses and possible strategies to minimize them.

1.2.1. Solar Cell parameters

The Shockley–Queisser limit defines that the maximum efficiency of solar cells is governed by several intrinsic parameters that determine their theoretical performance under ideal conditions (see Fig. 1.12).

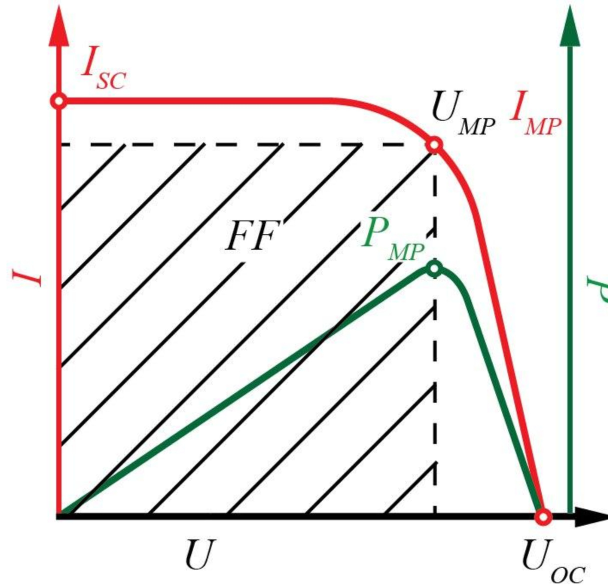

Fig. 1.12. Standard current-voltage curve (red) and power-voltage curve (green) of a solar cell. I_{sc} refers to the short-circuit current, and V_{oc} to the open-circuit voltage, while V_{MP} and I_{MP} denote the voltage and current at the maximum power point, respectively. P_{MP} represents the maximum generated power.

1. Bandgap energy (E_g).
   The bandgap energy of a semiconductor determines the spectrum range for photon absorption in a solar cell. Based on the Shockley–Queisser theory, the optimal bandgap for achieving the highest theoretical efficiency in converting sunlight from "one-sun" illumination with the standard AM 1.5G solar spectrum is approximately 1.34 eV (see Fig. 1.11), which corresponds to a wavelength of 928 nm.
2. Open-circuit voltage (V_{oc}).
   V_{oc} is the maximum voltage generated by a solar cell under conditions without any external load. Even under ideal conditions, the open-circuit voltage V_{oc} remains below the bandgap energy. This is because thermodynamic detailed balance dictates that the solar cell must remain in equilibrium with its surroundings, leading inevitably to spontaneous emission of photons from the cell. The related radiative recombination of carriers shows up as a dark current, causing the open-circuit voltage V_{oc} to be much lower than the bandgap voltage $V_g = \frac{E_g}{q}$.

3. Short-circuit current (I_{sc}).
   I_{sc} represents the maximum current obtained when all photons with energy above the semiconductor's bandgap (E_g) are fully absorbed, and all generated charge carriers are fully extracted. The quantum efficiency of electron-hole pair generation is 100% under the Shockley–Queisser limit assumptions.
4. The fill factor (FF) is a parameter that characterizes the quality of a solar cell and is defined as the ratio of the maximum power output to the product of the open-circuit voltage and the short-circuit current. Even under ideal conditions, the fill factor remains below 100%, as the maximum power point (maximum product of current and voltage, $I \times V$) always corresponds to a lower voltage (V_{MP}) and a lower current (I_{MP}) compared to V_{oc} and I_{sc}, respectively.
5. The efficiency of solar cell is described as

$$\eta = \frac{P_{MP}}{P_{in}} = \frac{V_{MP} I_{MP}}{A \times I} = \frac{V_{oc} I_{sc} FF}{A \times I}, \tag{1.1}$$

where, P_{MP} is the maximum power generated from the solar cell, P_{in} is light source power incident on the cell, V_{MP} and I_{MP} are voltage and current at maximum power (see fig. 1.12), A is the surface area of the solar cells, I is light irradiance incident on cell.

The mentioned parameters define the theoretical performance limit of a solar cell within the Shockley–Queisser model. However, under real-world conditions, achieving these ideal values is constrained by various losses that occur during light absorption, as well as during the generation, transport, and recombination of charge carriers.

1.2.2. Typical loss mechanisms in a solar cell

Although the Shockley–Queisser model establishes the theoretical efficiency ceiling, practical solar cells are subject to significant energy losses during the conversion of sunlight into electricity. These losses fall into two groups: intrinsic losses, determined by the fundamental physical constraints of a single junction device (illustrated in Fig. 1.13), and extrinsic or technological losses, which arise from imperfections in design, material quality, or optical management (Hirst & Ekins-Daukes, 2011).

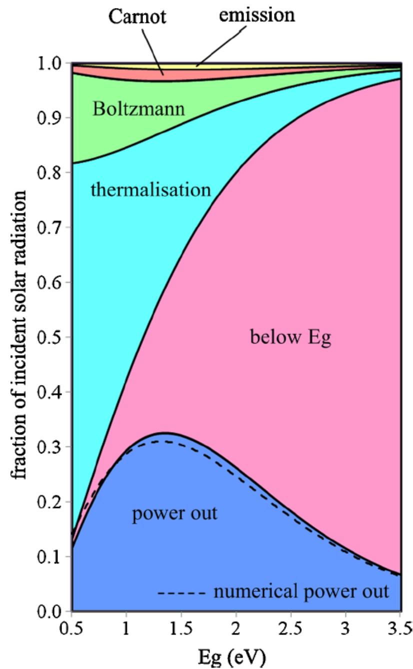

Fig. 1.13. Relationship between the band gap and intrinsic loss mechanisms (Hirst & Ekins-Daukes, 2011).

The main types of losses in photovoltaic devices are typically classified as follows:

a) Spectral losses – caused by the inability to absorb photons with energy below the bandgap, as well as the loss of excess energy during carrier thermalization.
b) Optical losses – due to unabsorbed light as a result of reflection, imperfect anti-reflective coatings, or insufficient thickness of the active layer.
c) Recombination losses – related to the loss of charge carriers through radiative, defect-related (SRH), or Auger recombination before they are collected at the contacts.
d) Electrical losses – include losses due to series and shunt resistance, contact resistance, and voltage drops resulting from uneven current distribution.
e) Entropic and thermodynamic losses – reflect intrinsic constraints related to emission, the increase in the emission solid angle (Boltzmann losses), and the inability to fully concentrate solar radiation.

1.2.2.1. Spectral losses

Spectral losses represent the majority of energy losses in photovoltaic devices, resulting from a difference between the solar radiation spectrum and the semiconductor's ability to efficiently absorb photons within a particular energy range. These losses are generally divided into two main mechanisms:

1. Below Bandgap Losses.
   Photons with energy below the semiconductor bandgap ($E < E_g$) are treated as unabsorbed and do not contribute to the generation of electron-hole pairs. These photons are considered a lost portion of the solar spectrum. The magnitude of such losses depends on the choice of material and its corresponding E_g, which determines the absorption threshold (Shockley & Queisser, 1961; Henry, 1980).
2. Thermalisation Losses.
   Photons with energy higher than E_g are absorbed, but the excess energy (i.e., $h\nu - E_g$) cannot be effectively utilized. After excitation, carriers quickly lose this extra energy as heat by interactions with phonons. Therefore, only the portion of the photon's energy that is equal to E_g is converted into electrical work, and the rest is lost as heat (Würfel, 2016; Hirst & Ekins-Daukes, 2011).

In combination, these two mechanisms can explain up to 80% of the overall energy losses in single junction solar cells during the conversion of sunlight into electricity (Hirst & Ekins-Daukes, 2011). Thus, choosing an optimal bandgap value (approximately 1.1–1.4 eV for the AM 1.5G spectrum) is necessary for achieving high efficiency.

1.2.2.2. Optical losses

Optical losses are formed already at the initial stage of solar energy conversion, when the light flux interacts with the solar cell. Their magnitude is largely determined by the structural features of the device, the quality of the semiconductor material, and the surface architecture. Although many semiconductors are characterized by a high absorption coefficient, a significant part of the photons still does not participate in the generation of electron-hole pairs.

One of the main mechanisms of such losses is reflection. A considerable portion of the incident light is reflected from the surface of the solar cell instead of entering the active layer. For bare silicon, the reflectance can reach up to 30% (Green, 1981), which significantly decreases the number of useful photons. These losses can be reduced by applying antireflection coatings, such

as Si_3N_4 or TiO_2, as well as by introducing surface texturing, which enables multiple passes of photons through the absorber layer (Nelson, 2003). Recent studies highlight that surface engineering and nanostructured coatings offer additional opportunities to significantly suppress reflectance even in high-efficiency silicon and perovskite cells (Kumar & Gupta, 2024; Spaans et al., 2025).

Another mechanism is incomplete absorption in the active layer. This effect is particularly pronounced in thin-film structures, where the absorber thickness is only a few microns, or in materials with a relatively low absorption coefficient, such as GaAs under long-wavelength illumination. In such cases, some photons pass through the layer without interaction and do not generate charge carriers. To reduce incomplete absorption, light-trapping methods, back reflectors, and other technological solutions that extend the optical path length are commonly employed (Polman et al., 2012; Nelson, 2003). Additional modeling using the transfer matrix method demonstrates that for perovskite/Si tandem structures, optimization of layer thicknesses and refractive indices can substantially reduce optical losses (Rafieipour et al., 2023). Similar approaches are being actively implemented in thin-film CIGS devices, where optical path management is considered decisive for approaching theoretical efficiency limits.

A further contribution comes from parasitic absorption. It occurs in layers that do not directly contribute to current generation, such as transparent electrodes (ITO), buffer layers, or protective coatings. In this case, the absorbed energy is converted into heat, which not only fails to enhance photocurrent but can also negatively affect the long-term stability of the solar cell (Nelson, 2003). Modern studies indicate that careful selection of transparent conductive oxides, reduction of buffer-layer thickness, and optimization of front glass can substantially minimize parasitic absorption in CdTe and heterojunction Si devices (Spaans et al., 2025).

Overall, optical losses in conventional solar cells typically amount to about 5–10% of the incident energy flux. Their minimization is especially crucial for thin-film and multijunction structures, where the effective utilization of each photon directly determines the final device efficiency.

1.2.2.3. Recombination losses

Recombination losses represent an important mechanism that restricts the efficiency of solar cells. They occur when electron-hole pairs are lost before they can be collected at the contacts and are directly associated with recombination processes taking place within the bulk of the semiconductor.

Shockley–Read–Hall (SRH) recombination arises due to the presence of trap states within the bandgap. These traps are formed as a result of structural defects, impurities, or chemical contamination. When an electron is captured by a trap, it can recombine with a hole without the emission of a photon. Such processes are particularly pronounced in low-quality materials or structures with a large surface-to-volume ratio. The SRH recombination rate is determined by the trap density, their energy levels, and the carrier lifetime (Shockley & Read, 1952).

Another important mechanism is Auger recombination. It occurs under conditions of high carrier concentration, when the energy released during electron-hole recombination is transferred to a third particle – another electron or hole. The excited carrier rapidly loses this energy through phonon interactions with the lattice. Auger recombination becomes especially relevant under intense sunlight or in high-efficiency devices with elevated carrier injection levels. As a non-radiative process, it significantly reduces device performance at high current densities (Green, 1995; Richter et al., 2012).

A distinct mechanism is radiative recombination, in which an electron in the conduction band recombines with a hole in the valence band accompanied by the emission of a photon. This process dominates in direct bandgap semiconductors, such as GaAs and InP, and is less probable in indirect bandgap materials, such as silicon. Radiative recombination is a fundamental mechanism that defines the Shockley–Queisser limit and sets the theoretical maximum efficiency of a solar cell in the absence of other loss channels (Shockley & Queisser, 1961; Würfel, 2016).

In summary, recombination losses impose a substantial limitation on the achievable open-circuit voltage and remain one of the principal challenges in the development of high-efficiency photovoltaic devices. Minimizing these losses is of critical importance, as effective control over recombination processes is essential for approaching the theoretical efficiency limits.

1.2.2.4. Electrical losses

Electrical losses constitute a specific mechanism that reduces the efficiency of solar cells, as they are directly related to resistances and irregularities in current distribution within the device. As a result, both the voltage and the fill factor are reduced, ultimately limiting the overall output power.

A significant role is played by series resistance, which includes the cumulative resistance of all layers through which current flows. This encompasses the semiconductor region, transparent conductive oxides,

metallic grid fingers, and interconnects. When the series resistance is too high, voltage drops occur within the device, particularly under high current conditions, which directly lowers the fill factor and overall power output. Reduction of these losses can be achieved by optimizing layer thickness and conductivity, shortening current pathways, and employing low-resistivity silver contacts (Green, 1981).

Equally important is the shunt resistance, which arises from alternative current pathways bypassing the p-n junction. Such leakage channels may result from microcracks, fabrication defects, or contamination. Low shunt resistance is particularly detrimental under low illumination, when the photocurrent is small and even minor leakage currents can cause significant reductions in voltage and efficiency. Conversely, high shunt resistance is desirable and can be ensured through strict process control and isolation of defective regions (Green, 1981).

Another factor is the contact resistance, which characterizes the resistance at the interface between the semiconductor and the electrodes or transparent conductive layers. Elevated values of this parameter lower the voltage at the external terminals and hinder efficient carrier collection. Minimizing contact resistance is important for high-efficiency devices and can be achieved through surface chemical treatments, the use of intermediate contact layers, or high-temperature annealing (Aberle, 2001).

Therefore, electrical losses hinder the attainment of optimal solar cell performance. Optimization of materials, contacts, and fabrication technologies is required for improving efficiency and approaching the theoretical limits.

1.2.2.5. Entropic and thermodynamic losses

Entropic and thermodynamic losses are fundamental limitations of energy conversion in a solar cell. They occur even in the absence of material defects and are determined by the general laws of thermodynamics and statistical physics, forming an intrinsic part of the voltage generation process.

One unavoidable mechanism is emission loss. According to Kirchhoff's law, any material capable of absorbing radiation must also emit it. In solar cells, particularly near open-circuit voltage, spontaneous radiative emission of photons takes place. This process reduces V_{oc} and manifests as dark current. Even in theoretically ideal structures, emission losses cannot be eliminated, which is why they are included in the Shockley-Queisser limit. Their magnitude depends on the device geometry, the reflection of emitted radiation,

and the efficiency of recombination processes (Shockley & Queisser, 1961; Würfel, 2016).

Another fundamental limitation is represented by Carnot losses. A photovoltaic converter operates between two thermal reservoirs – a hot one (the Sun, about 6000 K) and a cold one (the solar cell, about 300 K). This configuration is analogous to a heat engine, and thermodynamic principles impose an upper limit on the maximum voltage a solar cell can generate. The concept of Carnot loss thus demonstrates that the temperature difference between the reservoirs defines the theoretically achievable maximum efficiency of solar energy conversion (Hirst & Ekins-Daukes, 2011).

A further category is Boltzmann losses, which arise from the mismatch between the solid angles of absorption and emission. Sunlight enters the cell within a limited solid angle, whereas emitted photons are radiated in all directions. This leads to an entropic increase in photon flux and a reduction of the maximum voltage available for conversion. Within the Landsberg formalism, such losses are described as a reduction in the free energy of photons due to the expansion of photonic modes (Landsberg & Tonge, 1980; Hirst & Ekins-Daukes, 2011; Würfel, 2016). Figure 1.14 illustrates this process: in a conventional solar cell, the emission solid angle greatly exceeds the absorption angle ($\Omega_{emit} >> \Omega_{abs}$), while in systems with maximum light concentration or restricted emission, their matching minimizes free-energy losses and enables higher V_{oc} (Ekins-Daukes et al., 2013).

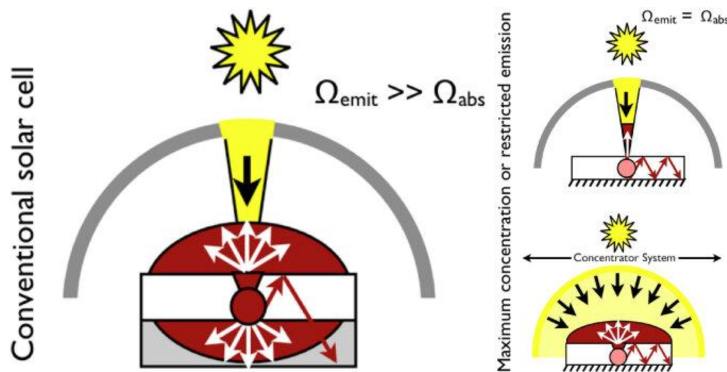

Fig. 1.14. Schematic illustration of Boltzmann losses in a conventional solar cell and in systems with light concentration or restricted emission (Ekins-Daukes et al., 2013).

1.3. Potential techniques to overcome the Shockley–Queisser limit

The previously discussed loss mechanisms define the efficiency limits of classical single junction solar cells and explain why, in practical conditions, their performance is lower than the theoretical maximum. Improved fabrication technologies, material engineering, and device architecture can minimize some of these losses, such as recombination or optical losses. Others, such as thermodynamic losses, are intrinsic and cannot be removed under the traditional approach.

However, modern photovoltaics is moving beyond the classical paradigm. The implementation of innovative concepts provides a means of overcoming the fundamental limitations formulated in the Shockley–Queisser model.

1.3.1. Multijunction technology

Multijunction solar cells (MJSCs) were developed to minimize the spectrum losses related to single junction devices. Rather than depending on a single material to absorb every wavelength of the solar spectrum, MJSCs combine many semiconductor layers in a cascade structure, each with a different bandgap, optimized to convert a specific part of the solar spectrum. This configuration enables significantly higher theoretical efficiencies, exceeding 45% under concentrated light, by absorbing and utilizing a broader range of the solar spectrum more effectively (Baiju & Yarema, 2022; Henry, 1980; Martí & Araujo, 1996). In the standard MJSC architecture, the top cell with the highest bandgap absorbs high energy (short wavelength) photons, while lower energy photons penetrate and are absorbed by succeeding subcells that have smaller bandgaps. This configuration minimizes thermalization losses, where extra photon energy is lost as heat, and below-bandgap losses, where low energy photons are unabsorbed (Baiju & Yarema, 2022; Polman et al., 2016).

Each subcell operates as a separate p-n junction, with its population of photogenerated carriers. In monolithic multijunction configurations, these subcells are stacked and interconnected by tunnel junctions or recombination contacts that facilitate carrier transport with minimal voltage drop. This configuration necessitates strict current matching, as all subcells are connected in series and the overall current is limited by the lowest-performing junction (Kurtz et al., 2008). Incorrect current matching can result in power loss and increased recombination. Alternatively, spectrum-splitting systems use optical filters or dichroic mirrors to spatially separate incoming photons based on wavelength, directing them to appropriately matched single junction

cells (see Fig. 1.15). This decouples the subcells electrically, eliminating the need for current matching and enabling independent optimization of each absorber (Nell & Barnett, 1987).

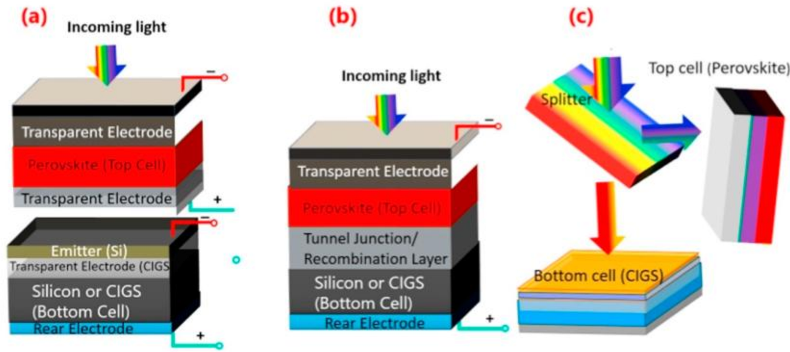

Fig. 1.15. Schematic diagram of tandem solar cell, (a) mechanically stacked four terminal (4T), (b) monolithically integrated 2T, and (c) optical splitting of the solar spectrum (Shah et al., 2023).

The basic material systems and structural designs employed in MJSCs determine the effect of different absorber combinations and architectural approaches on achieving high efficiency solar energy conversion.

GaInP/GaAs/Ge epitaxial multijunction structures are widely used in space and concentrator photovoltaics because of their higher radiation resistance, flexible bandgap configurations, and excellent crystal stability (Henry, 1980; Martí & Araujo, 1996). The top layer of GaInP and middle GaAs subcells have direct bandgaps, enabling in effect radiative recombination and strong photon absorption, important for achieving high open-circuit voltages (Baiju & Yarema, 2022). Although Ge, used as the bottom subcell, has an indirect bandgap, it effectively absorbs long-wavelength photons and contributes to current generation. Geisz et al. (2020) presented a six-junction III-V device achieving over 47% efficiency under concentrated illumination (Geisz et al., 2020).

Perovskite/Si tandems represent a highly promising strategy for achieving increased efficiency at reduced costs in multi-junction solar cell technology (Henry, 1980; Martí & Araujo, 1996). Perovskites offer solution-processable fabrication, tunable bandgaps achieved either by modifying halide composition or by controlling the number of atomic layers (a process known as dimensional engineering), and compatibility with existing crystalline silicon technologies (Baiju & Yarema, 2022). Their strong absorption

coefficients and long carrier diffusion lengths allow for thin, high-performing layers atop silicon subcells. Monolithic two-terminal designs have achieved above 33% efficiency in laboratory conditions, whereas three-terminal or mechanically stacked solutions are still under investigation to alleviate current-matching limitations (Al-Ashouri et al., 2020; Bush et al., 2017).

Hybrid configurations, including combinations of CIGS, organic semiconductors, or quantum dots with silicon or perovskite subcells, provide a versatile platform for designing flexible, lightweight, and solution-processable tandem structures. These hybrid architectures can exploit the complementary absorption ranges of different materials while also reducing production complexity and cost. The tunability of organic and quantum dot bandgaps makes them advantageous for integration in spectrum-matched tandem devices with relaxed lattice-matching requirements (Baiju & Yarema, 2022).

Despite the significant potential of multijunction solar cells, some critical technological challenges must be overcome to fully realize their potential. These include bandgap selection and lattice matching between layers, optical losses and imperfect antireflection coatings, series resistance in tunnel junctions that reduces the fill factor, and the high cost and complexity of III-V material growth (Yamaguchi et al., 2008).

1.3.2. Quantum-structured materials

Quantum-structured materials use the quantum confinement effect, which arises when the size of semiconductor structures is reduced to the nanometer scale. This allows for precise control over the bandgap energy, absorption spectrum, and recombination mechanisms, paving the way to overcome the classical limitations of single junction solar cells.

Quantum dots are zero-dimensional (0D) semiconductor nanocrystals that confine charge carriers in all three spatial dimensions. This complete quantum confinement leads to an increase in the bandgap energy as the dot size decreases. Such a property allows precise tuning of the spectral sensitivity by varying the size of the nanocrystals (Nozik, 2002). Materials such as PbS, PbSe, CdSe, InP, as well as perovskite-based quantum dots (e.g., $CsPbX_3$), are widely used in QD-based solar cells, down-shifting coatings, and multiple exciton generation (MEG) concepts (Semonin et al., 2011). Strong spatial confinement also reduces carrier scattering but increases sensitivity to surface defects. Therefore, surface passivation (e.g., organic ligands or dielectric shells) is essential to suppress non-radiative recombination and prolong carrier lifetimes (Kamat, 2013).

Quantum wells are two-dimensional (2D) nanostructures in which carriers are confined to one dimension (usually with a thickness of less than 10 nm) while remaining free to move in the other two. QWs are created by sandwiching a low-bandgap semiconductor layer (e.g., GaAs) between two higher-bandgap layers (e.g., AlGaAs). Figure 1.16 shows schematic energy band diagrams for QWs under the influence of the electric field in a solar cell. The top diagram illustrates the thermal escape of carriers across potential barriers, whereas the bottom diagram demonstrates carrier tunneling through the barriers.

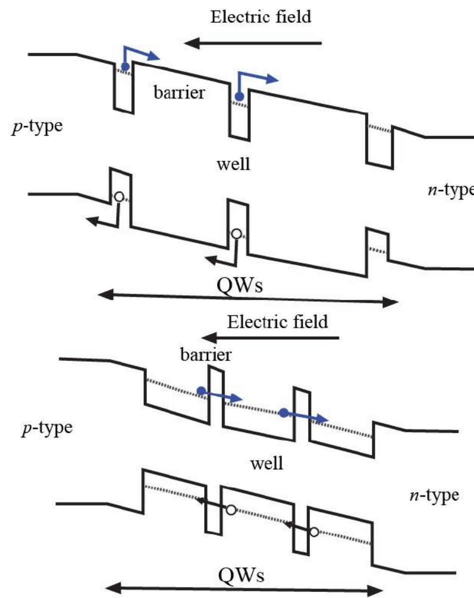

Fig. 1.16. Energy band diagrams of quantum wells in a solar cell: top – thermal escape of carriers; bottom – tunneling of carriers.

The resulting quantum confinement leads to discrete energy levels, enabling tailored absorption properties and improved light absorption at particular photon energies (Nelson, 2003). In photovoltaics, QWs are used to increase optical absorption, enable intermediate-band-like behavior, and reduce recombination losses. Additionally, they support advanced effects, including resonant tunneling, quantum cascade transitions, and carrier collection optimization in tandem structures (Würfel, 2016).

Quantum wires are one-dimensional (1D) nanostructures in which carriers are confined in two dimensions, allowing free transport only along the wire axis. This anisotropic geometry enhances carrier collection, enables natural

surface texturing for reduced reflection, and supports integration into flexible or transparent solar cell designs (Garnett & Yang, 2010). Quantum wires can demonstrate transverse mode quantization, surface plasmon resonance effects, and effective mass reduction of carriers due to spatial confinement. They also improve light-trapping through enhanced scattering and guiding effects in nanowire arrays (Hu & Chen, 2007).

Despite their considerable potential for improving efficiency, quantum-structured materials have several limitations that hinder their practical application. Quantum dots, while enabling precise bandgap tuning and multiple exciton generation, are sensitive to surface traps that cause non-radiative recombination and shorten carrier lifetimes. Additionally, they often contain toxic elements (Pb, Cd) and demonstrate low stability (Nozik, 2002; Semonin et al., 2011; Kamat, 2013). Quantum wells improve spectrum absorption, but carrier confinement in thin layers increases recombination probability and complicates electrical extraction, while device integration requires precise lattice matching (Nelson, 2003; Würfel, 2016). Quantum wires provide anisotropic transport and improved light harvesting but are prone to surface recombination and require complex growth processes to maintain crystalline quality (Garnett & Yang, 2010; Hu & Chen, 2007).

1.3.3. Spectral manipulation techniques

Spectral manipulation techniques aim to minimize the spectral mismatch between the solar spectrum and the absorption properties of photovoltaic devices. The main aim is to redirect energy that would be lost as unabsorbed sub-bandgap photons or thermalization losses in a standard solar cell into useful energy to generate electron-hole pairs (Trupke et al., 2002; Richards, 2006; Van Sark et al., 2005).

Up-conversion is a nonlinear optical process that transforms two or more low-energy photons, each with energy below E_g, into a single-photon with energy exceeding E_g, thus enabling its absorption by the PV device (see Fig. 1.17). This process has been investigated in rare-earth doped systems, semiconductor nanocrystals, and organic molecular assemblies. Up-conversion operates through sequential photon absorption, excited-state absorption, or cooperative energy transfer, both requiring long-lived intermediate states.

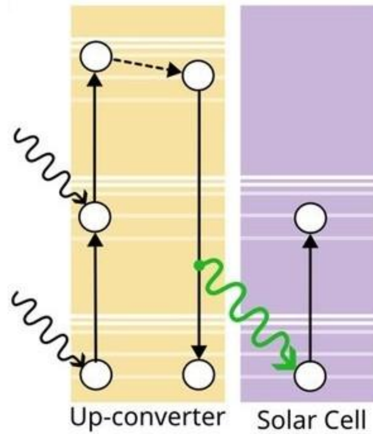

Fig. 1.17. Schematic energy diagrams of the mechanism of up-conversion (Santos et al., 2025).

Excited-state absorption refers to the process whereby an electron (or activator ion) first absorbs a photon, promoting it to an intermediate energy level. A subsequent photon then excites it to a higher level above E_g, from which it can contribute to conduction band population. Energy transfer up-conversion occurs when two nearby excited ions interact through dipole-dipole coupling, transferring energy from one to the other, which is elevated to a higher excited state capable of emitting a photon with energy above the bandgap. The practical implementation of UC is limited by the intrinsically tiny absorption cross-sections of rare-earth ions, the necessity for high excitation density to populate excited states, and the requirement to suppress nonradiative relaxation associated with phonon interactions. Embedding ions into host matrices with low phonon energies, such as fluorides, enhances the probability of radiative transitions and improves UC efficiency (Auzel, 2004; Shalav et al., 2007; Richards, 2006).

Conversely, down-conversion (or spectral down-shifting) entails the splitting of a single high-energy photon into two lower-energy photons, both of which can be absorbed to produce charge carriers, as represented in Fig. 1.18.

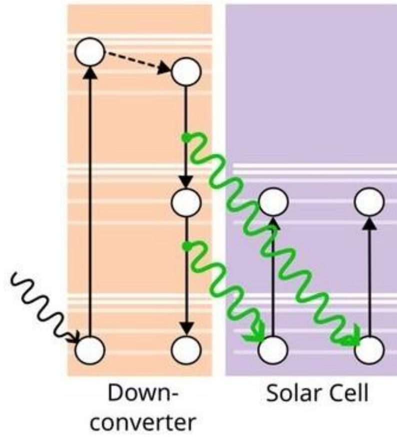

Fig. 1.18. Schematic energy diagrams depicting the down-conversion mechanism (Santos et al., 2025).

This technique reduces thermalization losses by optimizing the redistribution of excess photon energy. Physical implementations often include cooperative energy transfer between rare-earth ions or semiconductor quantum dots, where a single absorbed high-energy photon excites two lower-energy transitions. The objective is to achieve high quantum yields while minimizing nonradiative recombination. Down-shifting, a related mechanism, involves shifting high-energy photons to slightly lower energies (still above E_g) to match the spectral response of the absorber and reduce energy lost as heat (see Fig. 1.19).

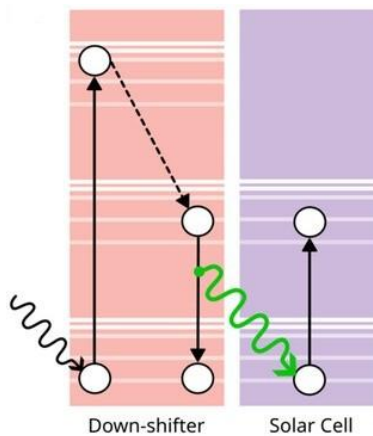

Fig. 1.19. Schematic energy diagrams illustrating the mechanism of down-shifting (Santos et al., 2025).

Although experimentally simpler than UC, DC/DS systems require precise spectral matching and high luminescence quantum yields to achieve measurable efficiency improvements (Richards, 2006; Trupke et al., 2002).

Multiple exciton generation, also known as carrier multiplication, is a process in which a single high-energy photon can generate more than one electron-hole pair. In contrast to photon-based methods (e.g., down-conversion), MEG transpires directly within the semiconductor material and involves the redirection of excess energy from hot carriers, which under standard conditions typically gets lost through rapid phonon relaxation. This technique is closely related to impact ionization, whereby the excess kinetic energy of a hot electron or hole is used to excite an additional electron-hole pair (Nozik, 2002). In bulk semiconductors, this effect is highly improbable due to the dominance of ultrafast energy dissipation through phonon scattering. However, in nanocrystals (quantum dots), quantum confinement significantly enhances Coulomb interactions between carriers, thereby increasing the likelihood of carrier-carrier collisions necessary for MEG (Schaller & Klimov, 2004). Moreover, the discretization of energy levels in quantum dots suppresses certain scattering channels, making the process more efficient compared to bulk crystals (Beard et al., 2014). Experimental investigations have shown that in PbSe, PbS, and CdSe quantum dots, quantum yields can exceed 100%, meaning that a single high-energy photon can initiate two or more electron-hole pairs (Semonin et al., 2011). This establishes a pathway for minimizing thermalization losses and increasing the maximum efficiency of solar cells beyond the Shockley–Queisser limit. Nevertheless, the practical realization of MEG-based solar cells faces several challenges. Chief among these is the ultrafast cooling of hot carriers, characterized by relaxation periods in the range of hundreds of femtoseconds, which competes with the formation of additional excitons (Klimov, 2006). Moreover, the generated multiexciton states are susceptible to Auger recombination, significantly reducing their efficiency. As a result, current research is focused on strategies to slow down hot carrier cooling, engineering interfaces for efficient extraction of multiexcitons into the external circuit, and minimizing Auger recombination (Beard et al., 2014). MEG remains one of the most promising mechanisms for overcoming fundamental loss channels in photovoltaics, but it requires further advances in material design and device engineering to enable practical implementation.

Spectral manipulation techniques aim to enhance the spectral response of solar cells while also reducing fundamental thermalization and sub-bandgap losses, as predicted by the Shockley–Queisser model. These approaches underscore the significance of photon management as a strategy for enhancing

efficiency by redistributing or harnessing photon energy that would otherwise go to waste. However, their practical implementation faces significant limitations such as low quantum yields, fast carrier cooling, and parasitic recombination channels. These limits indicate the importance of complementary concepts that target carrier dynamics directly.

1.4. Hot carriers in semiconductors and their role in photovoltaics

Despite the strong theoretical potential of the approaches discussed above, their practical impact remains limited, highlighting the necessity for alternate strategies. Among such paradigms, the hot carrier processes may serve as a direct strategy to overcome thermalization losses (Ross & Nozik, 1982).

1.4.1. Concept of hot carriers

In equilibrium, charge carriers in semiconductors follow the Fermi–Dirac distribution at the lattice temperature T_0. Absorption of photons with energies exceeding the bandgap or the action of strong electric or microwave fields drives electrons and holes into a nonequilibrium state with excess energy. Such carriers are termed hot carriers, and their distribution is often approximated by an effective temperature $T_e > T_0$ that reflects the average energy of the electron or hole gas. This approximation is valid when carrier-carrier scattering rapidly establishes a quasi-thermal distribution, while in other cases the actual non-thermal distribution function must be considered (Dienys & Požela, 1971; Zhang et al., 2021). The physical nature of the hot carrier effect manifests in two main scenarios. First, during interband photon absorption, the excess energy after electron-hole pair generation is transferred to carriers, leading to their heating and following rapid thermalization into the lattice (Ahmed et al., 2021). Second, sub-bandgap photons ($h\nu < E_g$) or microwave radiation can directly heat free carriers, producing an additional electromotive force (EMF) across inhomogeneous structures.

1.4.2. Mechanisms of hot carrier generation

Several approaches to hot carrier excitation have been described in the literature, each with its own advantages and limitations (Dienys & Požela, 1971; Požela, 1993). One of the earliest methods is microwave irradiation. The frequency range 0.3–300 GHz corresponds to photon energies far below the semiconductor bandgap (Zhou et al., 2019). As early as 1959 it was shown that a combination of a dc electric field and microwave modulation in n-type

Ge leads to measurable changes in conductivity (Morgan, 1959). This method enables contactless carrier heating and reduces the influence of structural inhomogeneities in the sample. At the same time, it has a number of drawbacks: the periodic nature of heating complicates the quantitative interpretation of results, and there is considerable uncertainty in determining the actual amplitude of the electric field inside the specimen (Požela, 1993).

Another widely used approach is excitation by short voltage pulses applied to samples with ohmic contacts. The pulse duration is chosen so that carriers can gain excess energy without causing significant lattice heating. Additional heat dissipation techniques are applied to stabilize the crystal temperature (Dienys & Požela, 1971). An advantage of this method is the possibility to control the energetic state of carriers in the time domain, which is particularly important for studying their relaxation dynamics.

For photovoltaics, the most relevant approach is optical excitation, as it directly reflects the operational conditions of solar cells. When the photon energy $h\nu > E_g$, absorption generates electron-hole pairs, and the excess photon energy is transferred into carrier kinetic energy, leading to heating. In the case of $h\nu < E_g$, direct interband excitation is impossible, yet photons can still interact with electrons already present in the conduction band, promoting them to higher energy states via intraband absorption. Thus, optical irradiation induces two parallel processes: classical interband generation of carriers and direct heating of free carriers (Ahmed et al., 2021).

1.4.3. Hot carrier cooling processes

After excitation, hot carriers lose their excess energy through a multistage cascade of scattering events that typically lasts from several tens of femtoseconds up to a few picoseconds (Conibeer et al., 2014; Zhang et al., 2021). In the initial stage, rapid carrier-carrier scattering, including electron-electron and electron-hole collisions, leads to the formation of a quasi-thermal distribution that can be described by a Fermi–Dirac function at an elevated effective temperature T_e. Subsequent cooling proceeds mainly through the emission of optical phonons, which serve as the dominant energy relaxation channel in most semiconductors. Because the energy of an optical phonon is limited, carriers must emit a large number of phonons to dissipate their excess energy, resulting in the formation of an intense phonon cascade. In the next step, these optical phonons undergo decay into acoustic phonons, which transfer the energy into the crystal lattice. This process leads to local lattice heating and modifies material parameters such as carrier mobility and the bandgap width, the latter often manifested as bandgap narrowing.

Ultimately, nearly all of the excess energy of hot carriers is converted into heat (see Fig. 1.20), which significantly reduces the efficiency of photovoltaic conversion.

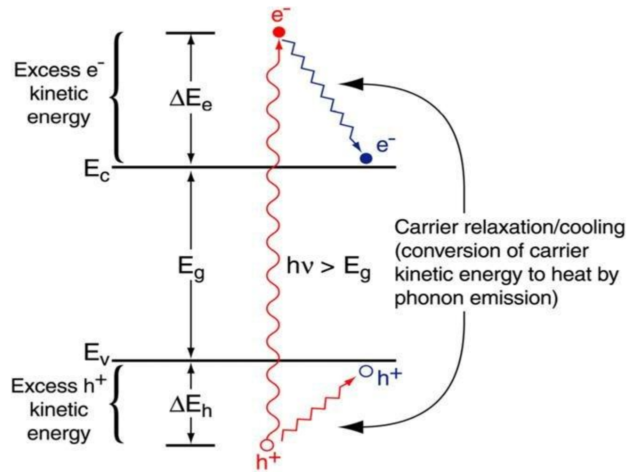

Fig. 1.20. Process of hot carrier cooling in semiconductor materials.

The overall hot carrier lifetime is on the order of 1 ps, and this ultrafast relaxation is regarded as the main obstacle to the practical extraction of hot carrier energy in optoelectronic devices. Therefore, one of the central challenges in modern semiconductor physics and photovoltaics is either to slow down the relaxation process by engineering materials and structures (for example, introducing quantum wells, nanostructures, or phonon bottleneck layers), or to extract hot carriers through energy-selective contacts before cooling occurs. Both approaches are considered essential requirements for the realization of efficient hot carrier solar cells (Ahmed et al., 2021; Zhang et al., 2021).

1.4.4. Photovoltaics of hot carriers

The first experimental evidence of hot carrier photovoltage was obtained in Ge p-n junctions irradiated with a CO_2 laser (λ = 10.6 μm, $h\nu \approx 0.12$ eV < E_g). The observed signal exhibited a polarity opposite to that of the classical generation-induced photovoltage, and this phenomenon was later termed the *hot photo-carrier effect* (Umeno et al., 1978). Subsequent investigations by Lithuanian researchers made a significant contribution to understanding the peculiarities of the hot carrier photoeffect in gallium arsenide structures. It was established that the amplitude and polarity of the induced photovoltage

strongly depend on the junction configuration (p-n, p-p$^+$, or n-n$^+$) as well as on the electrical parameters of the base layer (Ašmontas et al., 1997). In particular, measurements showed that samples with low-resistivity bases (Fig. 1.21 (b)) exhibited a stronger hot carrier signal compared to those with high-resistivity bases (Fig. 1.21 (a)).

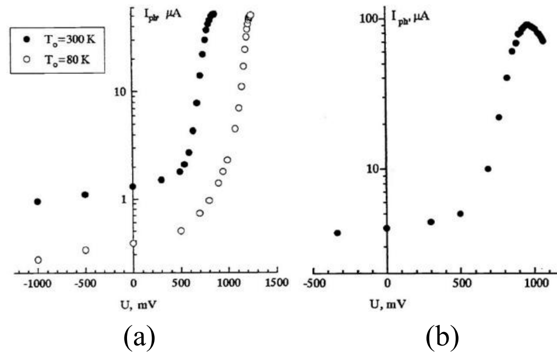

Fig. 1.21. Dependence of photocurrent on bias voltage in n-p$^+$ junctions exposed to CO_2 laser radiation: (a) structure with a high-resistivity base measured at various lattice temperatures, (b) structure with a low-resistivity base measured at room temperature (Ašmontas et al., 1997).

This behavior was explained by the enhanced role of the built-in electric field and the distribution of space charge in shaping the transport and separation of heated carriers. These tendencies are clearly illustrated in Fig. 1.22.

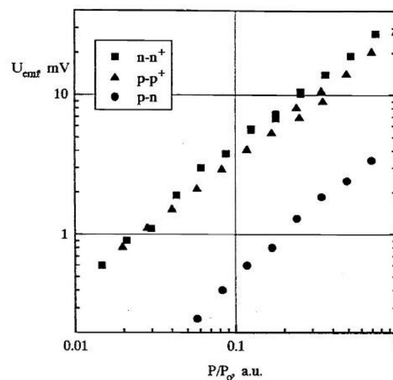

Fig. 1.22. Photoelectromotive force in p-n junctions with a high-resistance base and in l-h junctions as a function of CO_2 laser intensity at room temperature (Ašmontas et al., 1997).

The results reveal that asymmetric n-n$^+$ and p-p$^+$ junctions produce significantly higher photovoltages than p-n junctions under identical excitation conditions. At low excitation levels, the signal across the p-n junction remains weak, while n-n$^+$ and p-p$^+$ structures already exhibit measurable voltages above 1 mV. With increasing laser power, the response of the l-h junctions grows linearly, reaching values an order of magnitude higher than those observed in p-n junctions (Ašmontas et al., 1997). This comparative analysis confirms that the magnitude of the hot carrier signal is governed not only by excitation intensity but also by the junction asymmetry and doping profile, which determine the potential barrier and the strength of the internal electric field. Consequently, highly doped n-n$^+$ and p-p$^+$ junctions are much more effective in separating heated carriers and generating strong photoresponses.

Later works demonstrated that, under CO_2 laser excitation, the GaAs n-n$^+$ junction photoresponse consists of two temporal components (Fig.1.23): a fast signal arising nearly simultaneously with the laser pulse, attributed to carrier heating, and a slower signal associated with thermal processes in the lattice (Ašmontas et al., 1999). Importantly, the hot carrier contribution exhibited a polarity opposite to that of the generation-induced component, confirming its distinct physical origin (Ašmontas et al., 2001).

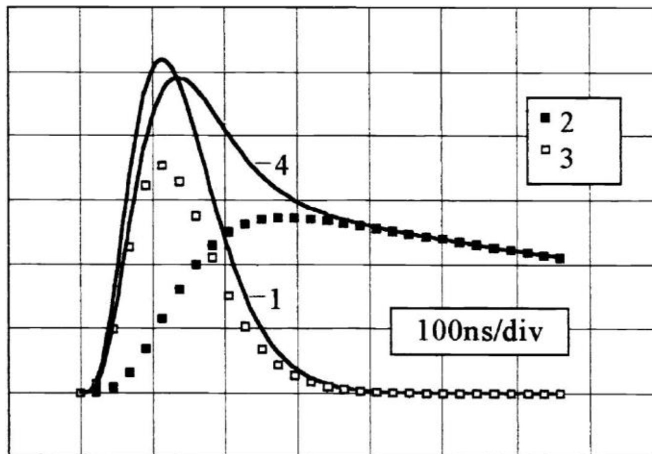

Fig. 1.23. Experimental waveforms of the CO_2 laser pulse (1) and the photovoltage across a GaAs n-n$^+$ junction (4) at T = 300 K, along with calculated curves of the fast (3) and slow (2) components (Ašmontas et al., 1999).

Furthermore, it was demonstrated that in GaAs p-n junctions under Nd:YAG laser excitation (λ = 1.064 μm), the photovoltage consists of two components of opposite polarity (Fig. 1.24): a fast hot carrier contribution and a slower generation-related component caused by two-photon absorption (Ašmontas et al., 2014). The hot carrier signal appears almost instantaneously with the arrival of the laser pulse, indicating its origin from intraband heating of free electrons in the conduction band. In contrast, the generation component develops with a noticeable delay and exhibits slower dynamics, since its formation is associated with nonlinear interband generation of electron-hole pairs.

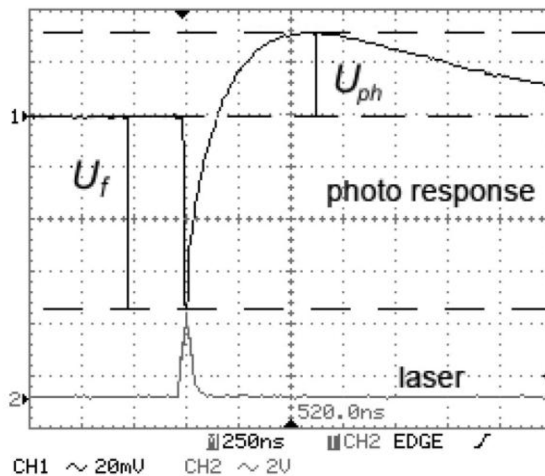

Fig. 1.24. Waveforms of the laser pulse (bottom) and the corresponding photoresponse (top) (Ašmontas et al., 2014).

It was established that the amplitude of the hot carrier signal increases linearly with excitation intensity, which confirms its nature as a result of single-photon intraband absorption (Fig. 1.25 (a)). By comparison, the generation component follows a square dependence on intensity (Fig. 1.25 (b)), which is characteristic of two-photon absorption, where two photons simultaneously interact with an electron, providing sufficient energy for the transition across the bandgap.

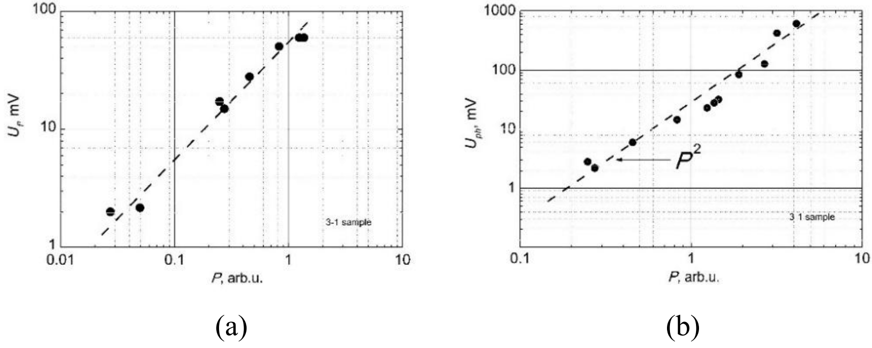

Fig.1.25. Laser-intensity dependence of hot carrier EMF (a) and photovoltage in GaAs p-n junctions (b) at 300 K (Ašmontas et al., 2014).

Additional investigations, carried out both experimentally and through modeling, revealed that the total photoresponse in GaAs p-n structures has a complex, multicomponent nature and can be decomposed into three distinct contributions (Fig. 1.26): hot carrier (U_{hc}), generation (U_{gen}), and thermal (U_{th}) (Gradauskas et al., 2020). It was shown that the hot carrier component follows the laser pulse, confirming its origin from rapid intraband heating of free carriers. The generation component appears with a short temporal delay and is associated with interband processes of electron-hole pair creation. The thermal contribution develops on much longer timescales, reflecting the transfer of energy from carriers to the phonon system, which leads to lattice heating.

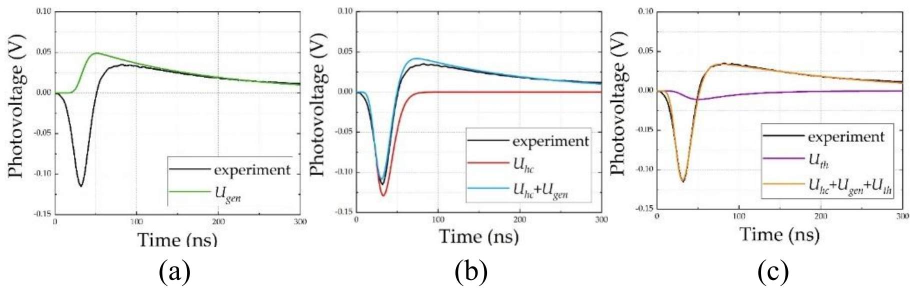

Fig. 1.26. Simulated sequence of photovoltage pulses: (a) generation-induced component (green); (b) hot carrier contribution (red) together with the combined signal of the two components (blue); (c) thermal lattice-heating contribution (violet) and the total signal including all three components (orange). The experimental photovoltage trace is shown in black for comparison (Gradauskas et al., 2020).

This decomposition allowed not only qualitative but also quantitative evaluation of the roles of different physical mechanisms in shaping the overall photovoltage. Importantly, the polarity of the hot carrier component was found to be opposite to that of the generation contribution, providing clear evidence of their distinct physical origins. The thermal component, in turn, determines the long "tail" in the signal decay.

Spectral studies confirmed that the generation-induced photovoltage in GaAs p-n junctions disappears at wavelengths $\lambda > 1.75$ μm (Fig. 1.27) since photon energies in this range are insufficient to overcome the bandgap and generate electron-hole pairs (Ašmontas et al., 2018).

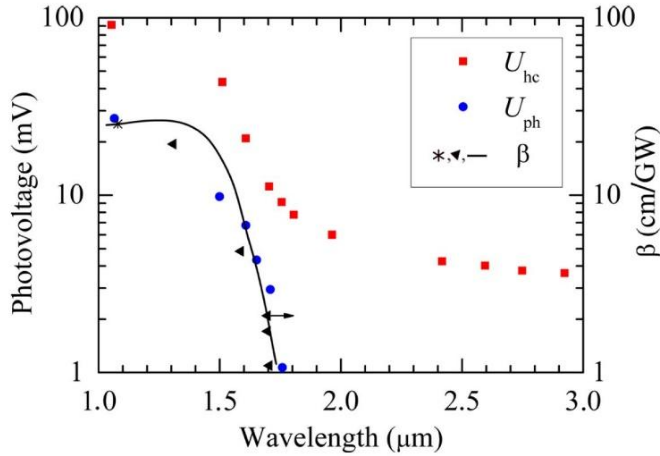

Fig. 1.27. Wavelength dependence of hot carrier photovoltage (U_{hc}) and classical photovoltage (U_{ph}) at a laser intensity of I = 0.22 MW/cm^2. Experimental points (asterisk and triangles) are compared with the theoretical solid curve of the two-photon absorption coefficient β (Ašmontas et al., 2018).

In contrast, the hot carrier component continues to appear under the same conditions. Its persistence is explained by two mechanisms: intraband absorption, in which free carriers in the conduction or valence band absorb sub-bandgap photons and are promoted to higher energy states, and the utilization of residual energy after interband transitions, which is not fully dissipated through thermalization.

Photovoltaic phenomena associated with the heating of carriers have also been investigated in GaAs/AlGaAs semiconductor heterostructures, where the presence of band discontinuities and controllable potential barriers

significantly influences the formation of the photoresponse (Ašmontas et al., 1997; Ašmontas et al., 2008; Ašmontas et al., 2003). In particular, heterostructures of the GaAs/AlGaAs type have experimentally demonstrated the emergence of hot carrier photoresponse under infrared laser irradiation with photon energies much lower than the bandgap of the base material. Under such conditions, interband generation of electron-hole pairs is absent, and the dominant interaction mechanism between the radiation and the semiconductor is intraband absorption by free carriers, which leads to an increase in their average energy and the formation of a thermoelectric photo-EMF of hot carriers. The characteristic features of the hot carrier photovoltaic response in GaAs/AlGaAs heterostructures are illustrated in Fig. 1.28.

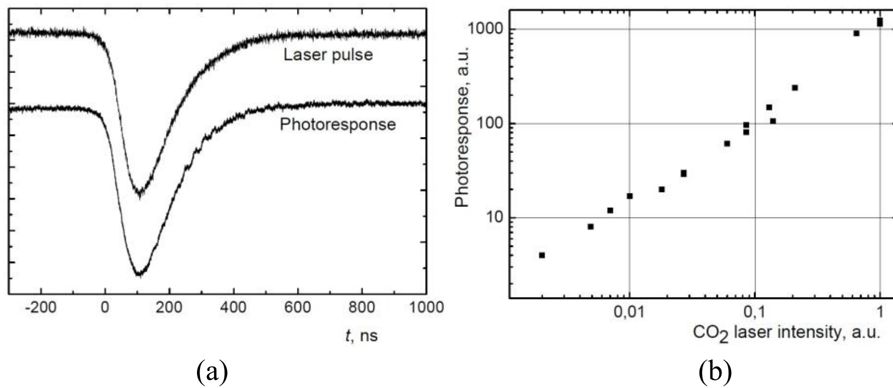

Fig. 1.28. Photoresponse of a GaAs/AlGaAs heterojunction diode under CO_2 laser irradiation: (a) temporal behaviour of the photoresponse signal induced by a CO_2 laser pulse; (b) dependence of the photoresponse on laser intensity, with the maximum intensity I_{max} = 100 kW/cm^2 (Ašmontas et al., 2008).

The figure 1.28a presents the temporal profiles of the CO_2 laser pulse and the corresponding photoresponse signal recorded across the heterojunction at room temperature. As shown, the photoresponse temporally correlates with the laser pulse, indicating its origin associated with the direct heating of free charge carriers due to intraband absorption. The dependence of the photoresponse amplitude on the excitation intensity is presented in Fig. 1.28b. The photoresponse increases almost linearly with increasing laser intensity within the investigated range. Such behavior is characteristic of photoeffects associated with the free carrier heating.

Photovoltaic effects of hot carriers were also studied in silicon p-n junctions under infrared excitation by a CO_2 laser (λ = 10.6 µm). The photon

energy in this case is approximately 0.12 eV, which is significantly lower than the bandgap of silicon. Under such conditions, interband generation of electron-hole pairs is impossible, and the primary interaction mechanism between the radiation and the material is intraband absorption by free charge carriers. It has been experimentally established that the photovoltage induced by CO_2 laser pulses in Si p^+-n diodes exhibits a complex structure and may consist of components with different polarities and distinct temporal scales (Encinas Sanz et al., 1993). A pronounced nonlinear dependence of the photoresponse on the excitation intensity was observed, with a sudden change in slope separating the low- and high-intensity regimes. Such behavior reflects the competition between carrier heating, carrier relaxation processes, and carrier generation via impact ionization in the hot carrier plasma (Encinas Sanz et al., 1993). Moreover, a pronounced dependence of the photovoltage amplitude on the junction temperature has been established, indicating the crucial role of thermal factors in the mechanism of the effect formation (Encinas Sanz & Guerra, 2003).

Further investigations of photovoltage formation across a Si p-n junction were carried out under laser irradiation of different wavelengths (Ašmontas et al., 2018). It was shown that at a wavelength of 1.489 μm, a photoresponse of two polarities is also observed, where U_f corresponds to the thermoelectromotive force of hot carriers, and U_{ph} is the classical photovoltage of opposite polarity caused by electron-hole pair generation. The oscilloscope traces presented in Fig. 1.29a clearly demonstrate the temporal separation of these two components. Similar to the case of GaAs, the classical photovoltage U_{ph} increases with increasing laser intensity according to the square law, indicating the dominant role of two-photon absorption in the sub-bandgap excitation regime. In contrast, the hot carrier thermoelectromotive force U_f shows a linear dependence on intensity, which is a characteristic feature thermal processes.

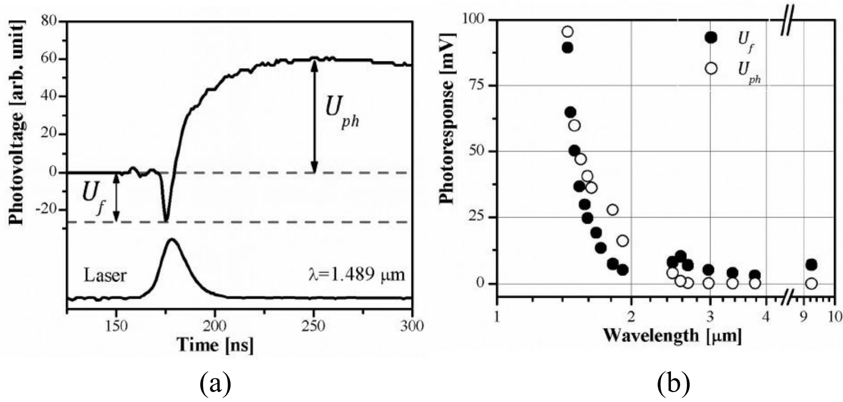

(a) (b)

Fig. 1.29. Photovoltage formation across Si p-n junction under laser irradiation: (a) oscilloscope traces of the 1.489 μm laser pulse (bottom) and the photovoltage signal (top) consisting of two components; (b) spectral dependences of the hot carrier thermoelectromotive force U_f and the classical photovoltage U_{ph} under intense laser illumination (Ašmontas et al., 2018).

It was also shown that the predominance of each component is determined by both the excitation intensity and the radiation wavelength. At low excitation levels, the hot carrier thermoelectromotive force prevails, whereas at higher intensities the generation-related contribution becomes dominant. It was demonstrated (see Fig. 1.29b) that the hot carrier contribution does not vanish with increasing wavelength, as it is governed by intraband absorption of free carriers, while the classical photovoltage decreases due to the reduction of the two-photon absorption coefficient.

The hot carrier photosignal was also detected in narrow-bandgap semiconductors under conditions of intraband excitation of free charge carriers.

$Hg_{0.8}Cd_{0.2}Te$ is a narrow-bandgap semiconductor characterized by a bandgap of approximately 0.16 eV at room temperature. This value is comparable to the photon energy of a CO_2 laser (λ = 10.6 μm, $h\nu$ = 0.12 eV). Such correspondence occurs only at temperatures close to room temperature. Unlike conventional semiconductors such as GaAs and Si, in which the bandgap decreases with increasing temperature, $Hg_{1-x}Cd_xTe$ exhibits an inverse temperature dependence of E_g (Rogalski, 2005). For the composition x = 0.2, the bandgap at liquid nitrogen temperature (80 K) is approximately 0.09 eV, which is lower than the photon energy of the CO_2 laser. Under these conditions, cooling the $Hg_{0.8}Cd_{0.2}Te$ p-n junction to 80 K enables

simultaneous observation of both the classical interband absorption-caused photocurrent and the hot carrier contribution in the total photoresponse (Ašmontas et al., 2002). Figure 1.30 presents the temporal profile of the CO_2 laser pulse together with the corresponding photoresponses measured across the $Hg_{0.8}Cd_{0.2}Te$ sample at various laser intensities.

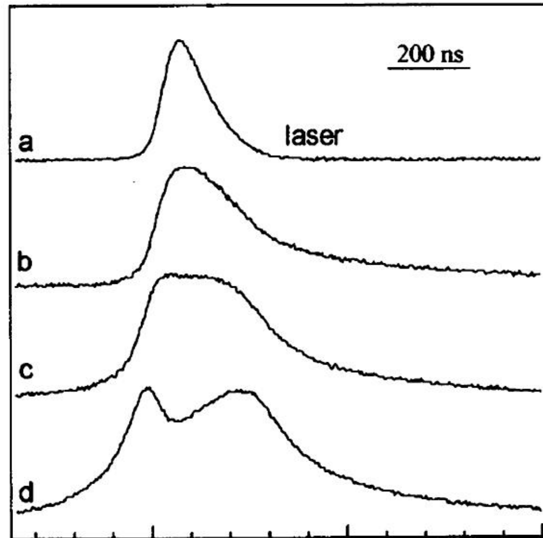

Fig. 1.30. Temporal profiles of the laser pulse (a) and the corresponding photoresponses (b–d), recorded at progressively increasing laser intensities from low to high (Ašmontas et al., 2002).

At low excitation intensities (see Fig. 1.30b), a classical photoresponse caused by interband absorption was observed. With increasing excitation intensity (Fig. 1.30c), the classical photovoltage became saturated due to the limitation imposed by the potential barrier height. A further increase in intensity led to the appearance of a photoresponse component of opposite polarity, as shown in Fig. 1.30d. This negative component originated from carrier heating under strong illumination. Importantly, the hot carrier signal fully followed the temporal profile of the laser pulse. The intensity dependences of both the classical and the hot carrier signals were approximately linear within their respective regimes (Ašmontas et al., 2002).

A similar behavior was also observed in InSb, which has a bandgap of approximately 0.23 eV at 80 K, where E_g exceeds the photon energy of the CO_2 laser (Ašmontas et al., 2003). At moderate intensities, the photovoltage

corresponded to the classical response associated with electron-hole pair generation via two-photon absorption, as evidenced by its square dependence on laser intensity. The amplitude of the classical photovoltage was limited by the potential barrier height. A further increase in intensity led to the appearance of a hot carrier component of opposite polarity. This component originated from carrier heating and their diffusion across the potential barrier. Reducing the barrier height by applying a forward bias resulted in the emergence of the hot carrier signal at lower excitation intensities. Thus, in InSb, both classical and hot carrier photoresponses could be observed simultaneously, with their relative contributions determined by the excitation intensity and the potential barrier height (Ašmontas et al., 2003).

The reviewed literature shows that, despite major advances in photovoltaics, single junction solar cells remain fundamentally constrained by intrinsic loss mechanisms. According to the Shockley–Queisser theory, spectral and thermalization losses dominate these limitations, accounting for up to 80% of intrinsic energy dissipation. Although approaches to reach or exceed this limit are typically described as methods for reducing these losses, both can also be interpreted through the lens of hot carrier physics. Spectral losses, or nonabsorption of low energy photons, contrast with experimentally observed intraband absorption, where free carriers absorb infrared radiation and generate a hot carrier photocurrent across a p-n junction or other potential barrier. Thermalization losses, in turn, result from the dissipation of excess hot carrier energy to the lattice after high energy photon absorption.

Modern efficiency enhancement strategies can therefore be viewed not only as pathways to surpass the Shockley–Queisser limit but also as means of reducing the negative impact of hot carriers on the total photoresponse. The total photoresponse of a p-n junction is a superposition of three components: classical electron-hole generation, the hot carrier thermoelectromotive force, and the lattice heating-induced component, the latter two having opposite polarity to the classical response. These mechanisms have been observed in both wide bandgap (GaAs, Si) and narrow bandgap (HgCdTe, InSb) semiconductors, with their relative contributions governed by temperature, excitation wavelength, barrier height, and bias. Still, a systematic analysis of hot carrier photocurrent as a function of temperature, bias, and excitation spectrum is still required.

At the same time, the hot carrier phenomenon offers promising opportunities for infrared sensing based on intraband excitation of free carriers. Unlike conventional narrow bandgap photodetectors that require cryogenic cooling to suppress dark current and maintain p-n junction functionality, devices exploiting controlled barrier hot carrier transport may

operate at room temperature, significantly broadening their practical applicability.

These considerations define the scientific motivation and justify the methodological approaches developed in the following chapters of the dissertation.

2. METHODOLOGY

The theoretical part focuses on the modeling of advanced photovoltaic structures by solving the coupled one-dimensional Poisson & Schrödinger equations by means of software 1D Poisson, allowing for the determination of the energy band diagrams. This provides an effective model for predicting carrier dynamics and photovoltaic characteristics in novel device architectures. The experimental part is based on two fundamental techniques: the measurement of current-voltage (I-V) characteristics of semiconductor junctions under varying external conditions and registration of photoelectric response induced by pulsed laser radiation. Within this concept, two main tasks are pursued: (a) investigation of the mechanisms of photovoltage component formation across a p-n junction and their dependence on temperature, applied bias, and excitation wavelength and intensity; (b) photoelectrical characterization of the developed ratchet sensor, allowing evaluation of its functional performance and correlation with theoretical predictions.

2.1. Structure simulation and fabrication

Semiconductor samples were fabricated using liquid phase epitaxy (LPE) and molecular beam epitaxy (MBE) techniques to grow structures based on GaAs and GaAs/$Al_xGa_{1-x}As$ compounds. For MBE, the development procedures of layered structures were pre-optimized by Schrödinger–Poisson simulations with the Poisson 1D software, enabling the determination of band diagrams and carrier distributions within the layers. This approach provided validation for novel structures without requiring labor-intensive technological pre-testing and simplified the prediction of the electrical characteristics of the samples. During the simulations of the ratchet-based sensor, the parameters of each layer were defined, including the AlAs mole fraction in $Al_xGa_{1-x}As$, conductivity type (n), doping carrier concentration, and layer thickness (see Fig. 2.1). These inputs allowed for the reconstruction of the potential distribution and band structure, which determine the operational characteristics of the semiconductor structures.

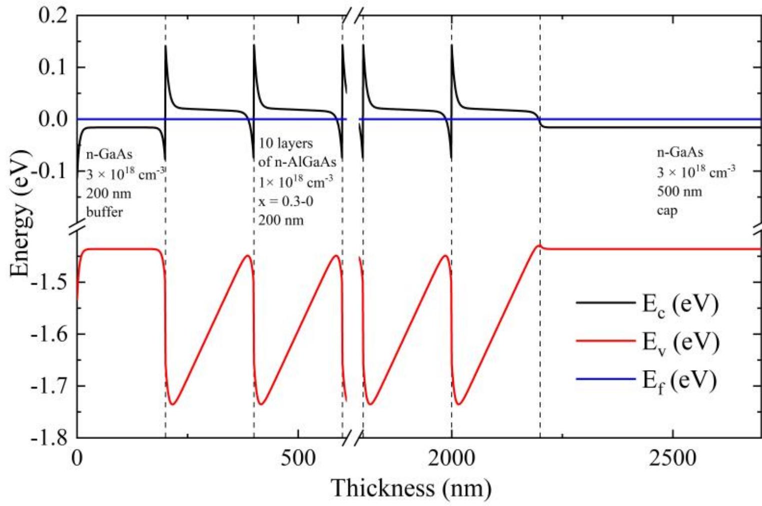

Fig. 2.1. Energy band diagram of ratchet-based sensor.

The MBE technique relies on the deposition of monocrystalline layers at ultra-high vacuum (<10^{-8} Torr) using highly pure Ga, As, and Al supplied from effusion cells as molecular beams. The regulation of growth rate, composition, dopant concentration, and layer thickness occurs at the atomic layer level, allowing high-quality purity and reproducibility. The LPE process entails the deposition of layers from high-temperature melts within a quartz furnace. The semiconductor substrate is partially dissolved in the melt, resulting in the crystallization of a crystalline layer on its surface. This technology ensures faster growth and enables the formation of comparatively thick layers, while it is inferior to MBE regarding purity and precision control. The thickness of the epitaxial layers was determined by optical microscopy of cross-sections, whereas the electrical characteristics (electron concentration and mobility) were evaluated using the Van der Pauw method at both room and temperatures.

2.2. Investigated samples

2.2.1. Industrial polycrystalline silicon solar cells

The samples were prepared from industrial polycrystalline silicon solar cells (SoliTek, Vilnius, Lithuania). The emitter and base regions had carrier concentrations of approximately $n \approx 10^{20}$ cm^{-3} and $p \approx 10^{16}$ cm^{-3}, respectively. The cells were diced into pieces of 2×2 mm^2. To prevent the generation of a

photoresponse at the metal contacts, the contacts were positioned at the edges of the samples. A schematic view of the layered structure is shown in Fig. 2.2.

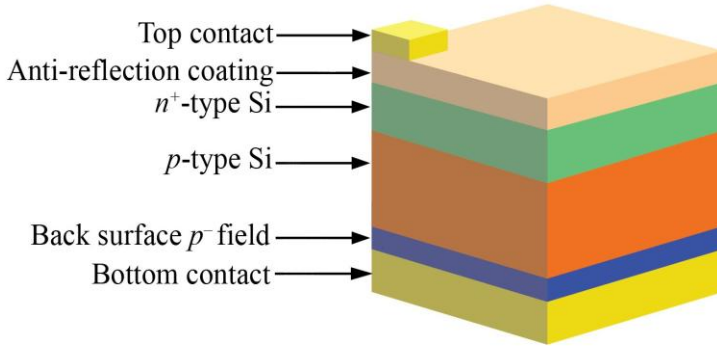

Fig.2.2. Layered structure of a polycrystalline silicon solar cell.

2.2.2. GaAs p-n junction structure

The GaAs p-n junction consisted of a 5 μm-thick p-type layer grown by liquid-phase epitaxy on an n-type substrate, with hole and electron densities of 5×10^{17} cm^{-3} and 3×10^{17} cm^{-3}, respectively. A thin, heavily doped p$^+$ layer with a hole concentration of 2×10^{18} cm^{-3} was produced to guarantee reliable ohmic contact. The device fabrication employed standard photolithography, succeeded by thermal evaporation and annealing of Au-Ge-Ni ohmic contacts. To prevent direct illumination and the formation of unwanted photoresponses at the top p-p$^+$ and semiconductor–metal contacts, the p$^+$ layer was selectively etched away, leaving it solely beneath the metal contacts. The contacts were positioned at the edge of the 2.5 × 2.5 mm^2 sample. The layout of the GaAs p-n junction with ohmic contacts is shown in Fig. 2.3.

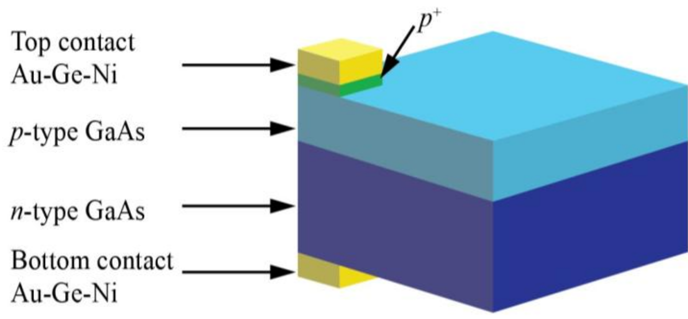

Fig. 2.3. Design of the semiconductor sample based on a GaAs p-n junction.

2.2.3. Ratchet-based sensor

The structures were MBE-grown up on an n-type GaAs substrate with an electron concentration of 3 × 10^{18} cm^{-3}. An additional 200 nm-thick n-type GaAs buffer layer with equal doping concentration was deposited to improve the crystalline quality. The active region consisted of ten $Al_xGa_{1-x}As$ layers, each 200 nm thick (total thickness 2 μm), with the AlAs mole fraction (x) progressively decreasing from 0.3 to 0. The electron density in these layers was sustained at 1 × 10^{18} cm^{-3}. A 500 nm-thick n-type GaAs cap layer, with an electron concentration of 3 × 10^{18} cm^{-3}, was deposited atop the active region to achieve structural and electrical symmetry. Ohmic contacts were defined using photolithography, followed by thermal evaporation and annealing of an Au-Ge-Ni alloy, which provided low-resistance electrical connections. To avoid parasitic photoresponses, the contacts were positioned along the periphery of the samples. Fig. 2.4 illustrates the schematic architecture of the GaAs/$Al_xGa_{1-x}As$ sensor structure.

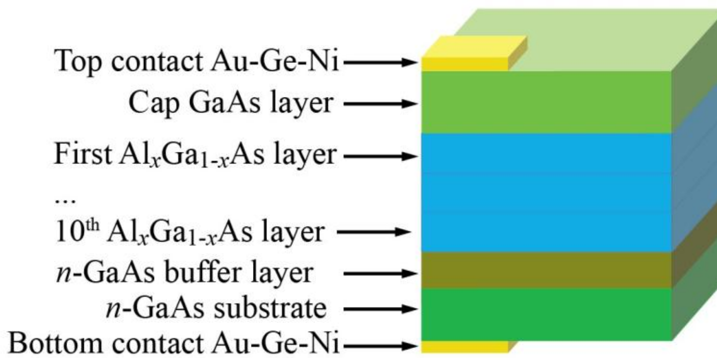

Fig. 2.4. Layout of the GaAs/$Al_xGa_{1-x}As$ multiheterostructure for the ratchet sensor

2.3. Experimental setup

2.3.1. Analysis of electrical properties of samples in direct current regime

Measurements of the semiconductor samples in direct current (DC) mode were conducted utilizing a probe station. This method involves positioning the probes on the sample's ohmic contacts and determination of key electrical

properties of the semiconductor structure, such as current-voltage characteristics and electrical resistance.

The I-V characteristic is one of the primary tools for evaluating the fundamental electrical parameters of semiconductor samples, as it describes the dependence of current flow on the applied voltage. In this work, I-V measurements were performed using the DC probe station "SUSS Microtec EP6" equipped with "SUSS Microtec PH110" probes and precision measurement equipment, specifically the I-V analyzer "Agilent E5270B" with "Agilent E5287A" modules. A schematic block diagram of the measurement setup is shown in Fig. 2.5. Each probe was connected to the I-V analyzer slots (Fig. 2.5–1) via BNC coaxial cables. The probes were positioned on the ohmic contacts of the diode using the probe station (2).

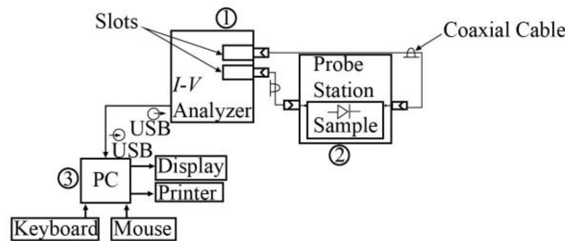

Fig. 2.5. Schematic block representation of the probe station setup for I-V measurements.

The measurements were controlled by the PC software "Agilent EasyExpert", which provided options to configure the voltage range, step size, and probe polarity. The controlling PC (3) was connected to the I-V analyzer using USB, and the virtual control interface is illustrated in Fig. 2.6. The resulting I-V characteristics were obtained for each sample.

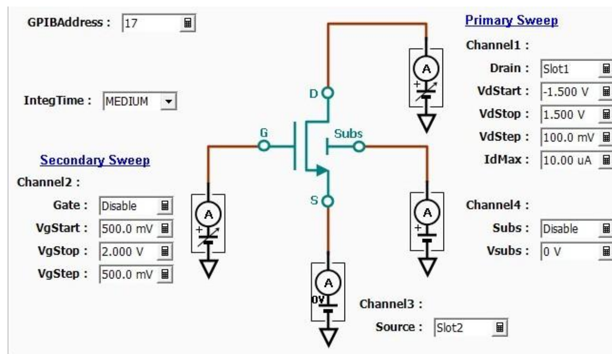

(a)

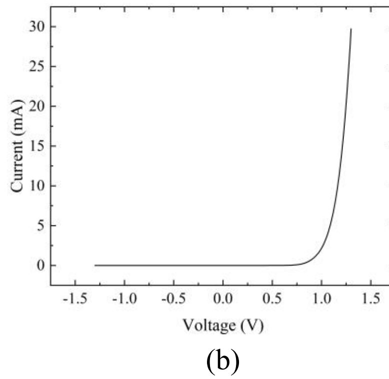

(b)

Fig. 2.6. View of the "Agilent EasyExpert" PC software: (a) settings for I-V characterization, (b) experimentally obtained I-V characteristic.

2.3.2. Measurement scheme and equipment

The photoelectrical study employed a specialized measurement circuit, laser sources with defined wavelengths, and temperature-regulated conditions to examine, characterize, and analyze the hot carrier effect in GaAs p-n junction diodes, industrial polycrystalline silicon solar cells, and the ratchet-based sensor. Figure 2.7 illustrates the schematic diagram of the measurement circuit.

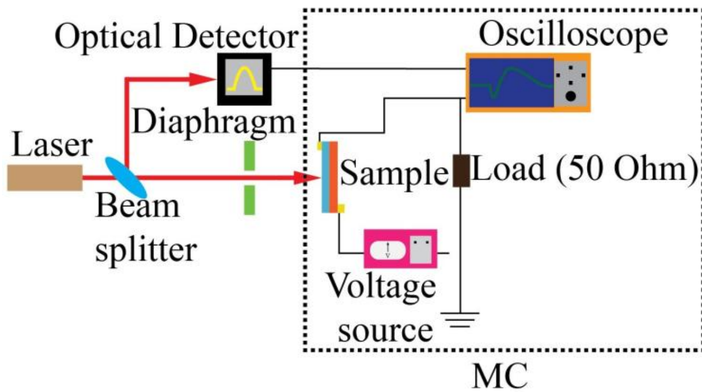

Fig. 2.7. Structural diagram for investigating photocurrent across the sample. Dashed rectangle indicates the measurement circuit (MC).

All measurements were conducted in the photocurrent regime. Four different lasers were employed to illuminate the samples. A load resistor (R = 50 Ω) was used to ensure impedance matching of the circuit and to obtain

reliable time-resolved characteristics of the photoresponse. A custom-built DC voltage source (0–9 V, 0–0.3 A) was used to provide the bias voltage during the measurements. The measurement circuit used to investigate the influence of different excitation wavelengths comprised the sample, a 50 Ω load resistor, a digital storage oscilloscope, and a DC voltage source (see Fig. 2.7). The temporal profiles of both the photovoltage and the laser pulse were recorded with a digital storage oscilloscope "DSO6102A" (Agilent Technologies Inc., Santa Clara, CA, USA), offering registration accuracy of ± 2.0% full scale (vertical/voltage), ± 0.0015% (horizontal/time), and a time resolution of 2.5 ps. The laser pulse shape was simultaneously observed using a high-speed optical signal reference detector "11HSP-FS1" (Standa Ltd., Vilnius, Lithuania). The experiments were conducted within a temperature range of 80–300 K. Low-temperature conditions were ensured using a custom-built optical cryostat.

2.3.3. Optical schemes of lasers for investigation

The excitation wavelength of 0.532 μm, corresponding to a photon energy of 2.32 eV, was employed in order to probe the hot carrier effect when the incident photon energy is greater than the bandgap of the investigated structures. For excitation of the samples, a diode-pumped, frequency-doubled neodymium-doped yttrium aluminium garnet (Nd:YAG) laser with an LBO nonlinear crystal NL202 (Ekspla Ltd., Vilnius, Lithuania) was employed. The laser generated 7–12 ns-long pulses at a wavelength of 532 nm with a repetition rate of 50 Hz. A harmonic separator (dichroic beamsplitter; Eksma Ltd., Vilnius, Lithuania) was used to eliminate the residual infrared radiation and transmit the 532 nm beam. A part of the radiation was directed to an optical reference detector (Standa Ltd., Vilnius, Lithuania) via a beam splitter plate. The beam power was adjusted using a variable attenuator (Eksma Ltd.) consisting of a Brewster-type polariser and a quartz half-wave plate. The average power of the radiation was measured with an optical power meter PM400 (Thorlabs Inc., Newton, NJ, USA). The maximum pulse power was about 0.414 MW/cm^2. The laser beam was directed onto the sample in the measurement circuit (MC) using a detachable beam splitter plate (BSP). The schematic block diagram of the experimental system is presented in Fig. 2.8.

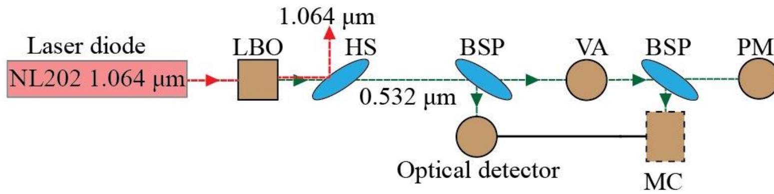

Fig. 2.8. Block scheme of the measurement system used for experiments with 532 nm laser irradiation. Labels: NL202 – diode-pumped Nd:YAG laser, LBO – nonlinear crystal for second harmonic generation; HS – Nd:YAG harmonic separator; BSP – beam splitter; VA – variable attenuator for the 532 nm beam; MC – measurement circuit with the sample; PM – optical power meter.

Laser radiation of a wavelength of 1.064 μm was selected with respect to the GaAs bandgap width of 1.42 eV. The corresponding photon energy of 1.16 eV is lower than the bandgap energy. As the source of 1.064 μm radiation, a neodymium-doped yttrium aluminium garnet (Nd:YAG) laser was employed, operating with pulses of 10–17 ns duration, a repetition rate of 50 Hz, and a maximum pulse intensity of 10 MW/cm^2. The schematic diagram of the experimental setup is shown in Fig. 2.9.

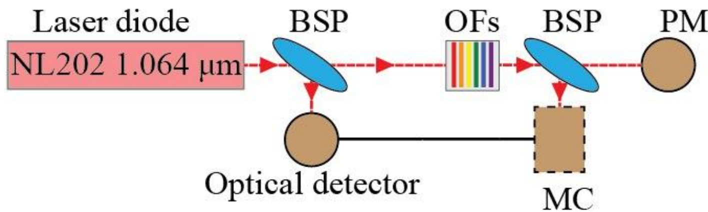

Fig. 2.9. Experimental setup for measurements under laser irradiation at 1.064 μm wavelength. Labels: BSP – beam splitter plate; OFs – set of optical filters; PM – optical power meter; MC – measurement circuit with the sample.

The laser output power was modified using optical filters with varying transmission coefficients at a wavelength of 1.064 μm. The sample was illuminated by the laser beam through a detachable beam splitter plate (BSP). The average power of the radiation was measured using an optical power meter, and the pulse power was later computed by considering the repetition rate and pulse duration.

A laser with a wavelength of 1.342 μm (photon energy 0.92 eV) was chosen based on the bandgap of polycrystalline silicon, which is approximately 1.1 eV. This wavelength was selected specifically to prevent single-photon excitation of electron-hole pairs. The radiation source was a neodymium-doped yttrium orthovanadate ($Nd:YVO_4$) diode laser functioning at 1.342 μm, with a pulse duration of 1.7 ns and an intensity range of 0.06 kW/cm^2 to 0.4 MW/cm^2. The output intensity was controlled by varying the laser pump power. Schematic diagram of the laser system with the sample within the measurement circuit (MC) is shown in Fig. 2.10.

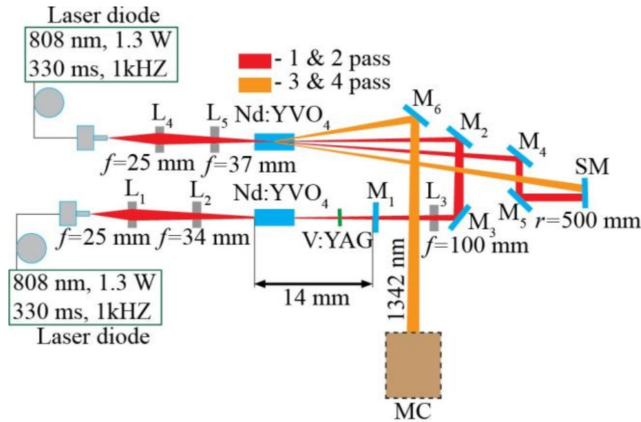

Fig. 2.10. Schematic diagram of the $Nd:YVO_4$ laser system used to generate radiation at 1.342 μm. Labels: L – lenses; M – mirrors; SM – spherical mirror (R = 500 mm); MC – measurement circuit with the sample. Red lines represent the first and second passes of the beam, while yellow lines correspond to the third and fourth passes.

Additional experiments were performed using laser excitation at a wavelength of 2 μm, which corresponds to a photon energy of 0.62 eV. This value is more than twice lower than the bandgap of GaAs ($E_g \approx 1.42$ eV), thus preventing the generation of electron-hole pairs through one- and two-photon absorption. The schematic layout of the laser system is presented in the referenced work: Augustinas Petrulėnas, Femtosecond Pulse Generation in the 1.1–3 μm Range by Parametric and Stimulated Raman Amplification of Supercontinuum (Petrulėnas, 2025). The excitation parameters during the experiment were defined by ultrashort pulses with a duration of ~0.5 picoseconds and an intensity range of 1.76–3 MW/cm^2, which allowed reproducing the conditions of extremely fast processes in the semiconductor structure.

3. RESULTS AND DISCUSSION

3.1. Spectral Analysis of Hot Carriers

The photoresponse in semiconductor solar cells is primarily determined by the solar spectrum, as electron-hole pairs are generated through the absorption of photons with energies equal to or exceeding the bandgap E_g. According to the Shockley–Queisser theory, photons with energies below E_g are not absorbed by the material and therefore do not contribute to carrier generation. When the photon energy exceeds E_g, electron-hole pairs are generated with excess energy. This extra energy does not contribute to carrier generation but is instead dissipated into the crystal lattice. As a result, part of the absorbed photon energy is lost to lattice heating, which reduces the overall efficiency of a solar cell.

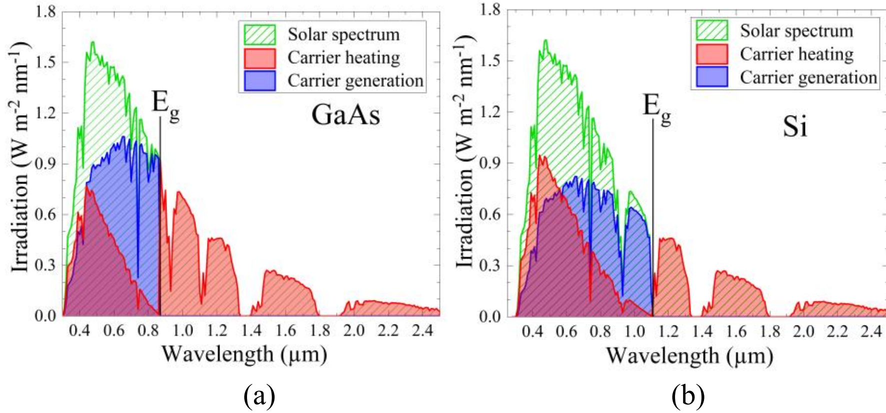

Fig. 3.1. Solar spectrum AM1.5 (green oblique-lined area), and its potential contribution to electron-hole pair generation (blue area) and carrier heating in GaAs (a) and Si (b). Red areas illustrate the portion of the spectrum corresponding to carrier heating by photons with energies exceeding the bandgap ($hv - E_g$), and photons with energies below the bandgap ($hv < E_g$).

The wavelength (or photon energy) determines the characteristics of both hot carrier formation and the generation-related photoresponse. In the context of the proposed model (Fig. 3.2), four mechanisms regulating photocurrent rise can be defined: conventional interband electron-hole pair generation (process 1), free-carrier heating through intraband light absorption (process 2), simultaneous electron-hole pair generation and carrier heating via two-photon absorption of below-bandgap photons (process 3), and combined

electron-hole generation with carrier heating induced by absorption of photons with energies exceeding the bandgap (process 4).

Thus, hot carriers can be generated by photons with energies both below and above the semiconductor bandgap. Although the free-carrier absorption coefficient is considerably smaller than the interband one, the existence of such heating and the formation of a pre-thermalized HC electrical response have been experimentally verified in semiconductor structures (Fig. 3.2, process 2). For instance, irradiation with a CO_2 laser ($h\nu = 0.12$ eV) induced HC photocurrent in Ge, Si, and GaAs p-n junctions with bandgaps of 0.66, 1.12, and 1.42 eV, respectively (Umeno et al., 1978; Ašmontas et al., 2017; Ašmontas et al., 1997). Also, spectral investigations revealed appearance of HC photovoltage under illumination with higher-energy photons (Ašmontas et al., 2018).

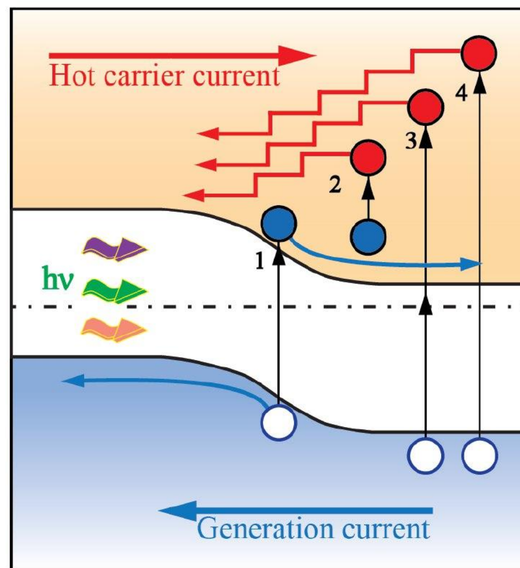

Fig. 3.2. Schematic illustration of the generation-induced (blue) and hot carrier (red) photocurrent across the p-n junction. Stepped arrows represent the cooling and diffusion of hot electrons; analogous processes involving hot holes are not shown to maintain visual clarity.

To investigate the properties of hot carriers at different wavelengths (spectral characteristics), laser irradiation with wavelengths of 532 nm, 1.064 μm, and 1.342 μm was employed. These values were selected with respect to the bandgap widths of the investigated materials, GaAs and Si:

1. Radiation at a wavelength of 532 nm provides photons with an energy of 2.34 eV, which significantly exceeds the bandgaps of both GaAs and Si. Under these conditions, interband generation of electron-hole pairs takes place, while the surplus energy, $hv - E_g$, equal to 0.92 eV for GaAs and 1.22 eV for Si, is used for carrier heating (Fig. 3.2, process 4).
2. At a wavelength of 1.064 μm, the photon energy is 1.16 eV. For GaAs, this value is below the bandgap, which prevents direct interband generation, only two-photon absorption is possible, with the excess energy of $2hv - E_g = 0.9$ eV (Fig. 3.2, process 3). Additional carrier heating may also occur via the intraband light absorption (Fig. 3.2, process 2). For Si, this photon energy is close to the bandgap edge, which enables interband generation together with carrier heating, $hv - E_g = 0.04$ eV (Fig. 3.2, process 4).
3. At a wavelength of 1.342 μm, the photon energy is 0.92 eV, which lies below the bandgap of both materials. In this case, interband generation is possible only through two-photon absorption, with excess energies of $2hv - E_g$ equal to 0.42 eV for GaAs and 0.72 eV for Si, respectively (Fig. 3.2, process 3). Carrier heating under these conditions may arise from both intraband absorption and the above-mentioned extra energy (Fig. 3.2, processes 2+3).

The hot carrier photocurrent exhibits several characteristic features. Its polarity indicates carrier transport against the potential barrier and contrasts with that of the generation process. In addition, it demonstrates a linear dependence on excitation power and responds rapidly to laser pulses. The temporal dynamics of the hot carrier effect is fundamentally determined by the carrier energy relaxation time, which is on the picosecond scale (Zhang et al., 2021; Dargys & Kundrotas, 1994).

Figure 3.3 presents the I-V characteristics of the GaAs p-n sample under 1.064 μm laser irradiation of 0.7 MW/cm^2 intensity at room temperature. The inset displays a representative oscilloscope trace of the photoresponse consisting of two components with opposite polarities. The negative photocurrent component (see inset in Fig. 3.3) is interpreted as a manifestation of the hot carrier effect for two reasons: (a) its rapid behavior is governed by the carrier energy relaxation time, and (b) its polarity corresponds to carrier transport across the p-n junction barrier in the opposite direction, as illustrated by the red stepped arrows in Fig. 3.2.

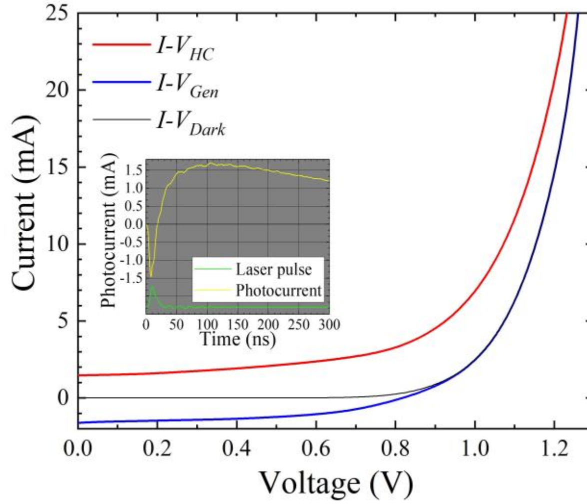

Fig. 3.3. I-V characteristics of the GaAs p-n junction in the dark (black line) and under illumination: the red line represents the HC photocurrent, and the blue line signifies the generation photocurrent. The inset shows a typical oscilloscope trace of a photocurrent pulse composed of two components, negative and positive, and a laser pulse below (not to scale) (Ašmontas et al., 2024).

The contribution of the lattice heating-induced component was disregarded because of its minor role in the total photocurrent (Gradauskas et al., 2020). Due to the opposite polarities of the generation-related (blue) and hot carrier (red) photocurrents, their competition is evident in the current-voltage characteristics, with both components being strongly affected by the applied bias.

The magnitude of the hot carrier photocurrent increases with applied forward bias (Fig. 3.4). At around 0.7 V, the dependence exhibits a characteristic inflection point, after which the photocurrent starts rising sharply. This exponential growth results from the transition of the pulsed displacement current, which occurs under reverse and low forward biases, to the transport of hot carriers across the p-n junction barrier lowered by the applied voltage. The displacement photocurrent of hot carriers is analogous to the alternating current flowing through a capacitor and appears only under pulsed carrier heating followed by junction recharging (Ašmontas et al., 1997). A further increase in forward bias leads to the saturation of the hot carrier photocurrent due to the reduction of the potential barrier (Umeno et al., 1978).

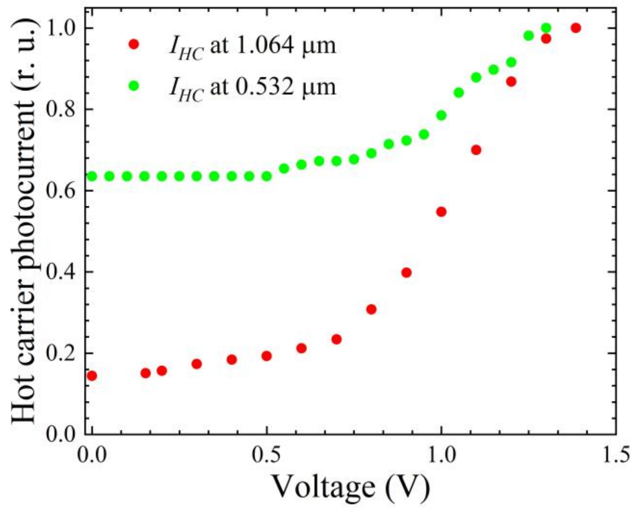

Fig. 3.4. Bias-voltage dependence of the normalized hot carrier photocurrent across GaAs p-n junction measured at room temperature under excitation at 532 nm (green) and 1.064 µm (red) laser wavelength.

Fig. 3.5 presents the current-voltage characteristics under laser illumination at different wavelengths, all maintained at the same intensity.

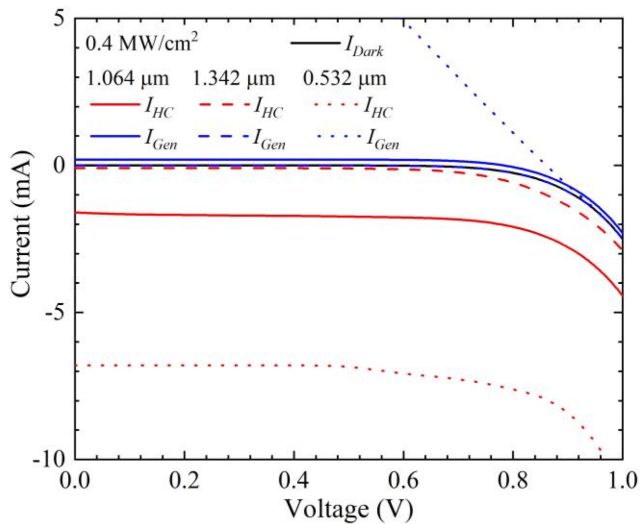

Fig. 3.5. I-Vs of GaAs p-n junction exposed to 0.4 MW/cm^2-intense laser radiation of 1.064 µm (solid lines), 1.342 µm (dashed lines) and 0.532 µm wavelength (dotted lines) at room temperature (Gradauskas et al., 2024).

Photons with wavelength of 1.342 μm (0.92 eV) predominantly contribute to the hot carrier photocurrent, as their energy is insufficient to produce a noticeable generation-related response. At 1.064 μm (1.16 eV), the hot carrier component prevails over the classical photocurrent originating from two-photon absorption. This behavior can be explained by the surplus energy of 0.9 eV remaining after the formation of an electron-hole pair through the conventional interband mechanism, which is further used for carrier heating. Under irradiation with photons of 0.532 μm (2.32 eV, above the GaAs bandgap), a significant hot carrier photocurrent is also detected, which contradicts classical expectations. This effect is most likely associated with the residual 0.92 eV energy retained after the single-photon interband absorption process.

As Fig. 3.6 shows, the spectral characteristics of the two photocurrent components exhibit ambiguos behavior. When the excitation intensity is kept constant but the photon energy is reduced (wavelength of 1.342 μm instead of 1.064 μm), the generation-related component I_{Gen} almost completely disappears, whereas the hot carrier component I_{HC} also decreases, though to a lesser extent. Such a reduction cannot be explained solely by the free-carrier absorption mechanism, which in the classical approximation follows the $\propto \lambda^2$ law (Szuszkiewicz, 1996).

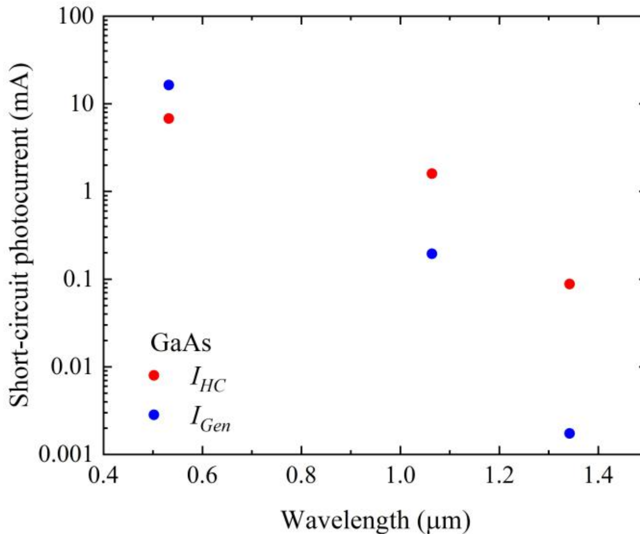

Fig. 3.6. Spectral dependence of short-circuit hot carrier (red dots) and carrier generation (blue dots) photocurrents of GaAs p-n junction exposed to 0.4 MW/cm^2-intense laser light at room temperature (Gradauskas et al., 2024).

This indicates that carrier heating, and thus the formation of the hot carrier photocurrent, is additionally governed by the residual energy left after two-photon absorption: lowering the photon energy from 1.16 eV to 0.9 eV results in a decrease of the excess energy from 0.92 eV to 0.42 eV. Under shorter-wavelength excitation (0.532 µm instead of 1.064 µm), interband single-photon absorption becomes dominant, leading to an enhancement of the generation-related photocurrent component. At the same time, the residual photon energy of about 0.92 eV continues to contribute to free-carrier heating, emphasizing the complex interplay between generation-induced and hot carrier mechanisms.

Figure 3.7 presents the typical temporal profiles of the photocurrent pulse across the silicon p-n junction under conditions of zero external bias (green curve) and under a forward bias of +0.4 V (olive curve), when excited by a 1.342 µm laser pulse (bottom pink curve) at room temperature.

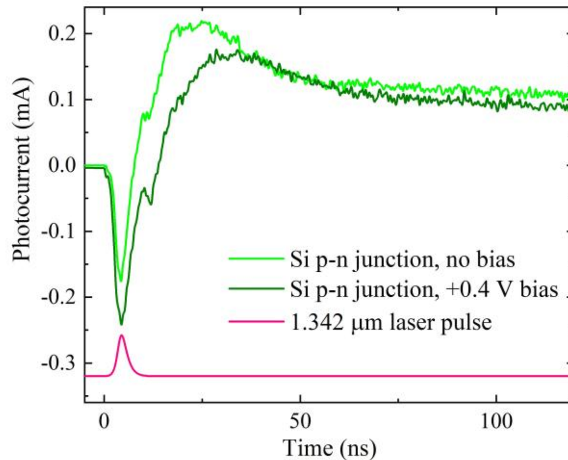

Fig. 3.7. Typical shapes of photocurrent pulse under conditions of no (green) and forward +0.4 V (olive) bias voltage under the excitation of 1.342 µm wavelength laser pulse (below in pink). Room temperature. Laser pulse shown not to scale. (Gradauskas et al., 2024).

It can be seen that the temporal shape of the response is also composed of several components. The fast rise of the initial subpulse, as well as its direction, clearly indicate that this component can be attributed to the hot carrier photocurrent I_{HC}. Application of the forward bias works in favour of the hot carrier photocurrent across the lowered potential barrier, and suppresses the generation current.

Figure 3.8 shows the dependence of the peak values of the photocurrent subpulses on the applied voltage. A sharp increase of the hot carrier component I_{HC} above a forward bias of 0.5 V is particularly noteworthy. Similar behavior has also been reported by other authors (Marmur & Oksman, 1975; Umeno et al., 1978; Ašmontas et al., 2017), which confirms the universality of the effect. This steep rise is interpreted as the achievement of favorable conditions for hot carriers to cross the junction associated with a lowering of the potential barrier height.

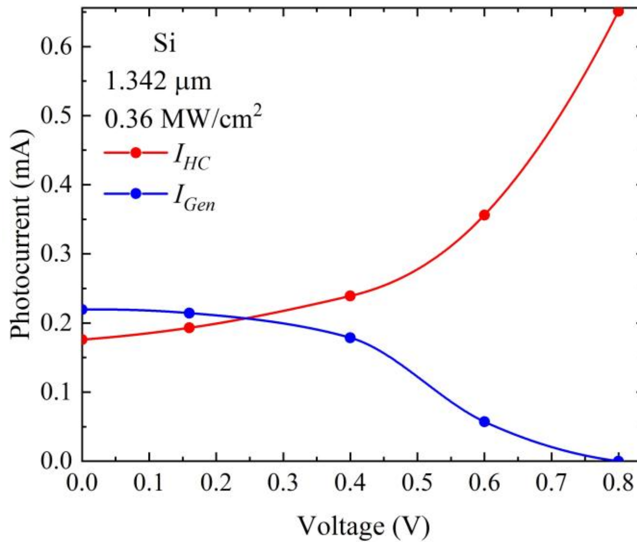

Fig. 3.8. Hot carrier photocurrent (red) and generation photocurrent (blue) vs. bias voltage at room temperature (Zharchenko et al., 2024).

These findings demonstrate the decisive role of forward bias in the formation of the hot carrier photocurrent in Si p-n junctions. It reduces the barrier for carrier injection and provides the conditions for rapid carrier transport across the junction, which is manifested in the steep rise of the photocurrent.

In a silicon p-n junction, the hot carrier photocurrent induced by radiation with a wavelength of 1.064 μm (photon energy above the band gap) is not observed under the short-circuit conditions. Its appearance is detected only at sufficiently high forward bias ~0.8 V (see insert Fig. 3.9), when the potential barrier becomes low enough for hot carriers to cross, while the contribution of the generation photocurrent is relatively weak. When the excitation wavelength is increased to 1.342 μm, the amplitude of the generation

photocurrent decreases, whereas the hot carrier component is enhanced (Fig. 3.9).

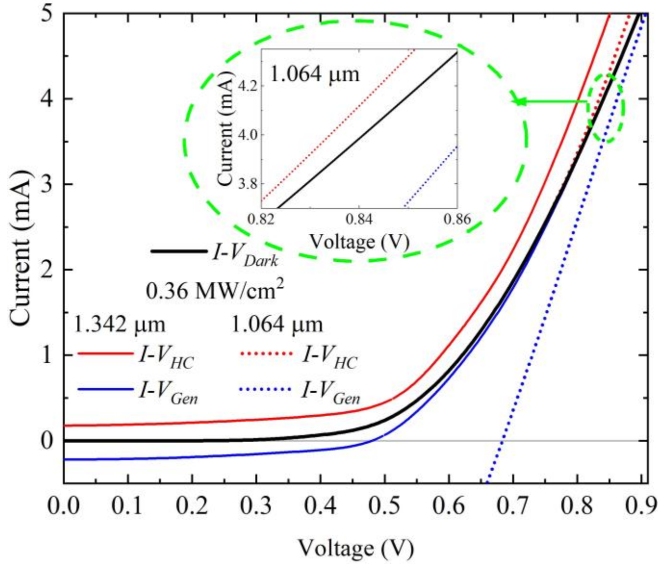

Fig. 3.9. Current-voltage characteristics of the Si solar cell at room temperature. In the inset: enlarged high-bias region of I-V curves under 1.064 μm illumination (Zharchenko et al., 2024).

This different response of the hot carrier photocurrent to long-wavelength excitation in Si compared to GaAs is most likely related to the steeper spectral dependence of interband absorption near the bandgap edge, which leaves a larger excess energy available for intraband free-carrier heating. Additional experiments with Si under 0.532 μm excitation revealed no hot carrier photocurrent. The intense interband absorption of photons with energies $h\nu \geq 2E_g$ fully suppresses the contribution of the hot carrier photocurrent.

3.2. Influence of laser intensity on the formation of hot carrier photoresponse

In p-n junctions, the illumination-induced photocurrent is formed as a superposition of three distinct components. The first one, U_{Gen}, is associated with electron-hole pair generation, i.e., it corresponds to the classical photovoltage. The second component, U_{HC}, exhibits polarity opposite to the classical one and reproduces the temporal profile of the laser pulse. The third

component, U_T, has the same polarity as U_{HC} but develops much more slowly. (Gradauskas et al., 2020).

Laser excitation of GaAs samples was carried out at 1.064 μm with different intensities, and the corresponding typical photoresponses are presented in Fig. 3.10.

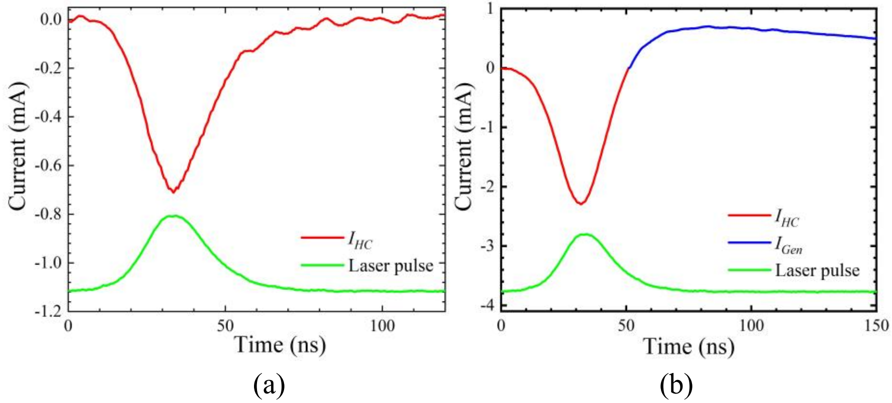

Fig. 3.10. Typical photoresponse pulse under low (a) and high (b) laser intensities at room temperature. Laser pulse shown not to scale (Gradauskas et al., 2024).

The negative-polarity pulse observed in the photoresponse can be interpreted as a superposition of the hot carrier component, I_{HC}, and the thermoelectric component, I_T (Fig. 3.10a). At relatively low laser intensities, the excitation conditions are insufficient to generate the classical photocurrent through two-photon interband absorption (Fig. 3.2, process 3). Consequently, the output signal originates exclusively from the second mechanism, i.e., intraband absorption by free carriers (Fig. 3.2, process 2). Under such conditions, the temporal behaviour of the photoresponse clearly reflects the dynamics of hot carriers: the signal follows the profile of the laser pulse, and after the termination of the optical excitation, the hot carrier photocurrent vanishes. The residual “tail” of the signal is then attributed to lattice heating caused by carrier thermalization, which is expressed as the slower thermoelectric component, I_T. A different situation is demonstrated in Fig. 3.10b, where the laser intensity is sufficiently high to initiate two-photon interband absorption in addition to the intraband heating process. In this regime, the photoresponse consists of two components havingopposite polarities. The coexistence of negative and positive components evidences the simultaneous action of both mechanisms (Fig. 3.2, processes 2 and 3) in the

formation of the output signal. Specifically, the negative part of the response remains a result of the combined influence of hot carrier and thermoelectric contributions (I_{HC} + I_T), while the positive part corresponds to the classical photocurrent, I_{Gen}, induced by the generation of electron-hole pairs.

The current-voltage characteristics presented in Fig. 3.11 demonstrate that is the increase of the excitation level isfavorable for the rise of both components.

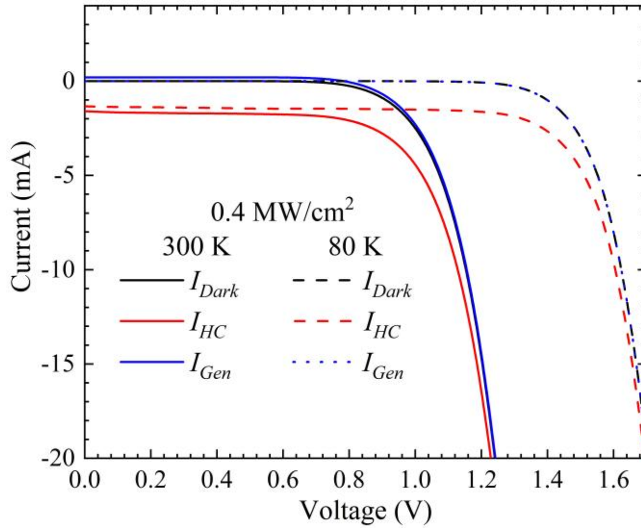

Fig. 3.11. I-Vs of GaAs p-n junction exposed to 1.064 µm laser radiation of 0.4 MW/cm^2 (solid lines) and 0.7 MW/cm^2 (dashed lines) intensity at room temperature (Gradauskas et al., 2024).

The experimental data indicate that a increase in 1.064 µm laser power further enhances the contribution of the hot carrier component. Higher optical excitation intensity supplies a larger number of carriers with excess energy, while the forward bias ensures their efficient extraction across the junction. Thus, the combined effect of elevated laser power and stronger forward bias creates optimal conditions for the manifestation of hot carrier photocurrent. Note, the generation-related component is more sensitive to laser intensity increase because of its two-photon absorption nature.

The dependence photoresponse components on laser power of 1.064 µm is shown in Fig. 3.12. The hot carrier current I_{HC} demonstrates a linear dependence on laser intensity, which is a typical signature of free-carrier heating processes: the number of hot carriers scales proportionally with the absorbed power. Conversely, the generation-induced current I_{Gen} shows a

quadratic dependence on excitation intensity, indicating that two-photon interband absorption is the dominant mechanism responsible for carrier generation under these conditions.

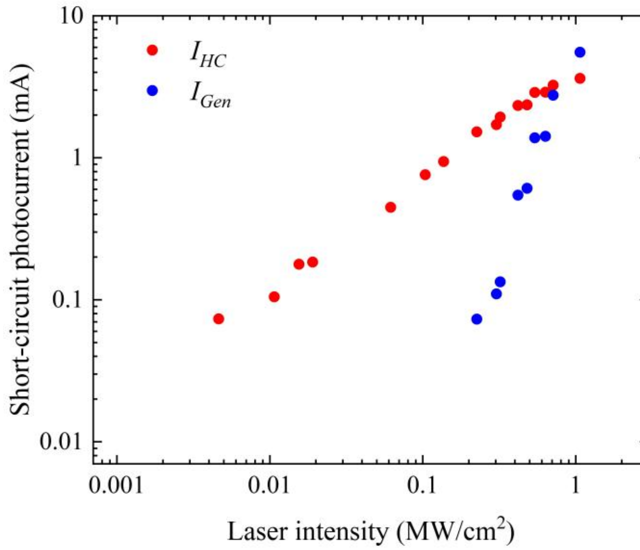

Fig. 3.12. Dependence of hot carrier (red circles) and generation-induced (blue circles) short-circuit photocurrents across GaAs p-n junction on the laser intensity at 1.064 µm at room temperature (Gradauskas et al., 2024).

As the laser intensity increases, both components become more pronounced, but the linear growth of I_{HC} is accompanied by a much steeper rise in I_{Gen}. This leads to competition between the two photocurrent components. At relatively low excitation levels, the hot carrier contribution dominates the photoresponse, while at higher intensities the generation-induced current rapidly surpasses it, eventually becoming the prevailing mechanism.

In contrast to the excitation at a wavelength of 1.064 µm, the mechanism of photocurrent formation differs under laser illumination with a wavelength of 0.532 µm, as described in the previous section (Fig. 3.2, process 4). The obtained results for this case are demonstrated in Fig. 3.13.

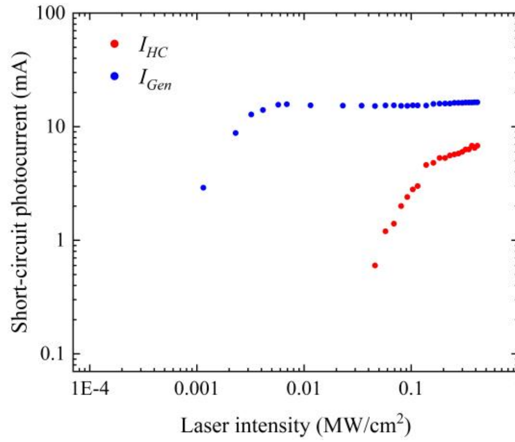

Fig. 3.13. Intensity dependence of hot carrier (red circles) and generation-induced (blue circles) short-circuit photocurrents across GaAs p-n junction under 0.532 μm illumination at room temperature.

On the other hand, the hot carrier current I_{HC} emerges more gradually and becomes visible primarily when the classical component reaches saturation. Its presence indicates that part of the absorbed photon energy exceeding the band gap is transferred to carrier heating. These hot carriers, before thermalization, are capable of overcoming the potential barrier and contributing to the HC photoresponse.

Experiments under 1.342 μm illumination were also conducted, and their results are depicted in Fig. 3.14.

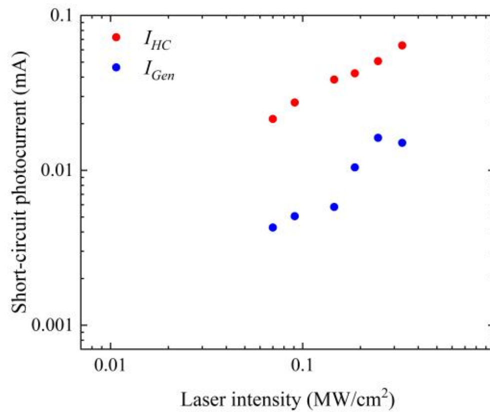

Fig. 3.14. Laser intensity dependence of hot carrier (red circles) and generation-induced (blue circles) short-circuit photocurrents across GaAs p-n junction measured under 1.342 μm excitation at room temperature.

The resulting hot carrier photocurrent again exhibits a nearly linear dependence on the laser intensity. In addition, a photocurrent of opposite polarity is observed. This component can be attributed to the photocapacitive effect associated with hot carriers. Its appearance reflects the redistribution of laser-heated carriers close to the potential barrier, leading to a displacement current that flows in the opposite direction relative to the classical generation-induced photocurrent (Ašmontas et al., 1997).

For silicon samples, a pronounced dependence of the photoresponse on the laser power was also observed. This behavior indicates the universality of hot carrier phenomena not only in direct-bandgap materials such as GaAs, but also in indirect-bandgap semiconductors, including industrial silicon solar cell structures. Fig. 3.15 presents the obtained results, which reflect how the photocurrent in industrial silicon p-n junctions depends on laser light intensity. In the inset are represented the short-circuit photocurrent pulse and laser pulse.

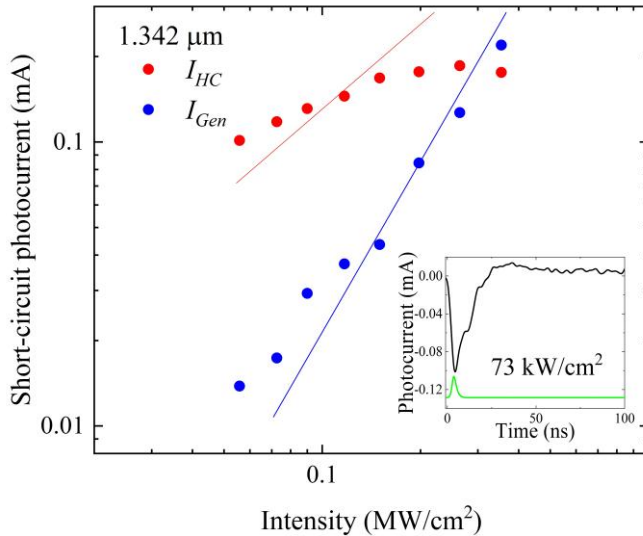

Fig. 3.15. Dependence of the short-circuit photocurrents I_{HC} and I_{Gen} on laser light intensity under illumination at 1.342 μm in industrial silicon structures at room temperature. Straight lines are guides for the eye of the respective linear and square laws. In the inset: short-circuit photocurrent pulse and laser pulse below (not to scale) (Zharchenko et al., 2024).

In the case of Si, the generation-induced photocurrent shows an almost quadratic dependence on excitation intensity, which is typical for two-photon absorption (Gradauskas et al., 2020; Bristow et al., 2007). This behavior is

explained by the fact that, under these conditions, interband transitions occur through multiphoton processes shown in Fig. 3.2, process 3. If the hot carrier photocurrent in silicon were governed solely by the intraband absorption, its dependence on intensity would be linear, as observed earlier for photons with energies much smaller than E_g (Ašmontas et al., 2001). However, the obtained I_{HC} dependence is clearly sublinear. This can be explained by several factors. First, the two-photon absorption coefficient increases with excitation power, reducing the number of photons available for free-carrier absorption. Second, the residual single-photon energy available for carrier heating after two-photon generation is much smaller, $(2hv - E_g) \div 2 = 0.365$ eV, compared to the direct single-photon absorption case ($hv = 0.92$ eV). Third, the generation component suppresses the hot carrier contribution of opposite polarity, since it grows much faster with excitation intensity.

3.3. Influence of Temperature on Hot Carrier Photocurrent Formation

It is well known that the energy relaxation time of hot electrons in semiconductors is strongly temperature dependent. In GaAs, at 80 K, it is on average an order of magnitude longer than at room temperature (Dargys & Kundrotas, 1994). This implies that, at lower temperatures, hot carriers lose their excess energy much more slowly, thus remaining in an excited "hot" state for a longer period of time. Consequently, the contribution of hot carrier processes to the formation of photoresponse in semiconductor structures is expected to increase as the temperature decreases. Experimental confirmation of this phenomenon demonstrated that the amplitude of the hot carrier photoresponse at 80 K was significantly higher compared to that at 300 K in GaAs p-n junctions (Ašmontas et al., 1996). This behaviour is consistent with theoretical expectations concerning the slowed thermal relaxation of carriers in the crystal lattice at cryogenic temperatures.

At room temperature, the intensity of the 1.064 μm laser pulse is sufficient to initiate the classical photocurrent via the two-photon absorption (Fig. 3.2, process 3). Under such conditions, the hot carrier component originates from intraband absorption (Fig. 3.2, process 2), which is additionally supported by the excess energy released during interband transitions (Fig. 3.2, process 3 stepped arrows). The results presented in Fig. 3.16 indicate vanishing of generation-related photocurrent as the GaAs p-n junction cools down from 300 K to 80 K temperature.

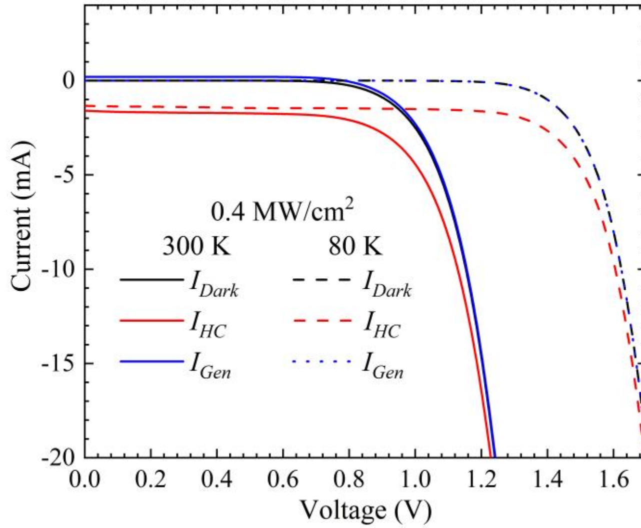

Fig. 3.16. I-V characteristics of the GaAs p-n junction exposed to 0.4 MW/cm² intense laser radiation of 1.064 µm wavelength for both room temperature (solid lines) and liquid nitrogen temperature (dashed lines) (Gradauskas et al., 2024).

This effect is attributed to the widening of the band gap, which significantly decreases the absorption coefficient (Dargys & Kundrotas, 1994) and reduces the probability of two-photon absorption. The reduction of the hot carrier photocurrent in the short-circuit mode at low temperatures can be explained by two main factors: firstly, by the lower value of the intraband absorption coefficient (Dargys & Kundrotas, 1994), and secondly, by the absence of surplus energy for carrier heating in the process of two-photon excitation. Thus, taken together, these two factors exert a stronger influence on the photocurrent than the extended relaxation time of hot carriers.

Figure 3.17 illustrates the temperature dependence of the short-circuit photocurrent components for GaAs p-n junctions under 1.064 µm laser irradiation at different intensities.

At relatively low laser intensity (0.4 MW/cm²), both the hot carrier photocurrent I_{HC} and the generation-induced photocurrent I_{Gen} exhibit a weak dependence on temperature within the range from 300 K down to 80 K.

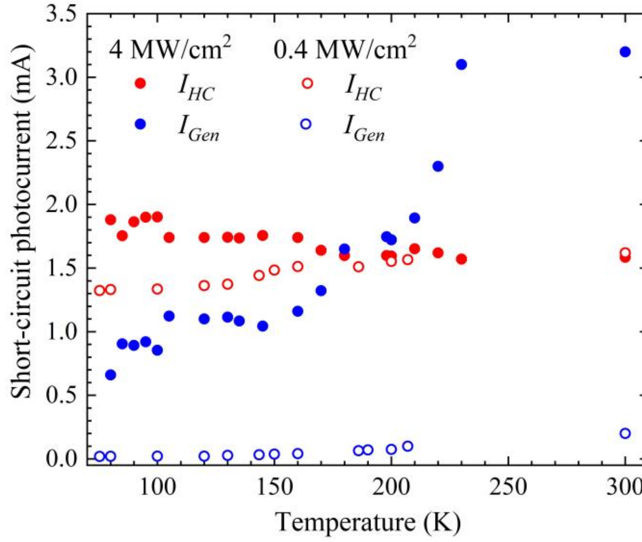

Fig. 3.17. Dependence of short-circuit photocurrents of hot carriers (red dots) and generation (blue dots) on temperature under 1.064 μm laser radiation of 0.4 MW/cm^2 (open dots) and 4 MW/cm^2 (solid dots) intensity (Gradauskas et al., 2024).

This indicates that under moderate excitation conditions the overall photocurrent is stable against thermal variations, and neither the hot carrier nor the generation process dominates significantly. However, at higher excitation intensity (4 MW/cm^2), a markedly different behavior is observed. The generation-induced current, which is relatively strong at room temperature, decreases sharply as the temperature is lowered. In contrast, the hot carrier photocurrent shows a slight but noticeable increase with decreasing temperature. This opposite trend reflects the different physical origins of the two components: the generation current is strongly influenced by two-photon interband absorption processes, while the hot carrier contribution is mainly related to intraband absorption. It is important to note that both the two-photon absorption coefficient and the free-carrier absorption coefficient decrease with lower temperatures (Krishnamurthy et al., 2011). Consequently, the persistence and even growth of the hot carrier photocurrent under such conditions suggests that it cannot be attributed solely to the intraband absorption. Instead, its magnitude results from the interplay and competition between carrier generation and carrier heating processes.

As Fig. 3.16 shows, the dark I-V curve shifts to the higher voltage values with lower temperature, reflecting an increase in potential barrier height. The same property is observed for the silicon samples (Fig. 3.18).

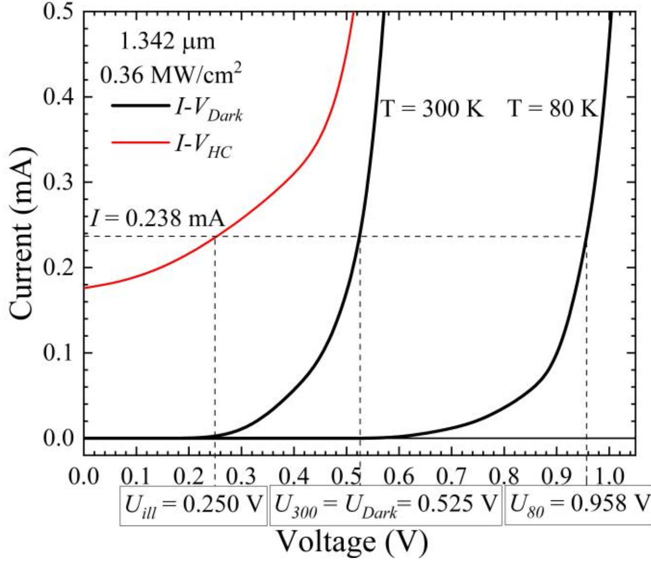

Fig. 3.18. Current-voltage characteristics of the Si solar cell in the dark at room and liquid nitrogen temperatures (black lines), and I-V of HC at room temperature (red line) (Zharchenko et al., 2024).

There exists the so called voltage temperature coefficient α_T, which characterizes the shift of the diode's I-V curve with temperature (Schaffner & Shea, 1955):

$$\alpha_T = \frac{\Delta U}{\Delta T}|I = const|. \tag{3.1}$$

In practical photovoltaic devices, α_T usually has a negative value: with increasing temperature, the voltage at a fixed current decreases, and each semiconductor material has characteristic values of this coefficient. For silicon, typical values fall within the –1.8 to –2.2 mV/K range, confirming the high sensitivity of the barrier height to temperature changes (Green & Blakers, 1982; Zhao et al., 1994; Cotfas et al., 2018). In this study, the same effect was employed as an "internal thermometer" for evaluating the hot carrier temperature under sub-bandgap laser irradiation. According to the dark I-V characteristics, at a fixed current of 0.238 mA, the voltage changes

from U_{300} = 0.525 V at T = 300 K to U_{80} = 0.958 V at T = 80 K. This corresponds to the temperature coefficient of $\alpha_T = -1.97$ mV/K, which is in good agreement with the reported value for silicon solar cells. Under laser illumination, the current also reaches 0.238 mA at room temperature (see red line in Fig. 3.18). In this case, the sole difference between the dark current and the photocurrent, which are equal in magnitude, is determined by the carrier temperature. From the corresponding voltages $U_{Dark} = U_{300}$ = 0.525 V and U_{ill} = 0.250 V (Fig. 3.18), and applying the calculated value of α_T, the temperature difference between the carriers and the lattice is obtained as:

$$\Delta T = \frac{U_{ill} - U_{Dark}}{\alpha_T} |I = 0.238\, mA| = 140\, K. \tag{3.2}$$

For the calculation, the current magnitude of 0.238 mA was selected based on the assumption that the dark current at U_{ill} = 0.250 V is sufficiently small and can be neglected. Under these conditions, the net current is defined exclusively by the HC photocurrent, which makes the evaluation of carrier temperature more reliable. The proposed model is further supported by a number of consistent arguments: as the excitation intensity increases, the photocurrent is amplified; the illuminated I-V curve (the red one in Fig. 3.18) shifts upward; U_{ill} becomes lower and the voltage difference ΔU at a fixed current becomes larger; and, accordingly, the value of the carrier temperature increases in agreement with equation (3.2). Thus, this method provides a direct way to detect the hot carrier temperature in single junction solar cells.

Comparison of the obtained hot carrier temperature with results reported by other authors cannot be straightforward because different studies use various experimental techniques and conditions. For instance, optical investigations typically depend on above-bandgap stimulation, which effectively elevates carrier temperatures. Numerical pump-probe simulations using femtosecond laser pulses of very high intensity (TW/cm^2) have produced electron temperatures in silicon over 4600 K (Sato et al., 2014). Time-resolved luminescence studies of bulk GaAs, on the other hand, have demonstrated a strong dependence of carrier temperature on excitation level and delay time, showing a decrease from 1200 K at a 1 ps delay to 300 K at a 100 ps delay (Pelouch et al., 1992). In this context, the evaluated carrier temperature in silicon is approximately 440 K when subjected to sub-bandgap laser irradiation at 1.342 μm, with a power density of 0.36 MW/cm^2 and a nanosecond pulse duration seems reasonable. Importantly, the suggested approach delivers an approximate, though consistent, assessment of the hot carrier temperature. This estimate is expected to be relatively insensitive to

the choice of the constant current value, since the dark I-V curves at T = 300 K and T = 80 K are nearly parallel, and therefore the voltage difference $U_{ill} - U_{Dark}$, as used in equation (3.2), remains almost unchanged.

3.4. Ratchet-based radiation sensor of broad radiation spectrum.

Various types of light sensors are characterized by specific limitations that determine their suitability for particular applications. Some are limited by insufficient sensitivity to weak signals, others by maximum response speed, spectral detection range, or the requirement for operation within a restricted temperature interval. Therefore, the search for alternative principles of infrared radiation detection remains a relevant task in modern semiconductor physics. One of the promising directions is the utilization of free carrier heating effects induced by infrared radiation. Previous studies have shown that in nonuniform semiconductor structures (p-n, p-i-n, l-h junctions, heterojunctions, and Schottky barriers), photovoltage can be generated due to the thermoelectromotive force of hot carriers even when the photon energy is lower than the semiconductor bandgap (Ašmontas et al., 2003). In this case, intraband absorption dominates, and the photoresponse is determined by the emission of hot carriers across the potential barrier. It has also been demonstrated that such structures are capable of producing a response signal at room temperature and provide nanosecond response times, which fundamentally distinguishes them from conventional narrow bandgap photodetectors. At the same time, in conventional p-n and heterostructures, the formation of the photoresponse is strongly associated with the potential barrier height and structural symmetry. In the absence of spatial asymmetry, the motion of heated carriers remains statistically symmetric, and the efficiency of converting their chaotic energy into a useful electrical signal is limited.

Electronic ratchet-type devices offer a fundamentally different approach. Unlike classical sensors, electronic ratchets are based on the creation of a periodic, asymmetric electric potential, which can give the random motion of charge carriers a directional character (Lau & Kedem, 2020). In such structures, a spatially asymmetric potential converts the chaotic motion of carriers, including hot carriers, into directed transport without the need for an external bias. In this way, such structures are able to rectify chaotic oscillating signals, for example, thermal noise, generating a unidirectional voltage or current (Roeling et al., 2011). The combination of carrier heating mechanisms with controlled potential asymmetry opens the possibility of developing highly sensitive infrared sensors capable of operating at room temperature

without the need for cryogenic cooling. Depending on the implementation, "flashing" and "rocking" ratchets are distinguished (Kedem et al., 2017; Linke et al., 1999). Despite its theoretical appeal, the practical implementation of ratchet structures is technologically challenging. Their fabrication often requires advanced nanolithography, quantum-confined heterostructures, and sometimes low temperatures. Organic semiconductor ratchets can operate at room temperature but suffer from low carrier mobility and density, while GaAs/AlGaAs ratchets demand nanowires and nanoscale Schottky gates, making the technology complex (Tanaka et al., 2013). A theoretical model of a ratchet sensor based on $Si/Si_{1-x}Ge_x$was proposed, where the asymmetric potential was created by mechanical elastic deformation gradients (Lau et al., 2017). Although this approach allowed the photovoltaic effect to be realized under far-infrared illumination, it had several significant disadvantages: complexity of controlling composition and growth of layers, limited active layer thickness (~100 nm), high internal resistance, and sensitivity to surface defects. The scientific and practical need is to create a ratchet radiation sensor capable of operating at room temperature, without complex technological limitations, and with an extended spectral sensitivity range.

The proposed concept of the $Al_xGa_{1-x}As$ ratchet sensor (see Section 2.1) overcomes the limitations of the existing analogues, such as the limited thickness of the active region and the technological complexity of forming a periodic potential in $Si/Si_{1-x}Ge_x$ structures. It is notable that the potential barrier height can be adjusted within the range of 100 – 500 meV (x = from 0.3 to 0, respectively), allowing the sensor to be tailored to specific spectral sensitivity requirements. The distance over which the conduction band edge decreases within the graded layer (the period) is chosen to be longer than the electron diffusion length, ensuring effective carrier drift transport. The electron concentration in the active region is selected to provide an optimal compromise between high sensitivity and low noise. The ratchet sensor operates on the basis of the hot carrier effect, schematically illustrated in Fig. 3.19.

In the absence of irradiation, free electrons are concentrated in the potential wells of the periodic asymmetric potential (Fig. 3.19a). Under illumination, the average electron energy increases, they become the hot carriers that diffuse in both opposite directions along the x-axis (Fig. 3.19b).

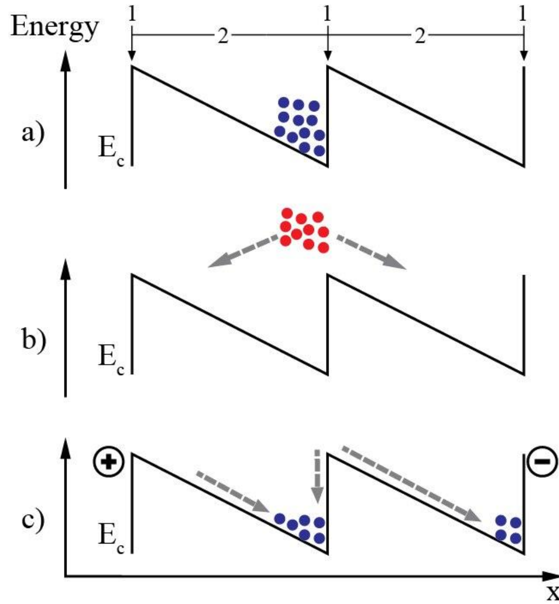

Fig. 3.19. Periodic potential of the ratchet sensor and schematic distribution of electrons in the conduction band: (a) absence of irradiation; (b) heating of free electrons and diffusion of hot electrons in both directions; (c) electron relaxation and redistribution between potential wells. E_c denotes the conduction band edge, and the plus and minus signs in circles indicate the polarity of the induced electromotive force.

As the hot electrons lose their excess energy, they relax to the bottom of the conduction band and drift under the influence of the potential gradient toward adjacent potential wells (Fig. 3.19c). Some carriers cross the barrier and enter the neighboring well, while the others return to the initial one. As a result, an electromotive force is induced at the sensor terminals, and in a closed electrical circuit, a direct current flows.

During the experimental investigation, the fabricated ratchet-based sensor based on $Al_{0.3}Ga_{0.7}As$ was exposed to laser radiation of different wavelengths to analyze its spectral response features. Figure 3.20a presents representative oscillograms recorded under illumination with a laser of 0.532 µm wavelength corresponding to 2.34 eV photon energy . This energy significantly exceeds the GaAs band gap (E_g = 1.42 eV), thus ensuring efficient interband absorption. Also, the sensor was also illuminated with pulsed laser radiation of 1.064 µm wavelength, corresponding to photon energy of 1.16 eV (Figure 3.20b). In this case, free carrier heating occurs mainly due to the intraband absorption.

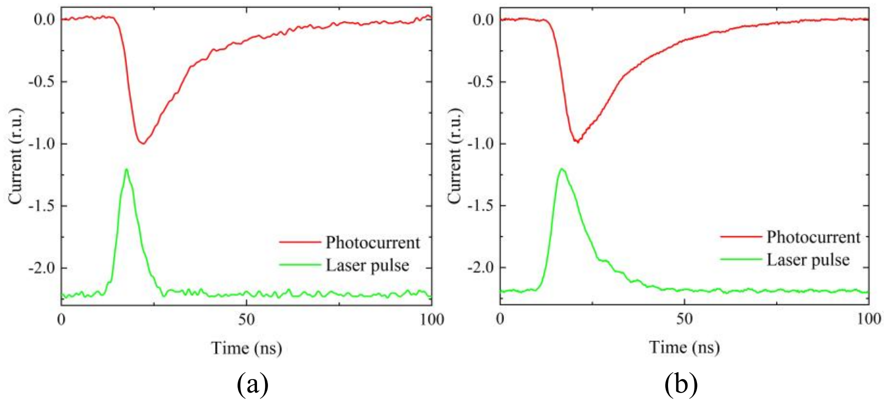

Fig. 3.20. Normalized to unity typical photocurrent signals (red) measured at room temperature under irradiation with intensities of 0.3 MW/cm^2 for 0.532 μm (a) and 7.4 MW/cm^2 for 1.064 μm (b) laser pulses (green). Laser pulses are not to scale.

The rapid rise of the recorded pulse and the polarity of the signal are consistent with the "+" and "–" designations shown in Fig. 3.19. A comparison of the oscillograms obtained under both excitation conditions reveals that the developed sensor is capable of responding not only to photons with energies exceeding the GaAs bandgap but also to photons with energies below it. This observation provides clear evidence that the sensor operates on the basis of the hot carrier effect. Furthermore, the ability to detect both above- and below-bandgap radiation demonstrates its broadband sensitivity, which significantly separates the proposed device from conventional quantum photodetectors limited to the interband absorption processes.

For a more comprehensive comparison of detection efficiency in different spectral regions, the photocurrent was analyzed as a function of incident laser intensity at wavelengths 0.532 μm (Fig. 3.21a), 1.064 μm (Fig. 3.21b), and 2.0 μm (Fig. 3.21c). The wavelengths were chosen to compare the sensor's ability to detect photons with energies significantly higher than the GaAs band gap ($h\nu$ = 2.34 eV), close to the band gap ($h\nu$ = 1.16 eV), and substantially lower ($h\nu$ = 0.62 eV). This approach makes it possible to evaluate the contributions of interband absorption, intraband carrier heating, and the manifestation of the hot carrier effect in the formation of the photocurrent.

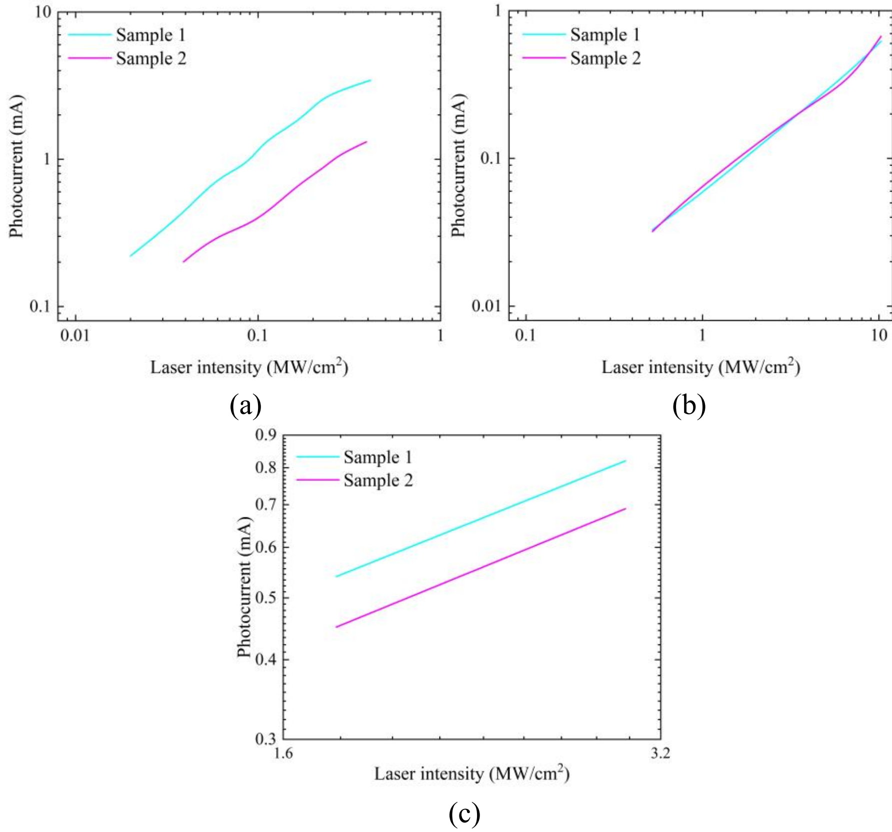

Fig. 3.21. Dependence of the photocurrent across the typical two ratchet-based sensors on 0.532 µm (a), 1.064 µm (b) and 2 µm (c) lasers intensity at room temperature.

When illuminated with $\lambda = 0.532$ µm, efficient interband absorption takes place in the structure. The photocurrent shows an linear dependence on the incident laser power. As Fig. 3.21b and Fig. 3.21c shows, both samples exhibit a linear dependence of photocurrent on 1.064 µm and 2.0 µm laser power throughout the entire investigated range. This indicates that the signal formation mechanism is not governed by interband (two-photon) absorption but rather by intraband carrier heating and the subsequent dynamics of hot carriers. The linear behavior confirms that with increasing irradiation intensity, the average carrier energy rises proportionally, leading to a stable photocurrent increase without signs of saturation within the investigated power range.

The results above demonstrate the potential of the ratchet-based sensor for broadband photodetection ranging from visible to the infrared spectra. Figure

3.22 presents the temporal oscillograms of the electromotive force induced across the sensor under laser pulse excitation of 0.532 μm and 2.0 μm wavelengths.

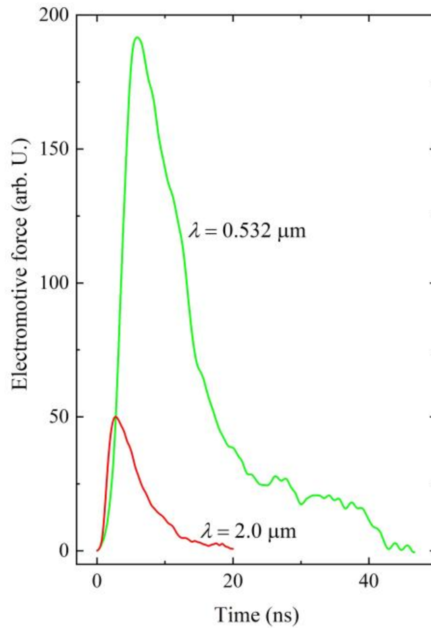

Fig. 3.22. Induced electromotive force signals under exposure to 2.0 μm laser irradiation of 3 MW/cm^2 intensity and 0.532 μm laser irradiation of 0.2 MW/cm^2 intensity. Pulse magnitudes are not normalized.

In the case of short-wavelength excitation, the signal amplitude is clearly four times higher than under the long-wavelength irradiation. This difference is directly related to the strong spectral variation of the absorption coefficient in gallium arsenide. The absorption coefficient of GaAs at λ = 0.532 μm is approximately 3000 times greater than that at λ = 2.0 μm (see Fig. 3.23). As a result, at shorter wavelengths, the interband absorption takes place much more efficiently, which leads to a higher photoresponse amplitude. In contrast, under irradiation at λ = 2.0 μm, the photon energy is lower than the GaAs band gap, and the signal is formed mainly through much weaker intraband processes.

Figure 3.23 shows spectral dependence of the experimentally obtained responsivity values of the developed ratchet-based sensor alongside with the absorption coefficient of GaAs.

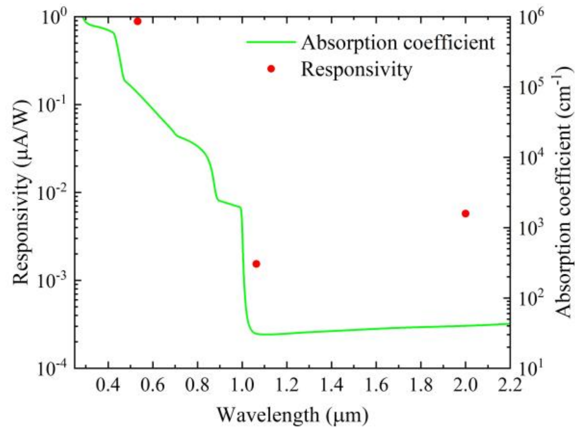

Fig. 3.23. Spectral dependences of the responsivity values (red dots) of the developed ratchet-based sensor and absorption coefficient of gallium arsenide (green line, taken from (Dargys & Kundrotas, 1994; Adachi, 1989; Green, 2008)).

It is seen, that the responsivity of the developed ratchet-based sensor follows the general trend of the GaAs absorption coefficient across the investigated spectral range.

As part of the investigation, the influence of temperature on the characteristics of the developed sensor was also analyzed. Figure 3.24 presents the photocurrent dependence on laser intensity at two temperature regimes: room temperature (T = 300 K) and liquid nitrogen temperature (T = 80 K).

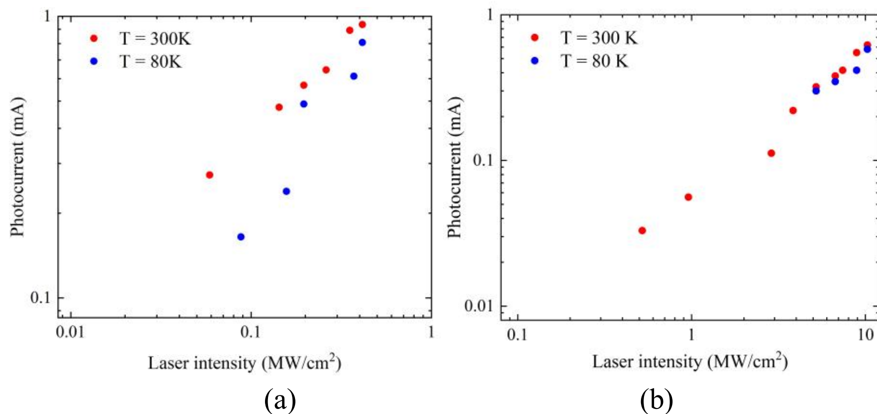

Fig. 3.24. Dependence of photocurrent on laser intensity at room temperature (red dots) and liquid nitrogen temperature (blue dots): (a) under 0.532 μm irradiation; (b) under 1.064 μm irradiation.

Across the entire investigated range of 0.532 μm irradiation intensities (Fig. 3.24a), the photocurrent is higher at room temperature than at liquid nitrogen temperature. This difference can be explained by the fact that the interband absorption coefficient in GaAs is higher at room temperature (Dargis & Kundrotas, 1994), and widening of the bandgap with lower temperature leaves less energy for heating of the generated carriers.

In contrast, in the case of 1.064 μm laser irradiation (as Figure 3.24b shows), the temperature-dependent deviation between the curves is minimal. This behavior can be attributed to the fact that the photoresponse is formed exclusively via the intraband absorption which is independent of the semiconductor bandgap, while the two-photon absorption is supressed by the bandgap widening with lower temperature.

CONCLUSIONS

1. The formation of hot carrier photocurrent in GaAs and Si p-n junctions is governed by excitation wavelength. Sub-bandgap irradiation promotes free carrier heating and a pronounced hot carrier contribution, whereas shorter wavelengths favor generation-related photocurrent, with partial energy transfer to carrier heating.
2. The photocurrent is strongly excitation-dependent and follows distinct scaling laws. Under sub-bandgap irradiation, the hot-carrier contribution is nearly linear at low intensities, while at higher levels a generation-induced term appears with a quadratic dependence characteristic of two-photon interband absorption. Under above-bandgap excitation, the generation photocurrent dominates, and the hot carrier component becomes apparent only once this contribution saturates.
3. Carrier heating and the competition between hot carrier and generation currents are universal across both direct- and indirect-bandgap semiconductors, as demonstrated in GaAs and Si – including industrial solar cells – highlighting their fundamental role in photovoltaic conversion.
4. The applied bias voltage is a key parameter controlling the realization of hot carrier photocurrent. When the potential barrier is sufficiently reduced, hot carriers can effectively cross the junction, resulting in a sharp increase of the hot carrier contribution.
5. Temperature has a non-trivial influence on the interaction between hot carrier and generation-induced photocurrent components. Cooling simultaneously enhances carrier heating effects through increased energy relaxation time and suppresses both intraband and interband absorption processes. The resulting dominance of either mechanism depends on excitation intensity, with hot carrier contribution prevailing at low intensities and becoming more pronounced at reduced temperatures.
6. The voltage-temperature coefficient methodology enables quantitative evaluation of hot carrier temperature in p-n junctions. Analysis of I-V shifts under sub-bandgap illumination demonstrates that carrier temperature can be directly extracted from electrical characteristics, providing a diagnostic tool for nonequilibrium carrier dynamics consistent with literature data.
7. The developed ratchet-based sensor operates under both above- and sub-bandgap excitation. Its photoresponse arises from hot carrier

heating induced by both classical interband and intraband absorption mechanisms, ensuring broadband spectral sensitivity beyond the limits of conventional interband photodetectors.

8. Temperature studies show that sensor sensitivity increases with temperature under interband excitation, while remaining nearly temperature independent under intraband excitation. This confirms stable room temperature operation and highlights a key advantage over conventional infrared sensors requiring cryogenic cooling.

SANTRAUKA

Per pastaruosius dešimtmečius saulės elementų (SE) efektyvumo didinimo tyrimai išlieka viena svarbiausių šiuolaikinės fotovoltikos ir energetikos mokslo krypčių. Klasikinis vienos p-n sandūros saulės elementas, nepaisant gamybos technologijų pažangos, iki šiol nepasiekė teorinės Shockley–Queisser ribos, siekiančios apie 33 % (Shockley & Queisser, 1961). Pagrindinė mažo efektyvumo priežastis yra fundamentalūs vidiniai nuostoliai, sąlygojami fotonų sąveikos su puslaidininkine medžiaga (Hirst & Ekins-Daukes, 2011). Svarbiausi jų yra spektriniai nuostoliai, atsirandantys dėl to, kad fotonai, kurių energija yra mažesnė už draudžiamosios energijos tarpą (E_g), nėra sugeriami, bei vadinamieji termalizacijos nuostoliai, susiję su perteklinės fotonų energijos (kai jų energija viršija E_g) išsklaidymu kristalinei gardelei šilumos pavidalu karštųjų krūvininkų relaksacijos metu. Kartu šie du mechanizmai sudaro iki 80 % visų vidinių nuostolių saulės elementuose (Hirst & Ekins-Daukes, 2011). Praktikoje pasiekti maždaug 26 % silicio ir 28 % galio arsenido saulės elementų efektyvumai vis dar išlieka mažesni už teorinę ribą.

Trečiosios kartos fotovoltikos vystymas yra orientuotas į šių apribojimų įveikimą, pasitelkiant daugiasandūrines struktūras, spektrinę konversiją, kvantinius šulinius ir kvantinius taškus, taip pat karštųjų krūvininkų saulės elementų koncepciją; pastarųjų efektyvumas, esant selektyviam krūvininkų ištraukimui dar prieš jų termalizaciją, teoriškai gali pasiekti iki 66 % (Ross & Nozik, 1982). Tačiau praktinis tokių įtaisų realizavimas susiduria su rimtais technologiniais iššūkiais, susijusiais su itin trumpa karštųjų krūvininkų gyvavimo trukme, siekiančia pikosekundžių eilę. Žvelgiant iš kitos perspektyvos, karštieji krūvininkai gali indukuoti fotovoltinę įtampą, kurios poliškumas yra priešingas elektrono-skylės generacijos sąlygotai fotoįtampai, taip mažindami bendrą p-n sandūros saulės elemento efektyvumą (Masalskyi & Gradauskas, 2022).

Taigi, karštųjų krūvininkų reiškinys pasireiškia dvejopu vaidmeniu. Viena vertus, jis gali būti traktuojamas kaip papildomas vidinių nuostolių mechanizmas klasikiniuose saulės elementuose, keliantis klausimų dėl teorinės efektyvumo ribos pasiekiamumo. Kita vertus, jis atveria perspektyvas kurti naujas, itin efektyvias fotovoltines struktūras ir jutiklinius įtaisus, kuriuose karštųjų krūvininkų vyksmai gali būti sąmoningai ir kontroliuojamai panaudojami.

Tikslas

Tyrimo tikslas yra ištirti karštųjų krūvininkų vaidmenį vienos sandūros saulės elementuose, ypatingą dėmesį skiriant jų tiesioginei įtakai fotovoltiniam atsakui.

Tyrimu siekiama įvertinti temperatūrines ir spektrines sąlygas, kuriomis karštųjų krūvininkų indėlis tampa dominuojantis. Taipogi, papildomas dėmesys yra skiriamas tikslingam karštųjų krūvininkų reiškinio panaudojimui kuriant naujas puslaidininkines struktūras – reketinius elektromagnetinės spinduliuotės jutiklius, – veikiančius karštųjų krūvininkų pagrindu.

Tyrimo uždaviniai

Siekiant tyrimo tikslo, buvo suformuluoti šie uždaviniai:

1. Ištirti GaAs ir Si p-n sandūrų voltamperines charakteristikas, esant lazeriniam sužadinimui skirtingų bangos ilgių ir intensyvumų spinduliuote, bei išanalizuoti generacijos ir karštųjų krūvininkų fotosrovių tarpusavio sąveiką.

2. Nustatyti temperatūrines ir spektrines sąlygas, kuriomis karštųjų krūvininkų indėlis tampa reikšmingas arba dominuojantis bendrame fotovoltiniame atsake.

3. Įvertinti efektyviąją karštųjų krūvininkų temperatūrą, remiantis volatamperinių charakteristikų analize.

4. Sukurti, sumodeliuoti ir eksperimentiškai ištirti GaAs/$Al_xGa_{1-x}As$ reketinį elektromagnetinės spinduliuotės jutiklį, veikiantį karštųjų krūvininkų reiškinio pagrindu.

Mokslinis naujumas

Pirmą kartą eksperimentiškai parodytas tiesioginis karštųjų krūvininkų poveikis vienos sandūros saulės elementų, ypač GaAs ir Si p-n sandūrų, fotovoltiniam atsakui plačiame spinduliuotės bangos ilgių ir temperatūrų diapazone. Efektyvioji karštųjų krūvininkų temperatūra nustatyta remiantis voltamperinių charakteristikų ir jų temperatūrinės priklausomybės analize, dėmesį skiriant pramoniniams silicio saulės elementams. Be to, sukurtas ir eksperimentiškai ištirtas GaAs/$Al_xGa_{1-x}As$ reketinis jutiklis, veikiantis karštųjų krūvininkų reiškinio pagrindu. Tyrimai atskleidė šio jutiklio veikimo

galimybes plačiame spektriniame ir temperatūriniame diapazone, tokiu būdu pasiūlant naują elektromagnetinės spinduliuotės detekcijos koncepciją.

Tyrimo rezultatų praktinė vertė

1. Gauti rezultatai leidžia patikslinti fotovoltinio atsako formavimosi mechanizmus vienos sandūros saulės elementuose ir gali būti taikomi peržiūrint bei tikslinant klasikinių struktūrų efektyvumo ribas.
2. Efektyviosios karštųjų krūvininkų temperatūros nustatymas pramoniniuose silicio saulės elementuose sudaro prielaidas tiksliau prognozuoti jų veikimo charakteristikas esant skirtingoms eksploatavimo sąlygoms, ypač koncentruotos spinduliuotės sistemose.
3. Sukurtas ir eksperimentiškai ištirtas GaAs/$Al_xGa_{1-x}As$ reketinis jutiklis parodo praktinį karštųjų krūvininkų reiškinio panaudojimo potencialą elektromagnetinės spinduliuotės, ypač infraraudonosios srities, detekcijos įrenginiuose, nereikalaujant kriogeninio aušinimo.

Ginamieji teiginiai

1. Karštųjų krūvininkų fotosrovė egzistuoja saulės elementuose su p-n sandūra nepriklausomai nuo šviesos fotonų energijos; ji susidaro tiek dėl laisvakrūvės, tiek dėl tarpjuostinės šviesos sugerties.
2. Karštųjų krūvininkų sukelta fotosrovė tampa reikšminga įtampų srityje ties maksimalios galios tašku, kas parodo esminį karštųjų krūvininkų vyksmų neigiamą indėlį į saulės elemento veikimą.
3. Efektyvioji karštųjų krūvininkų temperatūra gali būti kiekybiškai nustatyta taikant įtampos-temperatūros koeficiento metodą, kuris suteikia tiesioginį eksperimentinį būdą tirti krūvininkų kaitimo dinamiką fotovoltiniuose įrenginiuose.
4. GaAs/$Al_xGa_{1-x}As$ reketo tipo jutiklis veikia plačiame spektriniame ruože, detektuodamas fotonus, kurių energija yra tiek mažesnė, tiek ir didesnė už draudžiamosios energijos tarpą, o jo sėkmingam veikimui infraraudonųjų spindulių srityje nereikia kriogeninio aušinimo.

Autoriaus indėlis

Autorius savarankiškai atliko pagrindinę GaAs ir Si p-n sandūrų eksperimentinių tyrimų dalį, taikant lazerinį žadinimą skirtingų bangos ilgių, intensyvumų ir temperatūrų sąlygomis. Autorius vykdė surinktų duomenų

analizę ir vizualizavimą, generacijos nulemtos ir karštųjų krūvininkų fotosrovės dedamųjų atskyrimą, taip pat efektyviosios karštųjų krūvininkų temperatūros įvertinimą pramoniniuose silicio saulės elementuose. $GaAs/Al_xGa_{1-x}As$ reketinio jutiklio koncepcija ir konstrukcija buvo sukurta tiesiogiai dalyvaujant autoriui, kuris taip pat atliko jo eksperimentinius tyrimus ir gautų rezultatų interpretaciją. Autorius parengė susijusių mokslinių publikacijų rankraščius ir pristatė tyrimų rezultatus tarptautinėse bei nacionalinėse mokslinėse konferencijose.

Literatūros apžvalga

Elektros energijos gamyba saulės elementais yra vienas perspektyviausių sprendimų tvariam pasaulinių energijos poreikių tenkinimui. Saulės elementai, veikdami fotovoltinio reiškinio principu, konvertuoja saulės spinduliuotę į elektros energiją taip mažindami šiltnamio efektą sukeliančių dujų emisijas ir naudodami gausų atsinaujinančios energijos šaltinį. Per pastaruosius du dešimtmečius reikšmingas fotovoltinių modulių kainų sumažėjimas paskatino spartų šių technologinį vystymąsi (Green, 2000; Razykov et al., 2011; Green, 2019). Fotovoltinės saulės elementų technologijos dažniausiai yra skirstomos į tris kartas (Green, 2006). Pirmosios kartos saulės elementai, gaminami iš tradicinių puslaidininkinių medžiagų, silicio ir III–V grupės junginių, veikia klasikinės p-n sandūros principu. Fotonai, kurių energija viršija draudžiamosios energijos tarpą, generuoja elektronų-skylučių poras, kurios atskiriamos vidinio elektrinio lauko, taip sukuriant fotosrovę (Shockley & Queisser, 1961; Green, 2006; Rühle, 2016). Tokių vienos sandūros elementų efektyvumas yra mažesnis už teorinę Shockley–Queisser vertę (~33 %), o dar platesnį jų panaudojimą riboja aukšti medžiagų grynumo reikalavimai ir sudėtingi gamybos procesai. Vis dėlto, dėl savo patikimumo ir brandžių gamybos metodų, jie išlieka dominuojančia fotovoltine technologija pasaulyje (Green, 2000). Antrosios kartos saulės elementai atsirado kaip plonasluoksnės technologijos XX a. aštuntojo dešimtmečio pabaigoje, siūlančios mažesnį medžiagų sunaudojimą ir mažesnes gamybos sąnaudas (Green, 2006). Nors jų efektyvumas paprastai yra mažesnis nei kristalinio silicio pirmosios kartos elementų, plonasluoksniai saulės elementai pasižymi tokiais privalumais kaip lankstumas, mažas svoris ir tinkamumas pastatuose integruotoms bei nešiojamoms taikomosios paskirties sistemoms. Trečiosios kartos fotovoltinės technologijos siekia viršyti vienos sandūros elemento efektyvumo ribą ir pasiekti didesnį nei 60 % efektyvumą, taikant pažangias koncepcijas, tokias kaip daugiasandūrinės architektūros, nanostruktūriniai dariniai, spektrinė konversija ir nauji

krūvininkų valdymo mechanizmai, įskaitant daugybinį eksitonų generavimą, karštųjų krūvininkų ekstrakciją ir tarpinės juostos fotovoltiką. Šie metodai skirti išplėsti efektyvų saulės spektro panaudojimą ir sumažinti šiluminės relaksacijos nuostolius.

Didžiausias teorinis fotovoltinės energijos konversijos efektyvumas vienos sandūros saulės elementuose apibrėžiamas Shockley–Queisser riba (Shockley–Queisser limit, SQL). Anot šio modelio, fotonai, kurių energija yra mažesnė už puslaidininkio draudžiamosios energijos tarpą, išvis nėra sugeriami, o fotonai, kurių energija viršija E_g, generuoja elektronų-skylučių poras su 100 % kvantiniu efektyvumu (Shockley & Queisser, 1961). Paverčiant šviesos energiją elektra, saulės elementuose yra patiriami reikšmingi energijos nuostoliai. Šie nuostoliai paprastai skirstomi į vidinius (intrinsic), kylančius dėl fundamentalių vienos sandūros įtaisų apribojimų, ir išorinius (technologinius), kuriuos lemia medžiagų netobulumai, įrenginio konstrukcija, optiniai nuostoliai bei elektriniai nuostoliai, susiję su varžiniais efektais (Hirst & Ekins-Daukes, 2011). Didžiąją vidinių nuostolių dalį sudaro spektriniai nuostoliai, susiję su mažos energijos fotonų pralaidumu (nesugerimu) bei krūvininkų termalizacija; jiems priskiriami ir rekombinaciniai nuostoliai dėl spindulinės, Shockley–Read–Hall ir Auger rekombinacijos, taip pat entropiniai arba termodinaminiais nuostoliai, susiję su spinduliavimu ir ribota saulės spinduliuotės koncentracija. Spektriniai nuostoliai sudaro iki 80 % visų energijos nuostolių vienos sandūros saulės elementuose (Hirst & Ekins-Daukes, 2011), todėl jų mažinimas yra vienas pagrindinių tyrimų tikslų. Svarbu pabrėžti, kad šie nuostoliai yra tiesiogiai ar netiesiogiai susiję su karštųjų krūvininkų generavimu saulės elementuose.

Nors gamybos technologijų, medžiagų kokybės ir įrenginių architektūros pažanga leidžia sumažinti rekombinacinius, optinius ir varžinius nuostolius, šiuolaikinė fotovoltika vis dažniau peržengia klasikinės vienos sandūros paradigmos ribas. Siekiant įveikti fundamentalius Shockley–Queisser efektyvumo apribojimus, yra kuriamos novatoriškos koncepcijos. Viena svarbiausių iš jų – daugiasandūriai saulės elementai (MJSC) siūlantys sumažinti spektrinius nuostolius. Užuot naudoję vieną absorberį, MJSC taiko kelių sandūrų kaskadą iš skirtingų draudžiamosios energijos tarpo puslaidininkių, kurių kiekvienas yra optimizuotas tam tikram saulės spektro ruožui. Toks metodas leidžia pasiekti gerokai didesnius efektyvumus, teoriškai viršijančius 45 % esant koncentruotai apšvietai (Henry, 1980; Martí & Araujo, 1996; Baiju & Yarema, 2022). Tipinėje MJSC architektūroje didelės energijos fotonai sugeriami plačios draustinės juostos viršutinėje sandūroje, o mažesnės energijos fotonai pasiekia tolesnes, mažesnio draudžiamosios energijos tarpo sandūras, taip sumažinant tiek termalizacijos,

tiek mažos energijos fotonų nuostolius (Baiju & Yarema, 2022; Polman et al., 2016). Vis dėlto praktinį tokių įrenginių pritaikymą riboja tokie iššūkiai kaip optimalaus draudžiamosios energijos tarpo parinkimas, gardelės suderinamumas, tunelinių sandūrų varža, optiniai nuostoliai ir didelės III–V medžiagų auginimo sąnaudos (Yamaguchi et al., 2008).

Kitas novatoriškas požiūris yra pagrįstas kvantiškai struktūrizuotais dariniais, naudojančiais kvantinį apribojimą draudžiamosios energijos tarpui, sugerties spektrui ir krūvininkų rekombinacijos keliams valdyti. Nors tokios medžiagos siūlo perspektyvias galimybes didinti efektyvumą, jų plataus masto taikymą riboja rekombinaciniai nuostoliai, ilgalaikio stabilumo problemos, toksiškumo klausimai ir sudėtingi gamybos procesai.

Spektrinės manipuliacijos metodai siekia sumažinti neatitikimą tarp saulės spektro ir fotovoltinių įtaisų sugerties charakteristikų, paverčiant kitais atvejais nepanaudotą fotonų energiją elektriškai naudinga forma (Trupke et al., 2002; Richards, 2006; Van Sark et al., 2005). Šiems metodams priskiriama konversija aukštyn (up-conversion), kai keli mažos energijos fotonai yra sujungiami į vieną didelės energijos fotoną, ir konversija žemyn (down-conversion), kai vienas didelės energijos fotonas suskaidomas į du mažesnės energijos fotonus galinčius generuoti krūvininkus. Daugybinė eksitonų generacija, arba krūvininkų dauginimas, yra alternatyvus mechanizmas, kai vienas didelės energijos fotonas tiesiogiai puslaidininkyje sukuria kelias elektronų-skylučių poras, panaudodamas perteklinę karštųjų krūvininkų energiją, kuri kitu atveju būtų prarasta termalizacijos būdu. Nepaisant koncepcinių privalumų, šias fotonų ir krūvininkų valdymo strategijas šiuo metu riboja mažas kvantinis efektyvumas, greitas krūvininkų atvėsimas ir parazitiniai rekombinacijos procesai.

Karštųjų krūvininkų reiškiniai gali būti laikomi tiesiogine strategija termalizacijos nuostoliams įveikti (Ross & Nozik, 1982). Pusiausvyros sąlygomis krūvininkai puslaidininkiuose paklūsta Fermi–Dirako skirstiniui, apibrėžtam gardelės temperatūra T_0. Šviesos sugertis, stiprių elektrinių ar mikrobanginių laukų poveikis gali perkelti krūvininkus į nepusiausvyrinę būseną, kurioje jie turi perteklinę kinetinę energiją. Tokie krūvininkai vadinami karštaisiais krūvininkais, o jų energijos skirstinys dažnai aprašomas efektyviąja krūvininkų temperatūra $T_e > T_0$, jeigu greita krūvininkas-krūvininkas sklaida užtikrina kvaziterminį pasiskirstymą. Tais atvejais, kai ši sąlyga neįvykdoma, būtina taikyti nešiluminę pasiskirstymo funkciją (Dienys & Požela, 1971; Zhang et al., 2021). Literatūroje yra aprašyti įvairūs karštųjų krūvininkų sužadinimo metodai, įskaitant švitinimą mikrobangomis 0,3–300 GHz dažnių diapazone (Zhou et al., 2019), ar trumpų įtampos impulsų taikymą, kai impulsų trukmė ir šiluminis valdymas parenkami taip, kad būtų

išvengta gardelės kaitinimo (Dienys & Požela, 1971; Požela, 1993). Veikiant spinduliuotei, karštieji krūvininkai gali būti generuojami dviem atvejais. Pirma, tarpjuostinės sugerties metu (*hv* > E_g) perteklinė fotono energija, likusi po elektrono-skylės poros generacijos, perduodama krūvininkams, kurie tampa karštaisiais (Ahmed et al., 2021). Antra, mažos energijos fotonai (*hv* < E_g) gali tiesiogiai kaitinti laisvuosius krūvininkus per vidinę (laisvakrūvę) sugertį. Dėl to plataus spektro optinė spinduliuotė vienu metu gali sukelti tiek klasikinę tarpjuostinę krūvininkų generaciją, tiek tiesioginį krūvininkų kaitinimą (Ahmed et al., 2021). Po sužadinimo karštieji krūvininkai relaksuoja per sklaidos procesų kaskadą, trunkanti nuo kelių dešimčių femtosekundžių iki kelių pikosekundžių. Greita krūvininkas-krūvininkas sklaida pirmiausia suformuoja kvaziterminį pasiskirstymą esant padidėjusiai T_e, o vėliau energija išsklaidoma per optinių fononų emisiją (Conibeer et al., 2014; Zhang et al., 2021). Bendra karštųjų krūvininkų gyvavimo trukmė yra pikosekundžių eilės. Galiausiai didžioji dalis perteklinės krūvininkų energijos virsta šiluma (žr. 1.20 pav.), o tai sudaro vieną pagrindinių nuostolių kanalų, ribojančių fotovoltinės konversijos efektyvumą.

Nevienalyčiuose dariniuose karštieji krūvininkai gali indukuoti fotoįtampą (ar fotosrovę). Buvo parodyta (Umeno et al., 1978; Ašmontas et al., 1999; Ašmontas et al., 2014), kad fotonų, kurių energija yra gerokai mažesnė už draudžiamosios energijos tarpą, sugertis p-n sandūroje sukelia vadinamąją anomaliąją karštųjų krūvininkų fotoįtampą, kurios poliškumas yra priešingas įprastajai fotoįtampai sąlygotai elektronas-skylė porų generavimo. Tokia karštųjų krūvininkų fotoįtampa yra būdinga daugumai puslaidininkinių medžiagų, naudojamų fotovoltinių įtaisų gamyboje. Bendrai imant, fotoatsaką p-n sandūroje sudaro trys dedamosios (žr. 1.26 pav.) dėl: klasikinės elektronų-skylių porų generacijos, karštųjų krūvininkų termoelektromotorinės jėgos ir gardelės pakaitimo sukeltos dedamosios; pastarosios dvi yra priešingo poliškumo nei klasikinis atsakas (Gradauskas et al., 2020). Šie mechanizmai buvo stebėti tiek plačiajuosčiuose puslaidininkiuose (GaAs, Si), tiek siaurajuosčiuose (HgCdTe, InSb), o jų santykinis indėlis priklauso nuo temperatūros, sužadinimo bangos ilgio, potencialinio barjero aukščio ir pridėtos įtampos. Todėl yra poreikis atlikti sisteminę karštųjų krūvininkų fotosrovės susidarymo analizę, atsižvelgiant į temperatūrą, išorinę įtampą ir sužadinimo spektrą.

Kita vertus, karštųjų krūvininkų reiškinys atveria perspektyvias galimybes kurti infraraudonosios spinduliuotės jutiklius, veikiančius karštųjų krūvininkų reiškinio pagrindu. Skirtingai nuo įprastinių siaurajuosčių puslaidininkinių fotodetektorių, kuriems reikalingas kriogeninis aušinimas tamsinei srovei slopinti ir p-n sandūros funkcionalumui palaikyti, įrenginiai, naudojantys

karštųjų krūvininkų pernašą per valdomą potencialinį barjerą, gali veikti kambario temperatūroje, taip reikšmingai išplečiant jų praktinio taikymo galimybes.

Metodai

Šiame skyriuje pateikiama tyrime taikytų metodikų apžvalga. Teorinė analizė grindžiama fotovoltinių struktūrų modeliavimu sprendžiant susietas vienmates Poisson-Schrödinger lygtis naudojant 1D Poisson programinę įrangą, leidžiančią nustatyti energinių juostų diagramas ir krūvininkų pasiskirstymą. Eksperimentinė metodika paremta puslaidininkinių sandūrų voltamperinių (VACh) charakteristikų matavimu esant įvairioms sužadinimo ir temperatūros sąlygoms ir fotoelektrinio atsako, indukuoto impulsine lazerine spinduliuote, matavimu.

Tyrime buvo naudojami tokie bandiniai:

1. Pagaminti iš pramoninių polikristalinio silicio saulės elementų (UAB SoliTek). Emiteryje ir bazėje elektronų ir skylučių koncentracijos buvo atitinkamai $n \approx 10^{20}$ cm^{-3} ir $p \approx 10^{16}$ cm^{-3}. Saulės elementai buvo supjaustyti į 2×2 mm^2 dydžio bandinius, o metaliniai kontaktai suformuoti jų kraštuose, siekiant išvengti fotoatsako, galimai kylančio iš apšviestų kontaktų srities.
2. GaAs p-n sandūra buvo sudaryta iš 5 μm storio p-tipo sluoksnio, išauginto skystosios fazės epitaksijos būdu ant n-tipo padėklo; skylučių ir elektronų koncentracijos atitinkamai buvo 5×10^{17} cm^{-3} ir 3×10^{17} cm^{-3}. Siekiant užtikrinti patikimą ominį kontaktą, paviršiuje buvo užaugintas plonas stipriai legiruotas p^+ sluoksnis, kurio skylučių koncentracija sudarė 2×10^{18} cm^{-3}. Įtaisų gamyba apėmė standartinę fotolitografiją, po kurios sekė Au-Ge-Ni ominių kontaktų terminis garinimas ir atkaitinimas. Siekiant išvengti parazitinių fotoatsakų p-p^+ ir puslaidininkis-metalo sandūrose, p^+ sluoksnis buvo selektyviai išėsdintas, paliekant jį tik po metaliniais kontaktais. Kontaktai buvo suformuoti 2.5×2.5 mm^2 dydžio.
3. Jutiklio struktūros buvo išaugintos MBE metodu ant n tipo GaAs padėklo (elektronų koncentracija 3×10^{18} cm^{-3}). Siekiant pagerinti kristalinę kokybę, papildomai buvo užaugintas 200 nm storio n-tipo tokio paties legiravimo lygio GaAs buferinis sluoksnis. Aktyvioji sritis buvo sudaryta iš dešimties $Al_xGa_{1-x}As$ sluoksnių, kurių kiekvieno storis buvo 200 nm (bendras storis – 2 μm), o AlAs molinė dalis (x) periodiškai palaipsniui mažėjo nuo 0,3 iki 0. Elektronų tankis

šiuose sluoksniuose buvo palaikomas 10^{18} cm^{-3} lygyje. Ant aktyviosios srities buvo užaugintas 500 nm storio n-tipo GaAs sluoksnis (elektronų koncentracija 3×10^{18} cm^{-3}), siekiant užtikrinti struktūrinę ir elektrinę simetriją. Ominiai kontaktai buvo suformuoti naudojant fotolitografiją, po kurios sekė Au–Ge–Ni lydinio terminis garinimas ir atkaitinimas, užtikrinantys mažos varžos elektrinius kontaktus.

Šiame darbe VACh buvo matuojamos naudojant nuolatinės srovės zondavimo stotį „SUSS Microtec EP6“, aprūpintą „SUSS Microtec PH110“ zondais, bei didelio tikslumo I-V analizatorių „Agilent E5270B“ su „Agilent E5287A“ moduliais. Matavimų valdymas, taip pat įtampos diapazono, žingsnio dydžio ir zondų poliškumo konfigūracija buvo vykdomi naudojant programinę įrangą „Agilent EasyExpert“.

Fotoelektriniuose tyrimuose buvo naudojama specializuota matavimo schema, lazeriniai šaltiniai su apibrėžtais bangos ilgiais ir temperatūros reguliavimo įranga, siekiant ištirti, charakterizuoti ir analizuoti karštųjų krūvininkų efektą GaAs p-n sandūros dioduose, pramoniniuose polikristalinio silicio saulės elementuose ir reketiniame jutiklyje. Matavimo schemos principinė diagrama pateikta S1 pav. Visi matavimai buvo atliekami fotosrovės režime. Apkrovos varža R = 50 Ω užtikrino impedanso suderinimą ir patikimus laiko atžvilgiu išskirtus fotoatsako matavimus. Išorinis priešįtampis buvo tiekiamas savadarbiu nuolatinės įtampos šaltiniu (0–9 V, 0–0,3 A).

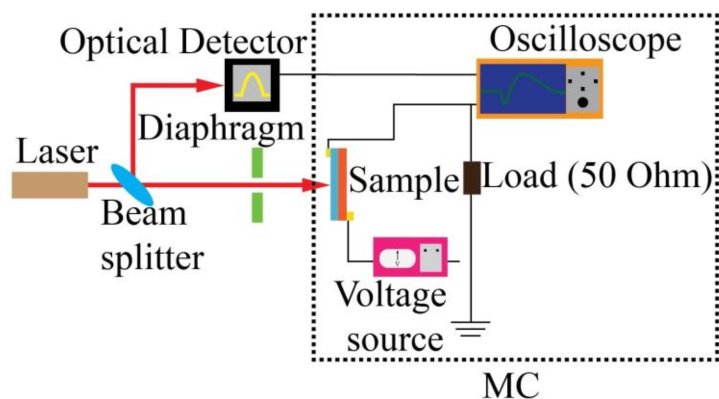

S1 pav. Fotosrovės tyrimo struktūrinė schema. Brūkšniuotas stačiakampis žymi matavimo grandinę (MC), naudotą skirtingų bangos ilgių lazerinio sužadinimo įtakai tirti.

Matavimo grandinę (MC) sudarė tiriamasis bandinys, 50 Ω apkrovos varža, skaitmeninis atmintinis oscilografas ir nuolatinės įtampos šaltinis (S1 pav.). Fotoįtampos ir lazerio impulsų laikiniai profiliai buvo registruojami skaitmeniniu atmintiniu osciloskopu „Agilent Technologies DSO6102A“, užtikrinančiu 2,5 ps laiko skyrą ir matavimo tikslumą ± 2,0 % (įtampa) bei ± 0,0015 % (laikas). Lazerio impulso forma buvo vienu metu stebima naudojant didelio greičio optinį etaloninį detektorių 11HSP-FS1 (UAB Standa). Matavimai buvo atliekami 80–300 K temperatūrų diapazone, o žemos temperatūros sąlygos buvo palaikomos naudojant savadarbį optinį kriostatą.

Mėginių apšvietimui buvo naudojami keturi lazerinės spinduliuotės šaltiniai. Sužadinimui 0,532 μm bangos ilgio spinduliuote buvo naudojamas diodais pumpuojamas, padvigubinto dažnio neodimiu legiruoto itrio aliuminio granato (Nd:YAG) lazeris su netiesiniu LBO kristalu NL202 (UAB Ekspla). Lazeris generavo 7–12 ns trukmės impulsus, esant 50 Hz kartojimosi dažniui. Liekamoji infraraudonoji spinduliuotė buvo nuslopinta naudojant harmonikų separatorių (dichroinį spindulio daliklį) (UAB Eksma), praleidžiantį tik 0,532 μm spinduliuotę. Galia buvo reguliuojama kintamu slopintuvu, sudarytu iš Briusterio tipo poliarizatoriaus ir kvarcinės pusbangės plokštelės. Vidutinė optinė galia buvo matuojama „Thorlabs Inc.“ galios matuokliu PM400, o maksimali impulso intensyvumo vertė siekė apie 0,414 MW/cm^2. Sužadinimui 1,064 μm bangos ilgiu buvo naudojamas Nd:YAG lazeris, generuojantis 10–17 ns trukmės impulsus, esant 50 Hz kartojimosi dažniui ir maksimaliai impulso intensyvumo vertei iki 10 MW/cm^2. Spinduliuotės intensyvumas buvo reguliuojamas naudojant skirtingo pralaidumo optinius filtrus. Sužadinimui 1,342 μm bangos ilgio spinduliuote buvo naudojamas neodimiu legiruoto itrio ortovanadato (Nd:YVO_4) diodinis lazeris, generuojantis 1,7 ns trukmės impulsus, kurių intensyvumas kito nuo 0,06 kW/cm^2 iki 0,4 MW/cm^2. Papildomi eksperimentai buvo atlikti naudojant ir 2 μm bangos ilgio spinduliuotės ultratrumpus lazerio impulsus (apie 0,5 ps), o intensyvumas kito nuo 1,76 iki 3 MW/cm^2.

Rezultatai

Sužadinimo bangos ilgis (fotonų energija) turi lemiamą įtaką tiek krūvininkų kaitinimo, tiek generacijos sukeltam fotoatsakui. Karštieji krūvininkai gali būti sužadinami fotonais, kurių energija yra mažesnė už puslaidininkio draudžiamosios energijos tarpą, ir fotonais, kurių energija jį viršija.

S2 paveiksle pateiktos voltamperinės charakteristikos, išmatuotos esant skirtingų bangos ilgių lazeriniam apšvietimui, išlaikant vienodą spinduliuotės intensyvumą. Apšvietus GaAs p-n sandūrą 1,342 μm (0,92 eV) bangos ilgio spinduliuote, beveik išimtinai stebima tik karštųjų krūvininkų fotosrovė, nes fotonų energija yra nepakankama krūvininkų generacijai. Esant 1,064 μm (1,16 eV) bangos ilgiui, karštųjų krūvininkų komponentė dominuoja prieš klasikinę generacijos sąlygotą fotosrovę, kylančią dėl dvifotonės sugerties. Tai siejama ne tik su tiesioginiu laisvųjų krūvininkų kaitinimu dėl laisvakrūvės sugerties, bet ir su perteklinės energijos (2 × 1,16 eV – 1,42 eV = 0,9 eV), liekančios po elektronas-skylė porų generavimu, perdavimu papildomam krūvininkų kaitinimui.

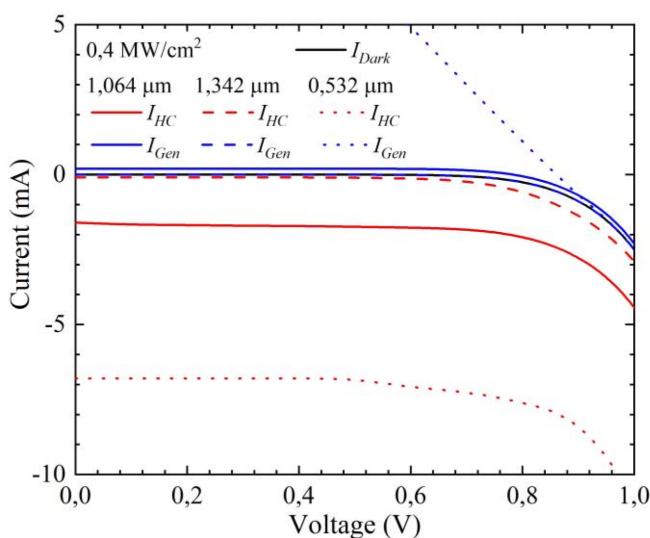

S2 pav. GaAs p-n sandūros voltamperinės charakteristikos, išmatuotos esant 0,4 MW/cm^2 intensyvumo lazeriniam apšvietimui: 1,064 μm (ištisinės linijos), 1,342 μm (brūkšninės linijos) ir 0,532 μm (taškinės linijos) bangos ilgiai; kambario temperatūroje (Gradauskas et al., 2024).

Sužadinant 0,532 μm (2,32 eV > E_g(GaAs)) bangos ilgio spinduliuote, taip pat stebima ryški karštųjų krūvininkų fotosrovė, priešingai nei būtų tikimasi pagal klasikinį požiūrį. Šis efektas greičiausiai siejamas su likutine energija (~ 0,92 eV), išliekančia po vienfotonės tarpujuostinės sugerties. Kaip matyti S3 paveiksle, dviejų fotosrovės komponenčių spektrinės charakteristikos pasižymi nevienareikšmiu elgesiu. Esant pastoviam sužadinimo intensyvumui, sumažėjus fotonų energijai (bangos ilgis 1,342 μm vietoje 1,064 μm), generacijos sukelta komponentė I_{Gen} beveik visiškai išnyksta, o

karštųjų krūvininkų komponentė I_{HC} taip pat sumažėja, nors ir mažesniu mastu. Toks sumažėjimas negali būti paaiškintas vien tik laisvųjų krūvininkų sugerties mechanizmu, kuris klasikinėje teorijoje paklūsta λ^2 dėsniui (Szuszkiewicz, 1996).

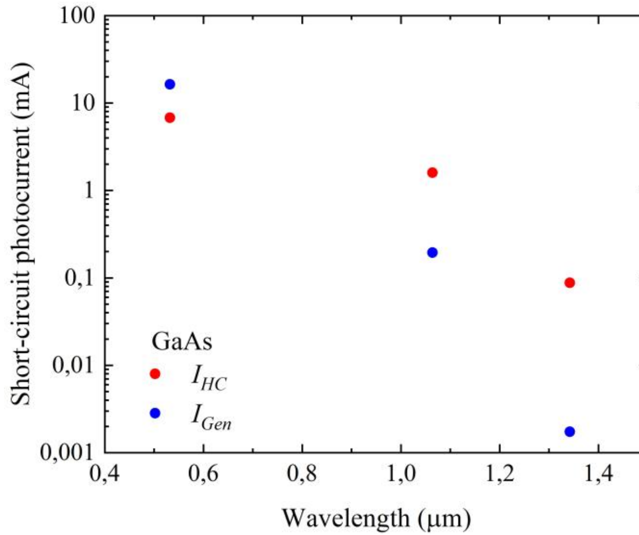

S3 pav. GaAs p-n sandūros trumpojo jungimo karštųjų krūvininkų (raudoni taškai) ir krūvininkų generacijos (mėlyni taškai) fotosrovių spektrinė priklausomybė, išmatuota esant 0,4 MW/cm^2 intensyvumo lazeriniam apšvietimui kambario temperatūroje (Gradauskas et al., 2024).

Tai rodo, kad krūvininkų kaitimas, o kartu ir karštųjų krūvininkų fotosrovės susidarymas, priklauso ir nuo likutinės energijos, išliekančios po dviejų fotonų sugerties: sumažinus fotono energiją nuo 1,16 eV iki 0,9 eV, perteklinė energija sumažėja nuo 0,92 eV iki 0,42 eV. Esant trumpesnio bangos ilgio sužadinimui (0,532 μm vietoje 1,064 μm), ima dominuoti vienfotonė tarpjuostinė sugertis, lemianti ženklų generacijos sukeltos fotosrovės sustiprėjimą. Tuo pat metu maždaug 0,92 eV likutinė fotono energija ir toliau prisideda prie laisvųjų krūvininkų kaitinimo, tuo pabrėžiant sudėtingą sąveiką tarp generacijos sukeltų ir karštųjų krūvininkų mechanizmų.

Silicio p-n sandūroje karštųjų krūvininkų fotosrovė, indukuota 1,064 μm spinduliuotės (fotono energija viršija draudžiamosios energijos tarpą), trumpojo jungimo sąlygomis nėra stebima. Ji pasireiškia tik esant pakankamai dideliam tiesioginiam priešįtampiui, apie 0,8 V (žr. S4 pav. intarpą), kai potencialinis barjeras tampa pakankamai žemas, ir karštieji krūvininkai gali jį

įveikti. Padidinus sužadinimo bangos ilgį iki 1,342 µm, generacijos fotosrovė sumažėja, o karštųjų krūvininkų komponentė sustiprėja (S4 pav.).

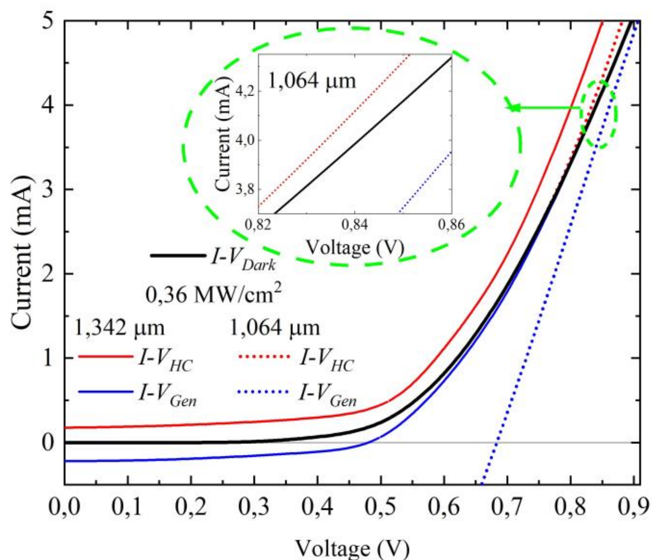

S4 pav. Silicio saulės elemento voltamperinės charakteristikos kambario temperatūroje. Intarpe pateikta padidinta didelių priešįtampių sritis, išmatuota esant 1,064 µm bangos ilgio apšvietimui (Zharchenko et al., 2024).

Skirtingas karštųjų krūvininkų fotoatsakas į ilgesnių bangų sužadinimą silicyje, palyginti su GaAs, greičiausiai susijęs su statesne tarpjuostinės sugerties spektrine priklausomybe ties draudžiamosios energijos kraštu; dėl to lieka daugiau perteklinės energijos laisvųjų krūvininkų sugerčiai ir jų kaitinimui. Papildomi eksperimentai su silicio dariniais, sužadinant juos 0,532 µm bangos ilgiu, nerodė jokios karštųjų krūvininkų fotosrovės. Intensyvi fotonų, kurių energija $h\nu \geq E_g$, tarpjuostinė sugertis visiškai nuslopina karštųjų krūvininkų fotosrovės indėlį.

Karštųjų krūvininkų fotosrovė stiprėja didėjant tiesioginiam priešįtampiui (S5 pav.). Esant maždaug 0,7 V įtampai, ši priklausomybė pasižymi būdingu lūžio tašku, kurį viršijus fotosrovė ima sparčiai augti. Toks eksponentinis didėjimas kyla dėl perėjimo nuo impulsinės poslinkio srovės, pasireiškiančios esant atbulinei ir mažai tiesioginei įtampai, prie karštųjų krūvininkų pernašos per p-n sandūros potencialinį barjerą, sumažintą pridėtu priešįtampiu.

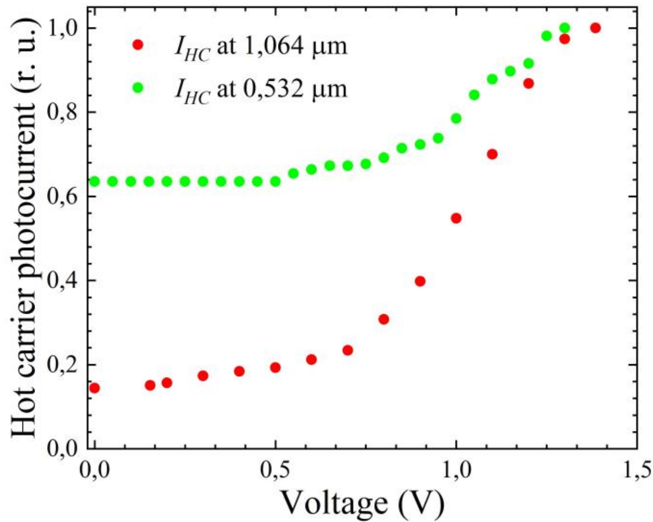

S5 pav. Normalizuotos karštųjų krūvininkų fotosrovės priklausomybės nuo priešįtampio GaAs p-n sandūroje, išmatuotos kambario temperatūroje, sužadinant 0,532 μm (žali taškai) ir 1,064 μm (raudoni taškai) bangų ilgio lazerine spinduliuote.

Karštųjų krūvininkų poslinkio fotosrovė yra analogiška kintamajai srovei, tekančiai per kondensatorių, ir pasireiškia tik esant impulsiniam krūvininkų kaitinimui, kurio metu vyksta sandūros talpos persikrovimas (Ašmontas et al., 1997). Toliau didinant tiesioginį priešįtampį, karštųjų krūvininkų fotosrovė įsisotina dėl potencialinio barjero sumažėjimo (Umeno et al., 1978).

S6 paveiksle pateikti tipiniai fotosrovės impulso laikiniai profiliai silicio p-n sandūroje, nesant išorinio priešįtampio (šviesiai žalia kreivė) ir esant +0,4 V tiesioginiam priešįtampiui (alyvinė kreivė), kai mėginys sužadinamas 1,342 μm bangos ilgio lazerio impulsu (apatinė rožinė kreivė) kambario temperatūroje.Matyti, kad laikinė fotoatsako forma susideda iš kelių komponenčių. Greitas pradinio subimpulso augimas, taip pat jo poliškumas, aiškiai rodo, kad ši komponentė priskirtina karštųjų krūvininkų fotosrovei I_{HC}. Tiesioginis priešįtampis sudaro palankias sąlygas karštųjų krūvininkų pernašai per sumažintą potencialinį barjerą ir kartu slopina generacijos sąlygotą srovę.

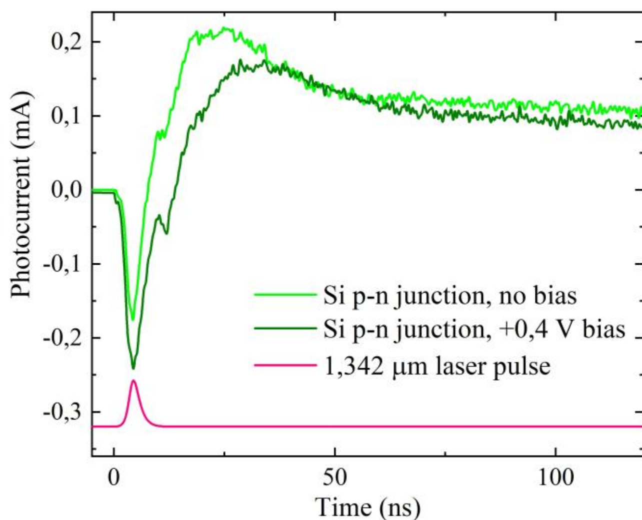

S6 pav. Tipiniai fotrosrovės impulsai Si p-n sandūroje nesant (šviesiai žalia) ir esant tiesioginiam +0,4 V (alyvinė) priešįtampiui, sužadinant 1,342 µm bangos ilgio lazerio impulsu. Kambario temperatūra. Lazerio impulsas (rožine) pateiktas ne mastelyje (Gradauskas et al., 2024).

Matyti, kad laikinė fotoatsako forma susideda iš kelių komponenčių. Greitas pradinio subimpulso augimas, taip pat jo poliškumas, aiškiai rodo, kad ši komponentė priskirtina karštųjų krūvininkų fotosrovei I_{HC}. Tiesioginis priešįtampis sudaro palankias sąlygas karštųjų krūvininkų pernašai per sumažintą potencialinį barjerą ir kartu slopina generacijos sąlygotą srovę.

S7 paveiksle parodyta abiejų fotosrovės komponenčių maksimalių verčių priklausomybė nuo priešįtampio. Ypač išsiskiria staigus karštųjų krūvininkų komponentės I_{HC} padidėjimas esant tiesioginiam priešįtampiui didesniam už 0,5 V. Panaši eiga buvo aprašyta ir kitų autorių darbuose (Marmur & Oksman, 1975; Umeno et al., 1978; Ašmontas et al., 2017), kas patvirtina šio efekto universalumą. Toks staigus augimas interpretuojamas kaip palankių sąlygų karštiesiems krūvininkams pereiti per sandūrą pasiekimas, susijęs su potencialinio barjero sumažėjimu.

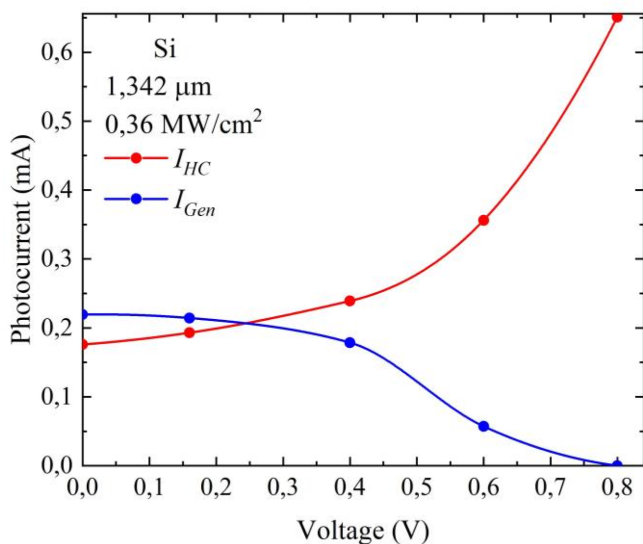

S7 pav. Karštųjų krūvininkų fotosrovės (raudona) ir generacijos fotosrovės (mėlyna) priklausomybė nuo priešįtampio kambario temperatūroje (Zharchenko et al., 2024).

Šie rezultatai parodo lemiamą tiesioginio priešįtampio vaidmenį formuojantis karštųjų krūvininkų fotosrovei Si ir GaAs p-n sandūrose.

Fotosrovės formavimosi pobūdis stipriai priklauso nuo krintančios spinduliuotės intensyvumo. Atitinkamos eksperimentinės priklausomybės GaAs atveju pateiktos S8 paveiksle.

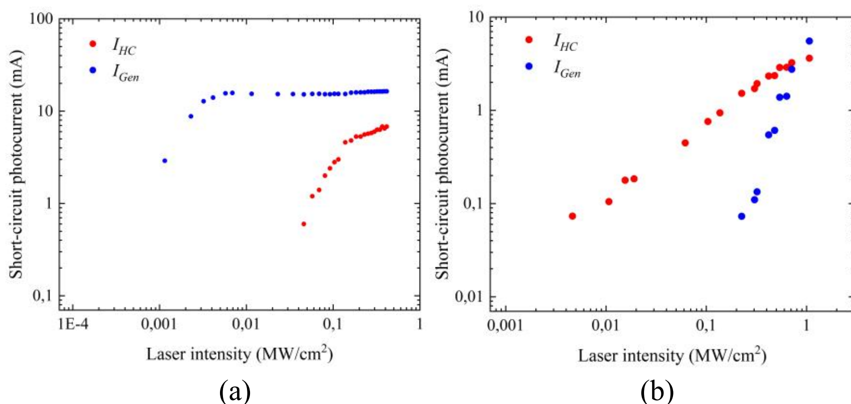

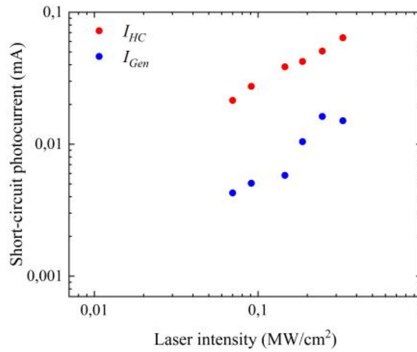

(c)

S8 pav. GaAs p-n sandūros trumpojo jungimo karštųjų krūvininkų (raudoni taškai) ir generacijos sukeltų (mėlyni taškai) fotosrovių priklausomybė nuo lazerinės spinduliuotės intensyvumo, sužadinant 0,532 µm (a), 1,064 µm (b) ir 1,342 µm (c) bangos ilgio spinduliuote. Kambario temperatūra.

Esant 0,532 µm bangos ilgio apšvietimui (S8a), fotosrovė greitai pasiekia sotį dėl dominuojančios stiprios tarpjuostinės šviesos sugerties. Karštųjų krūvininkų fotosrovė tampa pastebima tik tuomet, kai klasikinė (generacinė) fotosrovė jau yra soties režime. Esant 1,064 µm bangos ilgio apšvietimui (S8b), maksimali karštųjų krūvininkų fotosrovės vertė didėja tiesiškai didėjant lazerinės spinduliuotės intensyvumui. Priešingai, klasikinė fotosrovė rodo kvadratinę priklausomybę nuo intensyvumo, kas patvirtina jos kilmę iš dvifotonės sugerties. Esant 1,342 µm bangos ilgio apšvietimui (S8c), karštųjų krūvininkų fotosrovė taip pat demonstruoja tiesinę priklausomybę nuo lazerinės spinduliuotės intensyvumo. Priešingo poliškumo fotosrovės dedamoji priskirtina fototalpuminiam reiškiniui, susijusiam su karštaisiais krūvininkais.

Silicio bandiniuose taip pat buvo stebima ryški fotoatsako dedamųjų priklausomybė nuo lazerinės spinduliuotės galios (S9 pav.). Šiuo atveju, generacijos sukelta fotosrovė beveik kvadratiniu dėsniu priklauso nuo sužadinimo intensyvumo, kas yra būdinga dvifotonės sugerties procesams. Jei karštųjų krūvininkų fotrosrovę sąlygoja vien tik laisvakrūvė sugertis, ji turėtų paklusti tiesiniam dėsniui; dabar gi – subtiesinė priklausomybė.

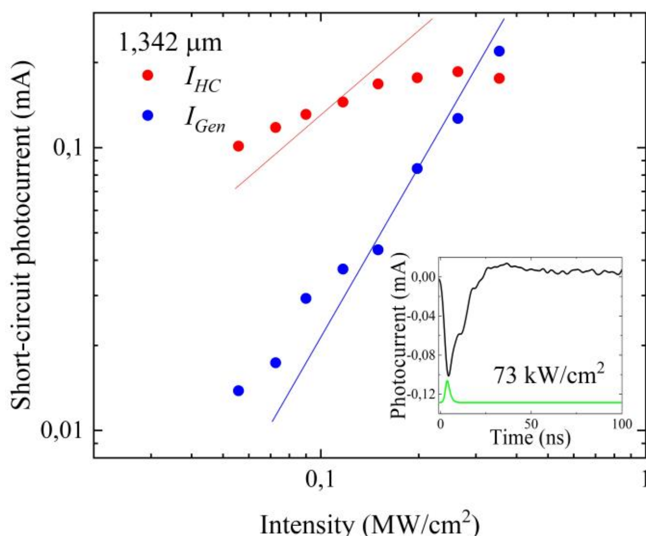

S9 pav. Trumpojo jungimo fotrosrovių I_{HC} ir I_{Gen} priklausomybė nuo lazerinės spinduliuotės (1,342 µm bangos ilgio) intensyvumo pramoninėse silicio struktūrose kambario temperatūroje. Tiesės pateiktos kaip atitinkamų tiesinio ir kvadratinio dėsnių iliustracinės gairės. Intarpe – trumpojo jungimo fotrosrovės impulsas ir lazerio impulsas apačioje (ne mastelyje) (Zharchenko et al., 2024).

To priežastys galimos trys. Pirma, didėjant sužadinimo galiai, dvifotonės sugerties koeficientas didėja, todėl laisvakrūvei sugerčiai lieka vis mažiau fotonų. Antra, dviejų fotonų energija, kuri lieka po dvifotonės generacijos ir yra panaudojama krūvininkų kaitinimui, yra mažesnė nei vieno fotono energija, kuri gali būti panaudojama laisvakrūvei sugerčiai ($2 \times 0{,}92$ eV – 1,12 eV = 0,72 eV < 0,92 eV). Trečia, generacinė fotosrovės komponentė slopina priešingo poliškumo karštųjų krūvininkų komponentę, nes sužadinimo intensyvumui didėjant ji auga dvigubai greičiau.

S10 paveikslе matyti, kad mažėjant temperatūrai tamsinės VACh kreivė pasislenka į didesnių įtampų pusę, o tai atspindi potencialinio barjero aukščio padidėjimą dėl temperatūros pokyčio.

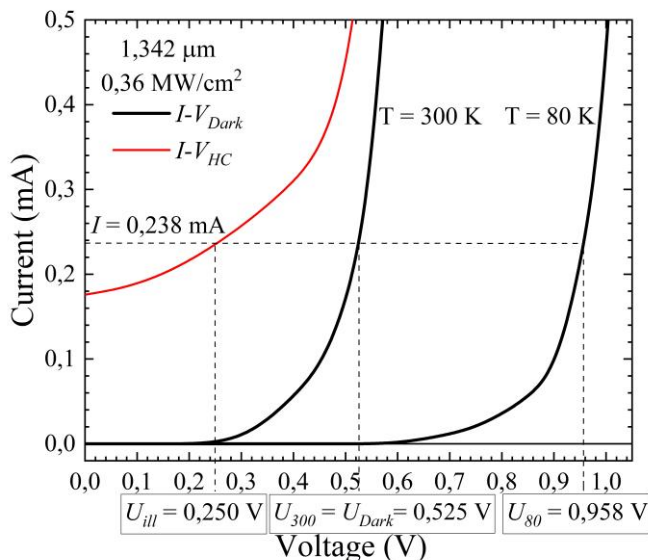

S10 pav. Silicio saulės elemento voltamperinės charakteristikos tamsoje kambario ir skystojo azoto temperatūrose (juodos linijos) bei karštųjų krūvininkų VACh kambario temperatūroje (raudona linija) (Zharchenko et al., 2024).

Egzistuoja vadinamasis temperatūrinis įtampos koeficientas α_T, kuris apibūdina diodo VACh charakteristikos poslinkį keičiantis temperatūrai (Schaffner & Shea, 1955):

$$\alpha_T = \frac{\Delta U}{\Delta T} |I = const|. \tag{4.1}$$

Fotovoltiniuose įrenginiuose α_T paprastai yra neigiamas: didėjant temperatūrai, įtampa (esant pastoviai srovei) mažėja. Kiekvienai puslaidininkinei medžiagai būdingos savitos šio koeficiento vertės. Siliciui tipiškos α_T vertės patenka į nuo –1,8 iki –2,2 mV/K intervalą, kas patvirtina didelį potencialinio barjero aukščio jautrumą temperatūros pokyčiams (Green & Blakers, 1982; Zhao et al., 1994; Cotfas et al., 2018). Remiantis tamsinėmis VACh, nustatytas temperatūrinis koeficientas $\alpha_T = -1.97$ mV/K. Panaudojant atitinkamas įtampų vertes iš kambario temperatūros tamsinės ir karštųjų krūvininkų voltamperinių charakteristikų (S10 pav.) ir pritaikius apskaičiuotą α_T reikšmę, gaunamas krūvininkų ir kristalinės gardelės temperatūrų skirtumas:

$$\Delta T = \frac{U_{ill} - U_{Dark}}{\alpha_T} |I = 0.238\, mA| = 140\, K. \quad (4.2)$$

Tokiu būdu įvertinta krūvininkų temperatūra silicyje siekia maždaug 440 K, kai mėginys buvo veikiamas mažesnių už draudžiamosios energijos tarpą fotonų 1,342 µm bangos ilgio lazerine spinduliuote, esant 0,36 MW/cm^2 galios tankiui ir nanosekundžių trukmės impulsams, atrodo pagrįsta. Svarbu pabrėžti, kad siūlomas metodas leidžia gauti apytikslį, tačiau nesudėtingą ir tarpusavyje suderintą karštųjų krūvininkų temperatūros įvertinimą.

Skirtingų tipų šviesos jutikliai susiduria su savitais apribojimais, kurie lemia jų tinkamumą konkrečioms taikymo sritims. Vienus riboja nepakankamas jautrumas silpniems signalams, kitus – maksimalus veikimo greitis, dar kitus – aptinkamo spektro diapazonas, o kai kurių veikimą riboja ir darbinės temperatūros intervalas. Elektroniniai reketo (ratchet) tipo įrenginiai siūlo alternatyvų sprendimą, suteikiant kryptį atsitiktiniam krūvininkų judėjimui naudojant asimetrinius potencialus. Tačiau esami jų projektai pasižymi dideliu technologiniu sudėtingumu. Šiame darbe siūlomas $Al_xGa_{1-x}As$ reketinis jutiklis, paremtas karštųjų krūvininkų reiškiniu, turi būdingus derinamus asimetrinius potencialinius barjerus ir pasižymi optimizuota krūvininkų pernaša, todėl užtikrina plačią spektrinę jautrą bei sumažintą technologinį sudėtingumą. Reketo tipo jutiklio veikimas, paremtas karštųjų krūvininkų reiškiniu, schematiškai pavaizduotas S11 paveiksle.

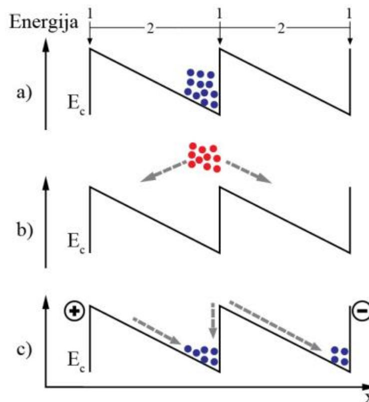

S11 pav. Reketinio jutiklio periodinis potencialas ir schematinis elektronų persiskirstymas laidumo juostoje: (a) apšvitos nėra; (b) spinduliuote pakaitintų karštųjų elektronų difuzija abiem kryptimis; (c) elektronų relaksacija ir persiskirstymas tarp potencialinių duobių. E_C žymi laidumo juostos apačią, o apskritimuose esantys pliuso ir minuso ženklai nurodo indukuotos elektrovaros jėgos poliškumą.

Nesant apšvitos, laisvieji elektronai yra susitelkę periodinio asimetrinio potencialo duobėse (S11a pav.). Apšvietimo metu vidutinė elektronų energija padidėja, jie tampa karštaisiais krūvininkais ir difunduoja abiem kryptimis išilgai *x* ašies (S11b pav.). Karštiesiems elektronams prarandant perteklinę energiją (vėstant), jie relaksuoja iki laidumo juostos dugno ir, veikiami potencialo gradiento, dreifuoja gretimų potencialinių šulinių link (S11c pav.). Dalis krūvininkų įveikia barjerą ir patenka į gretimą šulinį, o kiti grįžta į pradinį. Tokiu būdu jutiklio galuose indukuojama elektrovaros jėga, o uždaroje elektrinėje grandinėje teka srovė.

Pagamintas reketinis $Al_{0.3}Ga_{0.7}As/GaAs$ jutiklis buvo veikiamas trijų skirtingų bangos ilgių lazerine spinduliuote, siekiant išanalizuoti jo spektrinio atsako ypatybes.

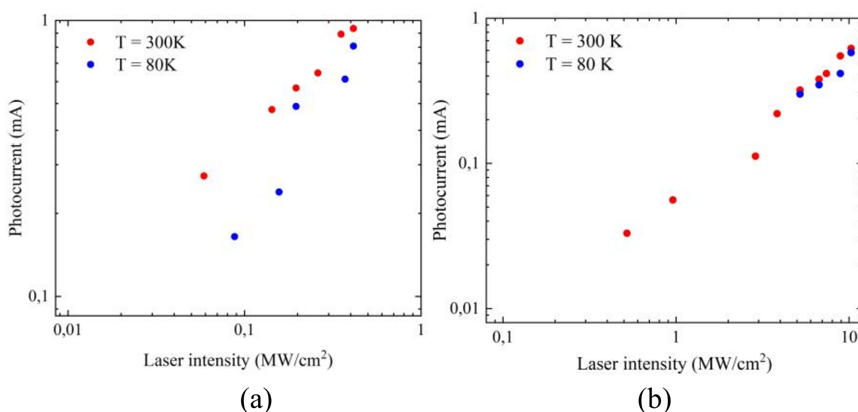

S12 pav. Reketinio jutiklio fotosrovės priklausomybė nuo lazerinės spinduliuotės intensyvumo kambario temperatūroje (raudoni taškai) ir skystojo azoto temperatūroje (mėlyni taškai), esant (a) 0,532 μm ir (b) 1,064 μm bangos ilgio lazeriniam apšvietimui.

Apšvietus struktūrą λ = 0,532 μm bangos ilgio spinduliuote (S12a pav.), joje vyksta efektyvi tarpjuostinė sugertis, todėl fotosrovė tiesiškai priklauso nuo lazerio spinduliuotės galios. Visame tirtame intensyvumų diapazone fotosrovė kambario temperatūroje yra didesnė nei skystojo azoto temperatūroje. Šį skirtumą galima paaiškinti tuo, kad tarpjuostinės sugerties koeficientas GaAs puslaidininkyje kambario temperatūroje yra didesnis (Dargis & Kundrotas, 1994), o draudžiamosios energijos tarpo didėjimas žemėjant temperatūrai palieka mažiau energijos sugeneruotų krūvininkų kaitinimui. Jutiklis demonstruoja tiesinę fotosrovės priklausomybę ir nuo 1,064 μm (S12b pav.), ir nuo 2,0 μm (neparodyta) lazerinės spinduliuotės

galios visame tirtame diapazone. Tai rodo, kad signalo formavimosi mechanizmas nėra valdomas tarpjuostinės dvifotonės sugerties, bet yra susijęs su laisvųjų krūvininkų kaitimu ir vėlesne karštųjų krūvininkų pernaša. Tiesinė fotosrovės eiga patvirtina, kad didėjant švitinimo intensyvumui vidutinė krūvininkų energija proporcingai auga, todėl tirtame galios diapazone nefiksuojami soties požymiai. Be to, esant 1,064 µm bangos ilgio lazeriniam apšvietimui (S12b pav.), temperatūrinis nuokrypis tarp kreivių yra minimalus, kas aiškinama tuo, jog fotoatsakas susidaro išimtinai dėl laisvųjų krūvininkų sugerties, nepriklausančios nuo puslaidininkio draudžiamosios energijos tarpo, o dvifotonė sugertis žemesnėje temperatūroje yra slopinama draudžiamosios energijos tarpo padidėjimu.

Išvados

1. Karštųjų krūvininkų fotosrovės formavimąsi GaAs ir Si p-n sandūrose lemia sužadinimo bangos ilgis. Spinduliuotė, kurios fotonų energija yra mažesnė už draudžiamosios energijos juostos plotį, sukelia laisvųjų krūvininkų kaitimą ir ryškų karštųjų krūvininkų indėlį, tuo tarpu trumpesni bangos ilgiai yra palankesni generacijos sąlygotai fotosrovei, kartu dalį energijos perduodant krūvininkų kaitimui.
2. Fotosrovė stipriai priklauso nuo sužadinimo sąlygų ir paklūsta skirtingiems mastelio dėsniams. Sužadinant ilgabange spinduliuote, karštųjų krūvininkų indėlis beveik tiesiškai priklauso nuo mažų sužadinimo intensyvumų, o didesnių intensyvumų srityje yra stebima generacijos sąlygota dedamoji, pasižyminti kvadratine priklausomybe nuo intensyvumo, kas yra būdinga dvifotonei tarpjuostinei sugerčiai. Sužadinant didelės energijos fotonais, dominuoja generacijos fotosrovė, o karštųjų krūvininkų komponentė išryškėja tik tuomet, kai ši dedamoji pasiekia sotį.
3. Krūvininkų įkaitimas ir konkurencija tarp karštųjų krūvininkų bei generacijos sąlygotų srovių yra universalus reiškinys tiek tiesioginės, tiek ir netiesioginės draustinės juostos puslaidininkiuose, kaip parodyta GaAs ir Si atveju – įskaitant ir pramoninius saulės elementus. Tai pabrėžia jų fundamentinį vaidmenį fotovoltinės konversijos procese.
4. Išorinė įtampa yra svarbus parametras, darantis įtaką karštųjų krūvininkų fotosrovės realizavimui. Kai potencialinis barjeras pakankamai sumažinamas, karštieji krūvininkai gali efektyviai įveikti sandūrą, dėl to staigiai padidėja karštųjų krūvininkų indėlis į bendrą fotosrovę.

5. Temperatūros poveikis sąveikai tarp karštųjų krūvininkų ir generacijos fotosrovės dedamųjų nėra akivaizdus. Aušinimas vienu metu sustiprina krūvininkų kaitimo efektus dėl pailgėjusios energijos relaksacijos trukmės ir slopina tiek laisvakrūvę, tiek irtarpjuostinę sugertį. Kuris mechanizmas taps dominuojantis, priklauso nuo sužadinimo intensyvumo: esant mažiems intensyvumams vyrauja karštųjų krūvininkų indėlis, kuris dar labiau išryškėja mažinant temperatūrą.
6. Įtampos-temperatūros koeficiento metodika leidžia kiekybiškai įvertinti karštųjų krūvininkų temperatūrą p-n sandūrose. Voltamperinių charakteristikų poslinkio analizė esant apšvietimui fotonais, kurių energija mažesnė už draudžiamų energijų tarpą, parodo, kad krūvininkų temperatūra gali būti tiesiogiai nustatoma iš elektrinių charakteristikų. Tai suteikia diagnostinį įrankį nepusiausvyrųjų krūvininkų dinamikos tyrimui, kurio rezultatai atitinka literatūroje pateiktus duomenis.
7. Sukurtas reketo tipo jutiklis veikia esant sužadinimui tiek mažos, tiek ir didelės energijos fotonams. Jo fotoatsakas kyla dėl karštųjų krūvininkų kaitimo, kurį sukelia tiek klasikiniai tarpjuostinės, tiek laisvakrūvės sugerties mechanizmai, kas užtikrina jautrį plačiame spektro ruože, viršijančiame įprastinių (tarpjuostinių) fotodetektorių ribas.
8. Temperatūriniai tyrimai parodė, kad, sužadinant didelės energijos fotonais, jutiklio jautris didėja kylant temperatūrai, tuo tarpu sužadinant mažos energijos fotonais jis išlieka beveik nepriklausomas nuo temperatūros. Tai patvirtina stabilią jutiklio veiką kambario temperatūroje ir išryškina šį esminį jo pranašumą, lyginant su įprastiniais infraraudonosios spinduliuotės jutikliais, kuriems yra būtinas kriogeninis aušinimas.

PUBLIKACIJŲ SARAŠAS

Disertacijos pagrindas

(A1) **Zharchenko I.**, Gradauskas J., Masalskyi O., Rodin A. “Hot carrier photocurrent induced by 0.92 eV photon energy radiation in a Si solar cell.” Opto-Electronics Review, 2024 32(2), 1-6.
doi: 10.24425/opelre.2024.150181.
(A2) Gradauskas J., Masalskyi O., Ašmontas S., Sužiedėlis A., Rodin A., **Zharchenko I**. “Hot carrier photocurrent as an intrinsic loss in a single junction solar cell.” Ukr. J. Phys. Opt., 2024, 25(1), 01106-01112.
doi: 10.3116/16091833/Ukr.J.Phys.Opt.2024.01106.
(A3) Ašmontas S., Masalskyi O., **Zharchenko I.**, Gradauskas J. “Some Aspects of Hot Carrier Photocurrent across GaAs p-n Junction.” Inorganics, 2024, 12(174), 1–9. doi: 10.3390/inorganics12060174.

Kitos publikacijos

(A4) Sužiedėlis A., Ašmontas S., Gradauskas J., Čerškus A., Lučun A., Anbinderis M., **Zharchenko I.** “Anisotropy of Voltage Sensitivity of Bow-Tie Microwave Diodes Containing 2DEG Layer .” – Crystals, 2025 15(367), 1-18. doi: 10.3390/cryst15040367
(P1) Gradauskas J., Ašmontas S., Sužiedėlis A., Masalskyi O., **Zharchenko I.** „Reketinis plataus spektro spinduliuotės jutiklis“ („Ratchet-based sensor of broad radiation spectrum“). Lietuvos Respublikos patentas Nr. LT 7030B (2023/02/17).

Konferencijos

(C1) V. Kyshchun, Ya. Faier, O. Masalskyi, **I. Zharchenko**, J. Gradauskas, A. Šilėnas, A. Čerškus. “Sensor based on hot carrier effect for electromagnetic radiation detection” – OpenReadings 2025 – 68th International Conference for Students of Physics Natural Sciences, May 13 – 16, 2025.
(C2) **I. Zharchenko**, J. Gradauskas, O. Masalskyi, S. Ašmontas, A. Sužiedėlis, A. Šilėnas, A. Čerškus, V. Kyshchun. “Evidence of Hot Carrier Effect in a Silicon Solar Cell” – Fiztech2024 – 14th Conference of Doctoral Students and Young Scientists, October 15 – 17, 2024.
(C3) O. Masalskyi, J. Gradauskas, **I. Zharchenko**, S. Ašmontas, A. Sužiedėlis, A. Šilėnas, A. Čerškus, E. Širmulis, V. Kyshchun.

"Peculiarities of hot carrier transport across GaAs p-n junction" – The APROPOS 19 Scientific Conference, October 1 – 4, 2024.

(C4) **I. Zharchenko**, J. Gradauskas, O. Masalskyi, S. Ašmontas, A. Sužiedėlis, A. Čerškus. "Unveiling Spectral Peculiarities of Hot Carrier Phenomena in GaAs Solar Cells" – «Lashkaryov's readings- 2024» Young scientists conference on semiconductor physics, April 4, 2024.

(C5) O. Masalskyi, J. Gradauskas, **I. Zharchenko**, S. Ašmontas, A. Sužiedėlis, A. Šilėnas, A. Čerškus, A. Rodin. "Exploring the unavoidable hot carrier effect in GaAs p-n junction" – 45-oji Lietuvos nacionalinė fizikos konferencija, October 25 – 27, 2023.

(C6) **I. Zharchenko**, J. Gradauskas, O. Masalskyi, S. Ašmontas, A. Sužiedėlis, A. Šilėnas, A. Čerškus. "Exploring Spectral and Temperature Aspects of Hot Carrier Phenomena in GaAs Solar Cells" – Fiztech2023 – 13th Conference of Doctoral Students and Young Scientists, October 18 – 19, 2023.

(C7) J. Gradauskas, S. Ašmontas, O. Masalskyi, A. Sužiedėlis, A. Šilėnas, A. Čerškus, A. Rodin and **I. Zharchenko**. "Peculiarities of hot carrier effect in GaAs p-n junction" – EU PVSEC 2023 – The 40th European Photovoltaic Solar Energy Conference & Exhibition, September 18 – 22, 2023.

(C8) **I. Zharchenko**, O. Masalskyi, J. Gradauskas, S. Ašmontas, A. Sužiedėlis, A. Šilėnas, A. Čerškus, A. Rodin. "Investigating Hot Carrier Effects in GaAs P-N Diodes under Pulsed Laser Irradiation" – MATERIALS OF INTERNATIONAL SCIENTIFIC AND TECHNICAL CONFERENCE LASER TECHNOLOGIES. LASERS AND THEIR APPLICATION – LTLA – 2023, June 29 – 30, 2023.

(C9) **I. Zharchenko**, O. Masalskyi, J. Gradauskas, S. Ašmontas, A. Sužiedėlis, A. Šilėnas, A. Čerškus, A. Rodin. "Spectral peculiarities of hot carrier phenomenon in a solar cell" – Open readings 2023: 66th international conference for students of physics and natural sciences, April 18 – 21, 2023.

(C10) J. Gradauskas, S. Ašmontas, **I. Zharchenko**, O. Masalskyi, A. Sužiedėlis, A. Šilėnas, A. Čerškus, A. Rodin and P. Augustinas. "Low and high photon energy induced photoresponse in single junction solar cells" – The APROPOS 18 Scientific Conference, October 5 – 7, 2022.

(C11) J. Gradauskas, S. Ašmontas, O. Masalskyi, A. Sužiedėlis, A. Šilėnas, A. Čerškus, A. Rodin and **I. Zharchenko**. "Pre-thermalizational impact of hot carriers on photovoltage formation in a single junction solar cell" – The 8th World Conference on Photovoltaic Energy Conversion, September 26 – 30, 2022.

(C12) O. Masalskyi, J. Gradauskas, S. Ašmontas, A. Sužiedėlis, A. Šilėnas, A. Čerškus, A. Rodin and **I. Zharchenko**. "Direct hot carrier impact on photovoltage of a solar cell" – The 23rd Sde Boker Symposium on Solar Electricity Production, September 5 – 7, 2022.
(C13) O. Masalskyi, J. Gradauskas, **I. Zharchenko**. "Photovoltage formation across GaAs p-n junction under intense laser light" – DOC 2022 – 18th International Young Scientist Conference Developments in Optics and Communications, April 21 – 22, 2022.
(C14) O. Masalskyi, J. Gradauskas, S. Ašmontas, A. Sužiedėlis, A. Šilėnas, A. Čerškus, A. Rodin, **I. Zharchenko**. "Hot carriers in photoresponse formation across GaAs p-n junction" – Open Readings 2022 – 65 The international conference for students of physics and natural sciences, March 15 – 18, 2022.

REFERENCES

Aberle, A. G. Overview on SiN surface passivation of crystalline silicon solar cells. *Solar Energy Materials & Solar Cells*, 65(1), 2001, 239–248. https://doi.org/10.1016/S0927-0248(00)00099-4

Adachi, S. (1998). Optical dispersion relations for GaP, GaAs, GaSb, InP, InAs, InSb, $Al_xGa_{1-x}As$, and $In_{1-x}Ga_xAs_yP_{1-y}$. *Journal of Applied Physics*, *66*(12), 6030. https://doi.org/10.1063/1.343580

Adams, W. G., Day, R. E. (1877). "On the action of light on selenium." *Philosophical Transactions of the Royal Society of London*, 167, 313–349. URL: https://www.jstor.org/stable/109173

Ahmed, I.; Shi, L.; Pasanen, H.; Vivo, P.; Maity, P.; Hatamvand, M.; Zhan, Y. There is plenty of room at the top: generation of hot charge carriers and their applications in perovskite and other semiconductor-based optoelectronic devices. *Light: Science & Applications*, 10(1), 2021, 1–28. https://doi.org/10.1038/s41377-021-00609-3

Al-Ashouri, A., Köhnen, E., Li, B., Magomedov, A., Hempel, H., Caprioglio, P., Márquez, J. A., Morales Vilches, A. B., Kasparavicius, E., Smith, J. A., Phung, N., Menzel, D., Grischek, M., Kegelmann, L., Skroblin, D., Gollwitzer, C., Malinauskas, T., Jošt, M., Matič, G., Rech, B., Schlatmann, R., Unold, T., Korte, L., Abate, A., Stannowski, B., Neher, D., Stolterfoht, M., & Albrecht, S. Monolithic perovskite/silicon tandem solar cell with >29% efficiency. *Science*, 370(6522), 2020, 1300–1309. https://doi.org/10.1126/science.abd4016

AMOLF. (n.d.). *Detailed balance charts*. Retrieved from https://amolf.nl/research/sustainable-energy-materials/detailed-balance-charts

Ašmontas, S., Gradauskas, J., Kazlauskaitė, V., Sužiedėlis, A., Širmulis, E., & Vingelis, M. (2008). *GaAs/AlGaAs heterojunction as a fast detector of infrared laser pulses*. Proceedings of SPIE, 7142, 71420N. https://doi.org/10.1117/12.815954

Ašmontas, S., Gradauskas, J., Seliuta, D., Sužiedėlis, A., Šilėnas, A., & Valušis, G. (1997). GaAs/AlGaAs heterojunction: A promising detector for infrared radiation. In Proceedings of the 5th European Gallium Arsenide and Related III–V Compounds Applications Symposium (GAAS '97) (pp. 345–348). Bologna, Italy. https://doi.org/10.6092/UNIBO/AMSACTA/1336

Ašmontas, S., Gradauskas, J., Seliuta, D., Sužiedėlis, A., Šilėnas, A., Širmulis, E., Valiušis, G., & Tetyorkin, V. V. (2002). CO_2 laser induced hot

carrier photoeffect in HgCdTe. Materials Science Forum, 384–385, 147–150. https://doi.org/10.4028/www.scientific.net/MSF.384-385.147

Ašmontas, S., Gradauskas, J., Seliuta, D., Sužiedėlis, A., Širmulis, E., Tetyorkin, V. V., Urbelis, A., & Alusis, G. (2003). Influence of free carrier heating on IR light detection in narrow-gap semiconductors. In *proc. of conference of Advanced Optical Devices, Technologies, and Medical Applications* 243–247. https://doi.org/10.1117/12.517029

Ašmontas, S., Gradauskas, J., Seliuta, D., Sužiedėlis, A., Valušis, G., & Širmulis, E. (2003). *Fast infrared detectors based on nonuniform semiconductors*. Proceedings of SPIE, 5123, 221–230. https://doi.org/10.1117/12.517026

Ašmontas, S., Gradauskas, J., Sužiedelis, A., Šilėnas, A., Širmulis, E., Švedas, V., Vaicikauskas, V., Vaiciūnas, V., Žalys, O., & Kostylyov, V. (2018). Photovoltage formation across Si p–n junction exposed to laser radiation. Materials Science-Poland, 36(2), 337–340. https://doi.org/10.1515/msp-2017-0106

Ašmontas, S., Gradauskas, J., Sužiedėlis, A., Šilėnas, A., Širmulis, E., Švedas, V., Vaičikauskas, V., Vaičiūnas, V., Valiulis, D., Žalys, O., & Kostylyov, V. (2017). Peculiarities of photovoltage formation across p–n junction under illumination of laser radiation. Solid State Phenomena, 267, 167–171. https://doi.org/10.4028/www.scientific.net/SSP.267.167

Ašmontas, S.; Dashevsky, Z.; Dariel, M. P.; Gradauskas, J.; Jarašiūnas, A.; Shusterman, S.; Sužiedėlis, A.; Valušis, G. Photo-thermovoltaic effects induced by CO_2 laser illumination of PbTe–metal junctions. *Proceedings of SPIE*, 4318, 2001, 230–236. https://doi.org/10.1117/12.432922

Ašmontas, S.; Gradauskas, J.; Seliuta, D.; Šilėnas, A. Photoemf of hot carriers in nonuniform GaAs. In: Silinsh, E. A.; Medvids, A.; Lusis, A. R.; Ozols, A. O. (eds.), *Proceedings of the International Conference on Advanced Optical Devices, Technologies, and Medical Applications*. Proc. SPIE, 1997, pp. 104–109. https://doi.org/10.1117/12.266815

Ašmontas, S.; Gradauskas, J.; Seliuta, D.; Širmulis, E. Photoemf of hot carriers in nonuniform GaAs. *Proc. SPIE*. 1996, 2968, 104–109. https://doi.org/10.1117/12.2077437

Ašmontas, S.; Gradauskas, J.; Seliuta, D.; Širmulis, E. Photoresponse in nonuniform semiconductor junctions under infrared laser excitation. *Proceedings of SPIE*, 3890, 1999, 125–132. https://doi.org/10.1117/12.373162

Ašmontas, S.; Gradauskas, J.; Sužiedėlis, A.; Šilėnas, A.; Širmulis, E.; Vaičikauskas, V.; Žalys, O. Hot carrier impact on photovoltage formation in

solar cells. *Applied Physics Letters*, 113(7), 2018, 071103. https://doi.org/10.1063/1.5043155

Ašmontas, S.; Gradauskas, J.; Sužiedėlis, A.; Šilėnas, A.; Vaičikauskas, V.; Žalys, O.; Steikūnas, G.; Steikūnienė, A. Photoelectric properties of GaAs p-n junction under illumination of intense laser radiation. *Proceedings of SPIE*, 9421, 2014, 942102. https://doi.org/10.1117/12.2077437

Auzel, F. Upconversion and anti-Stokes processes with f and d ions in solids. *Chemical Reviews*, 104(1), 2004, 139-173. https://doi.org/10.1021/cr020357g

Baiju, A., & Yarema, M. Status and challenges of multi-junction solar cell technology. *Frontiers in Energy Research*, 10, 2022, article 971918. https://doi.org/10.3389/fenrg.2022.971918

Beard, M. C.; Luther, J. M.; Nozik, A. J. The promise and challenge of nanostructured solar cells. *Nature Nanotechnology*, 9(12), 2014, 951-954. https://doi.org/10.1038/nnano.2014.292

Becquerel, Alexandre-Edmond. Mémoire sur les effets électriques produits sous l'influence des rayons solaires. *Comptes Rendus de l'Académie des Sciences*, Vol. 9 (1839), pp. 561–567. URL: https://scholar.google.com/scholar_lookup?title=Recherches%20sur%20les%20effets%20de%20la%20radiation%20chimique%20de%20la%20lumiere%20solaire%20au%20moyen%20des%20courants%20electriques&author=A.E.%20Becquerel&publication_year=1839&pages=145-149

Bello, S.; Urwick, A.; Bastianini, F.; Nedoma, A. J.; Dunbar, A. An introduction to perovskites for solar cells and their characterisation. *Energy Reports* 2022, 8, 89–106. https://doi.org/10.1016/j.egyr.2022.08.205

Brennan, L. J.; Byrne, M. T.; Bari, M.; Gun'ko, Y. K. Carbon nanomaterials for dye-sensitized solar cell applications: A bright future. *Advanced Energy Materials*, 2011, 1(4), 472 – 485. https://doi.org/10.1002/aenm.201100136

Brennan, M. C.; Zinna, J.; Kuno, M. Existence of a Size-Dependent Stokes Shift in $CsPbBr_3$ Perovskite Nanocrystals. *ACS Energy Letters* 2017, 2(7), 1487–1488. https://doi.org/10.1021/acsenergylett.7b00383

Bristow, A. D.; Rotenberg, N.; van Driel, H. M. Two-photon absorption and Kerr coefficients of silicon for 850–2200 nm. *Applied Physics Letters*. 2007, 90(19), 191104. https://doi.org/10.1063/1.2737359

Bush, K. A., Palmstrom, A. F., Yu, Z., Boccard, M., Cheacharoen, R., Mailoa, J. P., McMeekin, D. P., Hoye, R. L. Z., Bailie, C. D., Leijtens, T., Peters, I. M., Minichetti, M. C., Rolston, N., Prasanna, R., Sofia, S., Harwood, D., Ma, W., Moghadam, F., Snaith, H. J., Buonassisi, T., Holman, Z., Bent, S. F., & McGehee, M. D. 23.6%-efficient monolithic perovskite/silicon tandem

solar cells with improved stability. *Nature Energy*, 2, 2017, 17009. https://doi.org/10.1038/nenergy.2017.9

Chapin, D. M.; Fuller, C. S.; Pearson, G. L. A New Silicon p–n Junction Photocell for Converting Solar Radiation into Electrical Power. *Journal of Applied Physics*, Vol. 25, No. 5 (1954), pp. 676–677. DOI: 10.1063/1.1721711

Chen, B., Yu, Z. J., Manzoor, S., Wang, S., Weigand, W., Yu, Z., Yang, G., Ni, Z., Dai, X., Holman, Z. C., & Huang, J. Blade-Coated Perovskites on Textured Silicon for 26-Efficient Monolithic Perovskite/Silicon Tandem Solar Cells. *Joule*, 4(4), 2020, 850–864. https://doi.org/10.1016/j.joule.2020.01.008

Conibeer, G. "Third-generation photovoltaics." *Materials Today*, 10(11), 2007, 42-50. https://doi.org/10.1016/S1369-7021(07)70278-X

Conibeer, G., Shrestha, S., Huang, S., Patterson, R., Xia, H., Feng, Y., Zhang, P., Gupta, N., Tayebjee, M., Smyth, S., Liao, Y., Zhang, Z., Chung, S., Lin, S., Wang, P., & Dai, X. Hot carrier solar cell absorbers: materials, mechanisms and nanostructures. *Next Generation Technologies for Solar Energy Conversion V*, 9178, 2014, 917802. https://doi.org/10.1117/12.2067926

Cotfas, D. T.; Cotfas, P. A.; Machidon, O. M. Study of temperature coefficients for parameters of photovoltaic cells. *Int. J. Photoenergy*. 2018, 2018, 5945602. https://doi.org/10.1155/2018/5945602

Dargys, A., & Kundrotas, J. (1994). Handbook on the physical properties of Ge, Si, GaAs and InP. *Physics-Uspekhi*, 39(7), 743–774. https://doi.org/10.1070/PU1996V039N07ABEH001526

De Vos, A. J. Detailed balance limit of the efficiency of tandem solar-cells. *Journal of Physics D: Applied Physics* 1980, 13(5), 839-846. https://doi.org/10.1088/0022-3727/13/5/018

Denis, J.; Požela, J. Methods of carrier heating in semiconductors. *Lithuanian Journal of Physics (Lietuvos Fizikos Rinkinys)*, 11, 1971, 345–356.

Ding, Y., Li, H., Haider, M., Gao, Y., Yang, J., Yi, C., & Zheng, Z. (2024). *Perovskite/organic tandem solar cells: A review*. Energy Lab, 2, 230002. https://doi.org/10.54227/elab.20230002

Du X, Heumueller T, Gruber W, Classen A, Unruh T, Li N, et al. Efficient polymer solar cells based on non-fullerene acceptors with a potential device lifetime approaching 10 years. *Joule*. 2019; 3: 215-26. https://doi.org/10.1016/j.joule.2018.09.001

Einstein, A. Über einen die Erzeugung und Verwandlung des Lichtes betreffenden heuristischen Gesichtspunkt. *Annalen der Physik*, Vol. 17 (1905), pp. 132–148. DOI: 10.1002/andp.19053220607

Ekins-Daukes, N. J., Lee, K.-H., Hirst, L., Chan, A., Führer, M., Adams, J., Browne, B., Barnham, K. W. J., Stavrinou, P., Connolly, J., Roberts, J. S., Stevens, B., Airey, R., & Kennedy, K. Controlling radiative loss in quantum well solar cells. *Journal of Physics D: Applied Physics*, 46(26), 2013, 264007. https://doi.org/10.1088/0022-3727/46/26/264007

Encinas Sanz, F., Guerra Pérez, J. M., & Domínguez Ferrari, E. (1993). *CO_2 laser induced photoeffects in silicon junctions*. IEEE Journal of Quantum Electronics, 29(4), 1223–1227. https://doi.org/10.1109/3.214509

Encinas-Sanz, F., & Guerra, J. M. (2003). *Hot carrier photovoltaic effects in semiconductor junctions*. Progress in Quantum Electronics, 27(4–5), 267–294. https://doi.org/10.1016/S0079-6727(03)00002-8

Garnett, E., & Yang, P. D. "Light Trapping in Silicon Nanowire Solar Cells." *Nano Letters*, 10(3), 2010, pp. 1082-1087. DOI: 10.1021/nl100161z

Geisz, J. F., France, R. M., Schulte, K. L., Steiner, M. A., Norman, A. G., Guthrey, H. L., Young, M. R., Song, T., & Moriarty, T. Six-junction III-V solar cells with 47.1% conversion efficiency under 143 Suns concentration. *Nature Energy*, 5(4), 2020, 326–335. https://doi.org/10.1038/s41560-020-0598-5

Goetzberger, Adolf; Knobloch, Joachim; Voß, Bernhard. Crystalline Silicon Solar Cells. *John Wiley & Sons, Ltd.*, 1998. ISBN 978-0-471-97144-3. URL: https://books.google.lt/books/about/Crystalline_Silicon_Solar_Cells.html?id=1ztkQgAACAAJ&redir_esc=y

Gradauskas, J.; Ašmontas, S.; Sužiedėlis, A.; Šilėnas, A.; Vaičikauskas, V.; Čerškus, A.; Širmulis, E.; Žalys, O.; Masalskyi, O. Influence of hot carrier and thermal components on photovoltage formation across the p–n junction. *Applied Sciences*, 10, 2020, 7483. https://doi.org/10.3390/app10217483

Green, M. A. (2008). Self-consistent optical parameters of intrinsic silicon at 300 K including temperature coefficients. *Solar Energy Materials and Solar Cells*, *92*(11), 1305–1310. https://doi.org/10.1016/J.SOLMAT.2008.06.009

Green, M. A. Photovoltaics: Technology Overview. *Energy Policy*, Vol. 28, No. 14 (2000), pp. 989-998. DOI: 10.1016/S0301-4215(00)00086-0

Green, M. A. *Silicon Solar Cells: Advanced Principles & Practice*. Kensington, N.S.W.: Centre for Photovoltaic Devices & Systems, University of New South Wales, 1995. 366 p. ISBN 0733409946 (ISBN-13: 978-0733409943). URL: https://www.semanticscholar.org/paper/Silicon-solar-cells-%3A-advanced-principles-and-Green/ea4e385943366555b1535c0dfcb8e8e01670bac1

Green, M. A. Solar cell fill factors: General graph and empirical expressions. *Solid State Electronics*, 24(6-7), 1981, 788-789. https://doi.org/10.1016/0038-1101(81)90062-9

Green, M. A. Third Generation Photovoltaics: Advanced Solar Energy Conversion. *Springer Series in Photonics*. Berlin, Heidelberg: Springer-Verlag, 2006. 160 p. ISBN 978-3-540-40137-7. URL: https://books.google.lt/books/about/Third_Generation_Photovoltaics.html?id=81WI2LwrpkcC&redir_esc=y

Green, M. A., Hishikawa, Yoshihiro, Dunlop, Ewan D., Levi, Dean H., Hohl-Ebinger, Jochen, Yoshita, Masahiro, Ho-Baillie, Anita W.Y. Solar Cell Efficiency Tables (Version 53). *Progress in Photovoltaics: Research and Applications*, Vol. 27, No. 1 (2019), pp. 3-12. DOI: 10.1002/pip.3102.

Green, M. A.; Emery, K.; Blakers, A. W. Silicon solar cells with reduced temperature sensitivity. *Electron. Lett.* 1982, 18(3), 97–98. https://doi.org/10.1049/el:19820066

Henry, C. H. Limiting efficiencies of ideal single and multiple energy gap terrestrial solar cells. *Journal of Applied Physics, 51(8)*, 1980, 4494–4500. https://doi.org/10.1063/1.328272

Hirst, L. C., & Ekins-Daukes, N. J. Fundamental losses in solar cells. *Progress in Photovoltaics: Research and Applications*, 19(3), 2011, 286–293. https://doi.org/10.1002/pip.1024

Hu, L.; Chen, G. Analysis of optical absorption in silicon nanowire arrays for photovoltaic applications. *Nano Letters*, 7(11), 2007, 3249–3252. https://doi.org/10.1021/nl071018b

Yamaguchi, Masafumi; Takamoto, Takuya; Araki, Kenji; Ekins-Daukes, Nicholas J. Multi-junction solar cells: current status and future potential. *Solar Energy*, 82(2), 2008, p. 173–180. https://doi.org/10.1016/j.solener.2007.07.009

Kamat, P. V. Quantum Dot Solar Cells: The Next Big Thing in Photovoltaics. *The Journal of Physical Chemistry Letters* 2013, 4(6), 908-918. https://doi.org/10.1021/jz400052e

Klimov, V. I. Detailed-balance power conversion limits of nanocrystal-quantum-dot solar cells in the presence of carrier multiplication. *Applied Physics Letters*, 89(12), 2006, 123118. https://doi.org/10.1063/1.2356314

Klimov, V. I. Nanocrystal Quantum Dots, 2nd ed.; *CRC Press, Taylor & Francis Group: Boca Raton*, FL, USA, 2017. https://doi.org/10.1201/9781420079272

Krishnamurthy, S.; Yu, Z. G.; Gonzalez, L. P.; Guha, S. Temperature- and wavelength-dependent two-photon and free-carrier absorption in GaAs, InP,

GaInAs, and InAsP. *J. Appl. Phys.* 2011, 109(3), 033102. https://doi.org/10.1063/1.3549136

Kumar, B. K., & Gupta, N. D. Nanostructured anti-reflection coating for absorption enhancement in perovskite silicon tandem solar cells. *Optical Materials Express*, 14(1), 2024, 139–154. https://doi.org/10.1364/OME.503990

Kurtz, S., Myers, D., McMahon, W. E., Geisz, J., & Steiner, M. A Comparison of Theoretical Efficiencies of Multi-junction Concentrator Solar Cells. *Progress in Photovoltaics: Research and Applications*, 16(6), 2008, 537–546. https://doi.org/10.1002/pip.830

Lamanna, E.; Matteocci, F.; Calabrò, E.; Serenelli, L.; Menchini, F.; Lamanna, L.; Di Carlo, A.; Tucci, M. Mechanically stacked, two-terminal graphene-based tandem solar cells. Joule 2020, 4(4), 865–881. https://doi.org/10.1016/j.joule.2020.01.015

Landsberg, P. T., & Tonge, G. Thermodynamic limit for conversion of sunlight to electricity. *Journal of Applied Physics*, 51(8), 1980, 494–498. https://doi.org/10.1063/1.328187

Lau, B., & Kedem, O. (2020). Electron ratchets: State of the field and future challenges. The Journal of Chemical Physics, 152(20), 200901. https://doi.org/10.1063/5.0009561

Lau, W. H.; Brown, T.; Conibeer, G. Hot carrier relaxation dynamics in quantum confined semiconductor nanostructures. *Nat. Mater.* 2017, 16(9), 951–956. https://doi.org/10.1038/nmat4065

Lee, M. M.; Teuscher, J.; Miyasaka, T.; Murakami, T. N.; Snaith, H. J. Efficient hybrid solar cells based on meso-superstructured organometal halide perovskites. *Science* 2012, *338*(6107), 643-647. https://doi.org/10.1126/science.1228604

Li, T., Chen, Z., Wang, Y., Tu, J., Deng, X., Li, Q., et al. (2020). Materials for interfaces in organic solar cells and photodetectors. *ACS Applied Materials & Interfaces, 12*(3), 3301–3326. https://doi.org/10.1021/acsami.9b19830

Li, X.; Yu, H.; Liu, Z.; et al. Progress and Challenges Toward Effective Flexible Perovskite Solar Cells. Nano-Micro Letters 2023, 15, 206. https://doi.org/10.1007/s40820-023-01165-8

Linke, H., Humphrey, T. E., Löfgren, A., Sushkov, A. O., Newbury, R., Taylor, R. P., & Omling, P. (1999). Experimental tunneling ratchets. *Science, 286*(5448), 2314–2317. https://doi.org/10.1126/science.286.5448.2314

Liu, J.; Dong, Q.; Wang, M.; Ma, H.; Pei, M.; Bian, J.; Shi, Y. Efficient Planar Perovskite Solar Cells with Carbon Quantum Dot-Modified spiro-MeOTAD as a Composite Hole Transport Layer. *ACS Appl. Mater. Interfaces* 2021, 13, 56265–56272. https://doi.org/10.1021/acsami.1c18344

Liu, M., Johnston, M. B., & Snaith, H. J. (2013). Efficient planar heterojunction perovskite solar cells by vapour deposition. *Nature, 501*(7467), 395–398. https://doi.org/10.1038/nature12509

Liu, X.; Wu, J.; Guo, Q.; Yang, Y.; Luo, H.; Liu, Q.; Lan, Z. Pyrrole: An additive for improving the efficiency and stability of perovskite solar cells. *J. Mater. Chem. A* 2019, 7, 11764–11770. https://doi.org/10.1039/C9TA02916H

Malinkiewicz, O., Yella, A., Lee, Y. H., Espallargas, G. M., Graetzel, M., & Nazeeruddin, M. K. (2014). Perovskite solar cells employing organic charge-transport layers. *Nature Photonics, 8*(2), 128–132. https://doi.org/10.1038/nphoton.2013.341

Marmur, I. Ya.; Oksman, O. Effect of 10.6 μm laser radiation on the current of a forward biased photodiode. *Semiconductors (Fiz. Tekh. Poluprovodn.)*. 1975, 11, 2121–2124 (in Russian).

Martí, A., & Araújo, G. L. Limiting efficiencies for photovoltaic energy conversion in multigap systems. *Solar Energy Materials & Solar Cells*, 43(3-4), 1996, 203-222. https://doi.org/10.1016/0927-0248(96)00015-3

Masalskyi, O., & Gradauskas, J. Pre-themalizational effect of hot carriers on photovoltage formation in a solar cell. *Ukrainian Journal of Physical Optics*, 23(3), 2022, 117–125. https://doi.org/10.3116/16091833/23/3/117/2022

McCrea, A. Renewable Energy: A User's Guide. 1st ed. Marlborough, *UK: Crowood Press*, 2008. 192 p. ISBN 978-1-84797-579-2. URL: https://scholar.google.com/scholar_lookup?title=Renewable%20Energy%3A%20A%20User%D7%B3s%20Guide&author=A.%20McCrea&publication_year=2008

Morgan, T. N. The mobility of electrons heated by microwave fields in n-type germanium. *Journal of Physics and Chemistry of Solids*, **8**, 1959, 245–249. https://doi.org/10.1016/0022-3697(59)90327-0

Nell, M. E., & Barnett, A. M. The spectral p-n junction model for tandem solar-cell design. *IEEE Transactions on Electron Devices*, 34(2), 1987, 257-266.

Nelson, J. The Physics of Solar Cells: Properties of Semiconductor Materials. *World Scientific / Imperial College Press*, 2003. ISBN-10: 1-86094-349-7; ISBN-13: 978-1-86094-349-2. URL: https://books.google.lt/books/about/The_Physics_Of_Solar_Cells.html?id=4Ok7DQAAQBAJ&redir_esc=y

Ning, Z.; Gong, X.; Comin, R.; Walters, G.; Fan, F.; Voznyy, O.; Yassitepe, E.; Buin, A.; Hoogland, S.; Sargent, E. H. Quantum-dot-in-

perovskite solids. *Nature* 2015, 523, 324–328. https://doi.org/10.1038/nature14563

Nozik, A. J. Quantum Dot Solar Cells. Physica E: Low-Dimensional *Systems and Nanostructures* 2002, 14(1-2), 115-120. https://doi.org/10.1016/S1386-9477(02)00374-0

Pelouch, W. S.; Ogawa, S.; Galbraith, I.; Hwang, J. C. M.; Gibbs, H. M. Comparison of hot carrier relaxation in quantum wells and bulk GaAs at high carrier densities. *Phys. Rev. B*. 1992, 45(3), 1450–1453. https://doi.org/10.1103/PhysRevB.45.1450

Perlin, John. *Silicon Solar Cell Turns 50*. US: National Renewable Energy Laboratory, 2004. URL: https://www.osti.gov/biblio/15009471

Petrulėnas, A. *Femtosecond Pulse Generation in the 1.1–3 μm Range by Parametric and Stimulated Raman Amplification of Supercontinuum*. Doctoral Dissertation, Vilnius University, Center for Physical Sciences and Technology, Physics (N 002), Vilnius, 2025. https://doi.org/10.15388/vu.thesis.729

Petrus ML, Schlipf J, Li C, Gujar TP, Giesbrecht N, Müller-Buschbaum P, et al. Capturing the Sun: A review of the challenges and perspectives of perovskite solar cells. *Adv Energy Mater.* 2017; 7: 1700264. https://doi.org/10.1002/aenm.201700264

Planck, M. Ueber das Gesetz der Energieverteilung im Normalspectrum. *Annalen der Physik*, Vol. 4, No. 553 (1901), pp. 553–563. DOI: 10.1002/andp.19013090310

Polman, A., & Atwater, H. A. Photonic design principles for ultrahigh-efficiency photovoltaics. *Nature Materials*, 11(3), 2012, 174–177. https://doi.org/10.1038/nmat3263

Polman, A., Knight, M., Garnett, E. C., Ehrler, B., & Sinke, W. C. Photovoltaic materials: Present efficiencies and future challenges. *Science*, 352(6283), 2016, article aad4424. https://doi.org/10.1126/science.aad4424

Požela, J. Hot-Electron Transistors. In G. Vebrene (Ed.), *Physics of High-Speed Transistors* (1st ed., pp. 197–236). Springer US, 1993. https://doi.org/10.1007/978-1-4899-1242-8_7

Queisser, H. J. Detailed balance limit for solar cell efficiency. *Materials Science and Engineering: B*, 159–160, 2009, 322–325. https://doi.org/10.1016/j.mseb.2008.06.033

Razykov, T. M., Ferekides, C. S., Morel, D., Stefanakos, E., Ullal, H. S., Upadhyaya, H. M. Solar photovoltaic electricity: Current status and future prospects. *Solar Energy*, Vol. 85, No. 8 (2011), pp. 1580-1608. DOI: 10.1016/j.solener.2010.12.002

Ren, Y.; Zhang, D.; Suo, J.; Cao, Y.; Eickemeyer, F. T.; Vlachopoulos, N.; Grätzel, M. Hydroxamic acid pre-adsorption raises the efficiency of cosensitized solar cells. *Nature*, Vol. 613 (2023), pp. 60–65. DOI: 10.1038/s41586-022-05455-z.

Richards, B. S. Luminescent layers for enhanced silicon solar cell performance: down-conversion. *Solar Energy Materials & Solar Cells*, 90(8), 2006, pp. 1189-1207. https://doi.org/10.1016/j.solmat.2005.07.001

Richter, A., Glunz, S. W., Werner, F., & Cuevas, A. Improved quantitative description of Auger recombination in crystalline silicon. *Physical Review B*, 86(16), 2012, 165202. https://doi.org/10.1103/PhysRevB.86.165202

Roeling, E. M., Germs, W. C., Smalbrugge, B., Geluk, E. J., de Vries, T., Janssen, R. A. J., & Kemerink, M. (2011). Organic electronic ratchets doing work. Nature Materials, 10(1), 51–55. https://doi.org/10.1038/nmat2922

Rogalski, A. (2005). HgCdTe infrared detector material: history, status and outlook. *Reports on Progress in Physics*, *68*(10), 2267. https://doi.org/10.1088/0034-4885/68/10/R01

Ross, R. T., & Nozik, A. J. Efficiency of hot-carrier solar energy converters. *Journal of Applied Physics*, 53(5), 1982, 3813. https://doi.org/10.1063/1.331124

Rühle, Sven. "Tabulated Values of the Shockley–Queisser Limit for Single-Junction Solar Cells." *Solar Energy*, Vol. 130 (2016), pp. 139-147. DOI: 10.1016/j.solener.2016.02.015.

Santos, I. M.; Alexandre, M.; Vicente, António T.; et al. Next-Generation Solar-Powering: Photonic Strategies for Earth and Space Systems. *Solar RRL*, 2025. https://doi.org/10.1002/solr.202400666

Sargent, E. H. *Colloidal quantum dot solar cells*. *Nature Photonics* 2012, *6*(3), 133-135. https://doi.org/10.1038/nphoton.2012.33

Sato, S. A.; Shinohara, Y.; Otobe, T.; Yabana, K. Dielectric response of laser-excited silicon at finite electron temperature. *Phys. Rev. B*. 2014, 90(17), 174303. https://doi.org/10.1103/PhysRevB.90.174303

Schaeffer, John. *Solar Living Source Book*. 30th anniversary edition. Hopland, CA: Gaiam Real Goods, 2008. 582 p. ISBN 978-0-9794094-0-1. URL: https://books.google.ne/books?id=l-hSAAAAMAAJ

Schaffner, J. S.; Shea, R. F. The variation of the forward characteristics of junction diodes with temperature. *Proc. Inst. Radio Eng.* 1955, 43, 101. URL: https://ieeexplore.ieee.org/document/4055239

Schaller, R. D.; Klimov, V. I. High Efficiency Carrier Multiplication in PbSe Nanocrystals: Implications for Solar Energy Conversion. *Physical Review Letters*, 92(18), 2004, 186601. URL: https://doi.org/10.1103/PhysRevLett.92.186601

Semonin, O. E., Luther, J. M., Choi, S., Chen, H. Y., Gao, J., Nozik, A. J., & Beard, M. C. Peak external photocurrent quantum efficiency exceeding 100% via multiple exciton generation in a quantum dot solar cell. *Science*, 334(6062), 2011, 1530–1533. https://doi.org/10.1126/science.1209845

Shah, N.; Shah, A. A.; Leung, P. K.; Khan, S.; Sun, K.; Zhu, X.; Liao, Q. A Review of Third Generation Solar Cells. *Processes*, Vol. 11, No. 6 (2023), Art. 1852. DOI: 10.3390/pr11061852.

Shalav A.; Richards B. S.; Trupke T.; Krämer K. W.; Güdel H. U. Application of $NaYF_4:Er^{3+}$ Up-Converting Phosphors for Enhanced Near-Infrared Silicon Solar Cell Response. *Applied Physics Letters*, 86(1), 2005, 013505. https://doi.org/10.1063/1.1844592

Sharma, S.; Siwach, B.; Ghoshal, S.K.; Mohan, D. Dye sensitized solar cells: From genesis to recent drifts. *Renew. Sustain. Energy Rev*. 2017, 70, 529–537. https://doi.org/10.1016/j.rser.2016.11.136

Shockley, W., & Queisser, H. J. Detailed balance limit of efficiency of p-n junction solar cells. *Journal of Applied Physics*, 32(3), 1961, 510–519. https://doi.org/10.1063/1.1736034

Shockley, W., & Read, W. T. Statistics of the Recombinations of Holes and Electrons. *Physical Review*, 87(5), 1952, 835–842. https://doi.org/10.1103/PhysRev.87.835

Spaans, E. M., Venkataraj, S., Singh, K., Ravichandran, A., Manalo, M. L., Guerra, R., Aberle, A. G., & Nampalli, N. Optical losses in silicon heterojunction solar cells: analysis of record-efficiency devices and practical limits based on ray-tracing simulations. *EES Solar*, 1, 2025, 157–171. https://doi.org/10.1039/D5EL00001G

Suresh Kumar, N.; Chandra Babu Naidu, K. A review on perovskite solar cells (PSCs), materials and applications. *Journal of Materiomics* 2021, 7 (5), 940−956. https://doi.org/10.1016/j.jmat.2021.04.002

Szuszkiewicz, W. IR absorption due to free carriers in GaAs. In: Adams, A. R. (ed.). *Gallium Arsenide (GaAs) Physics, Technology, and Devices*. EMIS Datareviews Series, vol. 16. London: INSPEC, 1996, p. 235–243

Tanaka, T.; Nakano, Y.; Kasai, S. GaAs-Based Nanowire Devices with Multiple Asymmetric Gates for Electrical Brownian Ratchets. *Jpn. J. Appl. Phys*. 2013, 52(6S), 06GE07. https://doi.org/10.7567/JJAP.52.06GE07

Trupke, T.; Green, M. A.; Ẅurfel, P. Improving Solar Cell Efficiencies by Up-Conversion of Sub-Band-Gap Light. *Journal of Applied Physics*, 92(7), 2002, 4117-4122. https://doi.org/10.1063/1.1505677

Tsokos, K. A. Physics for the IB Diploma. 5th ed. *Cambridge: Cambridge University Press*, 2008. 836 p. ISBN 0521138213, 978-0521138215. URL:

https://books.google.com/books/about/Physics_for_the_IB_Diploma.html?id=uWVQrIZqz_MC

Umeno, M.; Sugito, Y.; Jimbo, T.; Hattori, H.; Amemiya, Y. Hot photocarrier and hot electron effects in p–n junctions. *Solid-State Electronics*. 1978, 21(1), 191–195. https://doi.org/10.1016/0038-1101(78)90137-5

van Sark, W. G. J. H. M.; Meijerink, A.; Schropp, R. E. I.; Roosmalen, J. A. M.; Lysen, E. H. Enhancing solar cell efficiency by using spectral converters. *Solar Energy Materials and Solar Cells*, 87(1), 2005, 395-409. https://doi.org/10.1016/j.solmat.2004.07.055

Wu, C.; Chiang, C.; Tseng, Z.; Nazeeruddin, M. K.; Hagfeldt, A.; Grätzel, M. High-efficiency stable inverted perovskite solar cells without current hysteresis. *Energy & Environmental Science* 2015, *8*(9), 2725-2733. https://doi.org/10.1039/C5EE00645G

Würfel, P., & Würfel, U. *Physics of Solar Cells: From Basic Principles to Advanced Concepts*, 3rd ed., John Wiley & Sons, 2016. URL: https://books.google.lt/books/about/Physics_of_Solar_Cells.html?id=Wqu-DAAAQBAJ&redir_esc=y

Xu, J., Boyd, C. C., Yu, Z. J., Palmstrom, A. F., Witter, D. J., Larson, B. W., France, R. M., Werner, J., Harvey, S. P., Wolf, E. J., Weigand, W., Manzoor, S., van Hest, M. F. A. M., Berry, J. J., Luther, J. M., Holman, Z. C., & McGehee, M. D. Triple-halide wide–band gap perovskites with suppressed phase segregation for efficient tandems. *Science*, 367(6482), 2020, 1097–1104. https://doi.org/10.1126/science.aaz5074

Zhang, Y.; Jia, X.; Liu, S.; Zhang, B.; Lin, K.; Zhang, J.; Conibeer, G. A review on thermalization mechanisms and prospect absorber materials for the hot carrier solar cells. *Solar Energy Materials and Solar Cells*, 225, 2021, 111073. https://doi.org/10.1016/j.solmat.2021.111073

Zhang, J.; Gao, J.; Church, C.P.; Miller, E.M.; Luther, J.M.; Klimov, V.I.; Beard, M.C. PbSe quantum dot solar cells with more than 6% efficiency fabricated in ambient atmosphere. *Nano Lett*. 2014, 14, 6010–6015. https://doi.org/10.1021/nl503085v

Zhao, J.; Wang, A.; Robinson, S. J.; Green, M. A. Reduced temperature coefficients for recent high-performance silicon solar cells. *Prog. Photovolt. Res. Appl.* 1994, 2(3), 221–225. https://doi.org/10.1002/pip.4670020305

Zhou, J.; You, Z.; Xu, W.; Su, Z.; Qiu, Y.; Gao, L.; Yin, C.; Lan, L. Microwave irradiation directly excites semiconductor catalyst to produce electric current or electron-hole pairs. *Scientific Reports*, **9**(1), 2019, 5470. https://doi.org/10.1038/s41598-019-41002-w

AUTHOR'S BIOGRAPHY

Name:	Ihor
Surname:	Zharchenko
Email:	ihor.zharchenko@ftmc.lt

Education:

2021 – 2025	State Research Institute Center for Physical Sciences and Technology. *PhD studies.*
2016 – 2017	National Technical University of Ukraine "Igor Sikorsky Kyiv Polytechnic Institute", Kyiv, Ukraine. *Specialist Academic Level in Micro- and Nanoelectronics Technology.*
2012 – 2016	National Technical University of Ukraine "Igor Sikorsky Kyiv Polytechnic Institute", Kyiv, Ukraine. *Bachelor's degree in Micro- and Nanoelectronics.*

Professional experience:

2024 – Present	State Research Institute Center for Physical Sciences and Technology, Laboratory of Electronic Processes. *Young researcher.*
2023 – Present	Vilnius Gediminas Technical University, Department of Electrical Engineering. *Lecturer.*
2022 – 2024	State Research Institute Center for Physical Sciences and Technology, Laboratory of Electronic Processes. *Engineer/Senior Engineer.*
2017 – 2021	Ukrspetstechnika, Kyiv, Ukraine. *Electronics Engineer.*

Vilniaus universiteto leidykla
Saulėtekio al. 9, III rūmai, LT-10222 Vilnius
El. p. info@leidykla.vu.lt, www.leidykla.vu.lt
bookshop.vu.lt, journals.vu.lt
Tiražas 25 egz.